

Purification and Distillation of Continuous Variable Entanglement

Von der Fakultät für Mathematik und Physik
der Gottfried Wilhelm Leibniz Universität Hannover
zur Erlangung des Grades eines

Doktors der Naturwissenschaften
– Dr. rer. nat. –

genehmigte Dissertation
von

Dipl.-Phys. Boris Hage

geboren am 19. Juni 1979 in Wolfsburg

2010

Referent:	Prof. Dr. Roman Schnabel
Korreferent:	Prof. Dr. Karsten Danzmann
Tag der Promotion:	25.01.2010

Abstract

Quantum communication and quantum computing to a large extent are based on the distribution and the processing of quantum entanglement. The implementation of the two is demanding because entanglement inherently is highly susceptible to decoherence, i.e. the uncontrollable loss of information to the environment. If the existing methods fail to minimize the decoherence sufficiently, entanglement *distillation* can solve this problem. Such a procedure extracts a smaller number of more strongly entangled states from a larger supply of weaker entangled states. In order to eliminate the decoherence completely or to realize quantum communication over a long distance this procedure has to be applied *iteratively*, i.e. the distillation is applied repeatedly on entangled states, which already have been distilled previously.

Within the scope of this thesis the experimental implementation of a continuous variable entanglement distillation protocol was conducted. The underlying entanglement was prepared in the quadrature amplitudes of monochromatic continuous-wave laser fields. The special decoherence process of phase diffusion was considered, which resulted in non-Gaussian probability distributions of the corresponding variables. The non-classicality of squeezed states suffering from this decoherence process was investigated using the characteristic function. The simultaneous distillation, purification and Gaussification of phase-diffused squeezed states was demonstrated. For the first time distilled entangled states were actually prepared for a downstream application. Furthermore, for the first time the iterative (multi-step) preparation of distilled entanglement was realized. Complete evidence was provided by the first implementation of a full, unbiased two-mode quantum state tomography in the continuous-variable regime.

Keywords: Quantum communication, entangled states, entanglement distillation.

Zusammenfassung

Die Konzepte der Quantenkommunikation und der Quantencomputer beruhen weitestgehend auf der Verteilung und Verarbeitung von Quantenverschränkung. Eine Umsetzung gestaltet sich als schwierig, denn Verschränkung weist eine starke Anfälligkeit für Dekohärenz, einen unkontrollierten Informationsverlust an die Umgebung, auf. Wenn die vorhandenen Methoden zur Minimierung der Dekohärenz unzureichend sind, kann die *Destillation* von Verschränkung dieses Problem lösen. Im Destillationsverfahren wird eine kleinere Anzahl stark verschränkter aus einer größeren Menge schwach verschränkter Zustände extrahiert. Um eine vollständige Eliminierung der Dekohärenz zu erreichen oder Quantenkommunikation auf große Distanz zu realisieren, muss die Destillation auf *iterative* Weise vorgenommen werden; dies bedeutet, dass das Destillationsverfahren wiederholt auch auf das Resultat einer vorherigen Destillation angewendet wird.

Im Rahmen der vorliegenden Arbeit wurde ein Verschränkungsdestillationsprotokoll in kontinuierlichen Variablen experimentell umgesetzt. Die zugrundeliegende Verschränkung bestand in den Quadraturamplituden von monochromatischen Dauerstrich-Laserstrahlen. Der spezielle Dekohärenzprozess der Phasendiffusion, der nicht-Gaußförmige Wahrscheinlichkeitsverteilungen zur Folge hat, wurde betrachtet. Die nicht-Klassizität von phasendiffundierten gequetschten Zuständen wurde untersucht. Die gleichzeitige Destillation, Purifikation und Gaussifikation von phasendiffundierten gequetschten Zuständen konnte gezeigt werden. Zum ersten Mal wurden destillierte verschränkte Zustände tatsächlich präpariert, was eine nachfolgende weitere Verwendung ermöglichte. Darüber hinaus wurde erstmalig eine *iterative* Destillation von Verschränkung realisiert. Auch hier wurde der präparierte Ausgangszustand für eine weitere Verwendung zur Verfügung gestellt. Der Nachweis wurde auf Grundlage einer vollständigen, unvoreingenommenen zwei-Moden Quantenzustandstomographie erbracht. Dies stellte die erste Implementierung dieser Methode im Bereich der kontinuierlichen Variablen dar.

Schlüsselwörter: Quanteninformation, verschränkte Zustände, Verschränkungsdestillation.

Acknowledgements

First of all I would like to thank my advisor, Prof. Dr. Roman Schnabel, for being an excellent mentor. He and the head of our department, Prof. Dr. Karsten Danzmann, provided a vivid, fruitful and efficient scientific environment. It was an honor for me to be a part of our institute.

I was delighted to interact with Dr. Jaromír Fiurášek, Associate Professor at the Palacký University Olomouc, Czech Republic. JF provided the theoretical background for the main part of this thesis. His enthusiasm was always stimulating and his ability to anticipate an experimentalist's point of view helped a lot during our productive discussions.

My gratitude goes to Prof. Dr. Werner Vogel from the University of Rostock, Germany, especially for our collaboration but also for the pleasant lunch breaks on several conferences.

I am indebted to many of my colleagues for their assistance in numerous ways. Especially my office mates Ali, Daniel, Henning and Stefan gave me a great time.

This thesis would at last not have been possible without the loving support of my family. Words cannot express my gratitude to Anke, whose love and confidence took the load off my shoulders. My parents, Bärbel and Herbert, also deserve my greatest gratitude for all their support during the long years of my education.

Contents

Contents	4
1 Introduction	7
2 Theory	11
2.1 Notation	11
2.1.1 Continuous Variables / Phase Space	12
2.1.2 Wigner Function	14
2.1.3 Glauber-Sudarshan P-function	15
2.2 Purification and Distillation	15
2.2.1 Purity of Quantum States	15
2.2.2 Phase-Diffused Squeezed States	16
2.2.3 Distillation of Phase-Diffused Squeezed States	18
2.2.4 Entanglement	20
2.2.5 Gaussian Entanglement – Two Mode Squeezing	21
2.2.6 Phase-Diffused Entangled States	24
2.2.7 Distillation of Phase-Diffused Entangled States	25
2.3 Quantum State Measurement	27
2.3.1 Homodyne Detection	27
2.3.2 Quantum State Tomography	31
3 Key Components of the Experiments	43
3.1 Laser Sources	43
3.1.1 Main Laser	43
3.1.2 Auxiliary Laser	46
3.2 Non-classical Light Sources / Squeezer	48
3.2.1 Optical and Mechanical Layout	51
3.2.2 Stabilization	55
3.3 Balanced Homodyne Detector	57
3.4 Quantum State Tomograph	59
3.5 Data Acquisition	61
3.6 Random Phase Diffusion	69
4 Experiments	75
4.1 Preparation and Characterization of Phase-Diffused Squeezed States	75

4.2	Distillation and Purification of Phase-Diffused Squeezed States	79
4.3	Distillation and Purification of Entangled States	87
4.4	Iterative Distillation and Purification of Entanglement	95
5	Discussion and Conclusion	103
A	Hardware	105
A.1	Homodyne Locking Scheme	105
A.1.1	Auxiliary Phase-Locked Laser	107
A.1.2	The Mixer Box	108
A.2	Electronics	110
A.2.1	Broadband Photo Detector	110
A.2.2	Resonant Photo Detector	111
A.2.3	Amplifier and Mixer for the Mixer Box	112
A.2.4	Subtractor / Adder for BHDs	113
A.2.5	Improved SHG Electronics	114
B	Calculus For Fun	115
B.1	Error Signals	115
B.1.1	Linear Set Point	115
B.1.2	Extremal Set Point	115
B.1.3	Extremal Not Modulatable Set Point, PDH Method	116
B.2	Modulation Of Light Fields	118
B.2.1	Amplitude Modulation	119
B.2.2	Phase Modulation	120
B.3	The Naive Optical Resonator	122
	Bibliography	127

Introduction

Since the quantum mechanical description of physical systems was formulated over a hundred years ago it has successfully explained many physical phenomena which were *mystical* to the classical theory. For example, the photoelectric effect was unexplainable without quantum mechanics. Also the spectrum of sunlight did not fit into the classical description of the interaction of light and matter. But quantum mechanics not only provided explanations for existing problems but also predicted new phenomena. Maybe the most tremendous aspect is the existence of *entangled states* of two or more physical systems. In contrast to classical physics the individual system in such a state – even when space-like separated – cannot be fully described individually by local quantities. This led Albert Einstein, Boris Podolsky and Nathan Rosen (EPR) in 1935 to the conclusion, that the theory of quantum mechanics must be incomplete, i.e. missing some hidden variables [1]. However, it turned out that – rather than quantum mechanics – EPR were wrong about their assumption of local reality. In 1965 John Steward Bell formulated the famous *Bell inequality* [2], based on the assumption of hidden variables. In 1982 Alain Aspect and his coworkers conducted the first experiment [3] with many more to follow, which violated the Bell inequality. In this sense quantum mechanics indeed is a valid and complete theory.

Measurements on the subsystems of an entangled state can exhibit a strong correlation exceeding any classical approach. Quantum mechanics also states that in general it is impossible to measure the quantum properties of a system without changing them. The vivid research field of quantum information makes use of these special properties to improve the quality of communication and information processing tasks. In general, a quantum field can be described by the number-operator or alternatively by two non-commuting position and momentum-like operators. It depends on the quantum picture of the measurement apparatus, which of the two is appropriate for the description of the experiment. The corresponding measurement results have either discrete or continuous spectra and form the basis of discrete-variable or continuous-variable quantum information, respectively. Within the frame of this thesis we work in the continuous variable regime. Here, entangled states of light can be generated in a reliable

and deterministic way by optical parametric amplifiers (OPAs). The states can be precisely manipulated with linear optics. The final measurements can be based on highly efficient balanced homodyne detectors. These entangled two-mode squeezed states show Gaussian probability distributions and were used for quantum teleportation [4] and entanglement swapping [5], [6]. In analogy to two-mode squeezed states of the light field, entangled states of the collective spins of two atomic ensembles have been generated [7]. Linking light and matter, the storage of quantum states of light in an atomic memory has been demonstrated [8]. The teleportation from a light-based state onto an atomic ensemble has been reported [9]. High-speed quantum cryptography with coherent light beams and homodyne detection has been demonstrated [10]. All these spectacular achievements reveal the great potential of this approach to quantum information processing.

The distribution of entangled states of light over long distances is a major challenge in the field of quantum information. However, due to the fragile nature of entangled states, environmental interactions such as optical losses, phase diffusion and mixing with thermal states lead to decoherence and destroy the non-classical properties after some finite transmission-line length. Obviously the first strategy to keep these effects small is to prevent the environmental interaction by using for example optical fibres with a small absorption coefficient. Yet, this strategy is not sufficient in many cases. For arbitrary distances, analogous to classical communication, *repeaters* can be inserted into the transmission line. *Quantum repeater* protocols [11], [12] were proposed to overcome this problem. These devices combine quantum memory [8], entanglement distillation [13], [14] and entanglement swapping [15]. The longer the distance the more repeater stages have to be used. A missing piece in this toolbox has been a feasible protocol for entanglement distillation and purification.

Entanglement distillation [13, 14] extracts from several shared copies of weakly entangled mixed states a single copy of a highly entangled state using only local quantum operations and classical communication (LOCC) between the two parties sharing the states. This procedure has to be applicable in an iterative way for a long distance scenario or in order to completely counteract the decoherence. In the continuous-variable regime this turned out to be a very challenging task. This regime is mainly based on linear optics, parametric amplification and homodyne detection. All these devices perform Gaussian operations. This characterizes the class of operations, which preserve the Gaussian properties of a state. It was proved that it is impossible to distil Gaussian entangled states by means of the experimentally accessible Gaussian operations [16, 17]. Though, a whole class of important decoherence processes give rise to non-Gaussian noise and therefore produce non-Gaussian entangled states. It has been shown [18] that in this case the entanglement distillation can be carried out using only interference on beam splitters, balanced homodyne detection and conditioning on the measurement outcomes. Precursor experiments confirmed this by successful demonstrations of distillation and purification protocols for single squeezed modes that suffered from de-Gaussifying noise [19, 20, 21, 22].

Within this thesis the results of the first experimental implementation of an iterative

entanglement distillation scheme are presented. A brief description of the underlying theory is provided in Chapter 2. This includes a short presentation of the theoretical model of the distillation scheme, which is based on the work of J. Fiurášek et al. [18]. In Chapter 3 a detailed description of the individual components of the experiments can be found. The main experiments and the results are presented in Chapter 4. The experimental setups are described in terms of the components from the previous chapter. The focus is set on the linking elements and the presentation of the results. A discussion of the results can be found in Chapter 5.

Theory

This section gives a brief description of the theoretical environment which the results of this work live in. It is short and as such it is not meant to be complete. It is rather a compilation of fundamental considerations plus details about purification and distillation. For a detailed description, see either of the books [23, 24, 25] and the individual references. We use the standard *bra-ket* notation $|n\rangle$ and denote operators with a hat, e.g. \hat{a} . The Planck constant \hbar is set to unity unless noted differently.

2.1 Notation

We postulate that the electric field strength \hat{E} for a single spatial mode for a single frequency, see Page 28, characterized by $u(\vec{x}, t)$ is given by:

$$\hat{E} = u^*(\vec{x}, t)\hat{a} + u(\vec{x}, t)\hat{a}^\dagger, \quad (2.1)$$

with the bosonic annihilation operator \hat{a} for the amplitude, which are subject to the commutation relation:

$$[\hat{a}, \hat{a}^\dagger] = 1. \quad (2.2)$$

The number of photons in the considered mode is counted by:

$$\hat{n} = \hat{a}^\dagger \hat{a}, \quad (2.3)$$

which we use for the phase shift operator $\hat{U}(\theta) = e^{-i\theta\hat{n}}$, that shifts the phase of \hat{a} by the amount θ :

$$\hat{U}(\theta)^\dagger \hat{a} \hat{U}(\theta) = \hat{a} e^{-i\theta}. \quad (2.4)$$

2.1.1 Continuous Variables / Phase Space

Based on the amplitude operator we define the Hermitean operators \hat{q} for the amplitude quadrature and \hat{p} for the phase quadrature:

$$\hat{q} = \sigma(\hat{a}^\dagger + \hat{a}), \quad \hat{p} = i\sigma(\hat{a}^\dagger - \hat{a}). \quad (2.5)$$

Commonly, the scaling factor σ is set to $\sigma = \sqrt{1/2}$, which leads from Equation 2.2 to the commutation relation of conjugate observables:

$$[\hat{q}, \hat{p}] = i. \quad (2.6)$$

Sometimes it is preferable to set the scaling factor differently. The uncertainty limit for \hat{q} and \hat{p} reads:

$$\Delta\hat{q}\Delta\hat{p} \geq \sigma^2. \quad (2.7)$$

In case of the vacuum state the limit is met and the individual uncertainties are equal. For the variance $V_{q,vac}$ of the \hat{q} quadrature we obtain:

$$V_{q,vac}(\Delta\hat{q})^2 = \sigma^2. \quad (2.8)$$

This quantity can be measured experimentally and is often used to normalize the whole apparatus the quantum scale. In this situation it is sometimes more convenient to consider $\sigma = 1$ as a reference. For a squeezing experiment this scaling is often circumvented by quantifying the squeezed variance V_{sqz} on a Decibel scale: $10 \log_{10}(V_{sqz}/V_{vac})$, which is unique, independent of the scaling σ .

Quadrature Eigenstates

The eigenstates $|q\rangle$ and $|p\rangle$ of the quadrature operators are defined by:

$$\hat{q}|q\rangle = q|q\rangle, \quad \hat{p}|p\rangle = p|p\rangle. \quad (2.9)$$

Being orthogonal and complete they can be used as a basis for the state space, see Section 2.1.2 for the Wigner function. The probability density $prd(q)$ for e.g. the \hat{q} quadrature is given by the absolute square of the quadrature wave function $\psi(q) = \langle q|\psi\rangle$:

$$prd(q) = |\psi(q)|^2. \quad (2.10)$$

In the experiment this is measured by homodyne detection, see Section 2.3.1.

Fock States

Fock states are the eigenstates of the photon number operator:

$$\hat{n} |n\rangle = n |n\rangle. \quad (2.11)$$

They are also complete and orthogonal and have discrete eigenvalues. This allows to represent a state $\hat{\rho}$ by the matrix:

$$\rho_{mn} = \langle m | \hat{\rho} | n \rangle. \quad (2.12)$$

In Section 2.3.2 we use their wave functions:

$$\psi_n(q) = \frac{H_n(q)}{\sqrt{2^n n!} \sqrt{\pi}} e^{-q^2/2}, \quad (2.13)$$

for the reconstruction of the density matrix ρ_{mn} from balanced homodyning measurements. Here, H_n denote the *Hermite polynomials*.

Glauber States

The light field created by a laser of high quality comes close to a Glauber state. These states are also called *coherent states*, and defined as eigenstates of the annihilation operator (analogous the classical amplitude):

$$\hat{a} |a\rangle = \alpha |a\rangle. \quad (2.14)$$

Coherent states are not orthogonal:

$$|\langle \alpha' | \alpha \rangle|^2 = e^{-|\alpha - \alpha'|^2}, \quad (2.15)$$

but complete and we can represent a state in the coherent state basis, see Section 2.1.3 for the *P*-function.

Squeezed States

In a formal way *squeezed states* $|s\rangle$ are generated by applying the squeezing operator \hat{S} :

$$\hat{S}(\zeta) = e^{\frac{1}{2}(\zeta^* \hat{a}^2 - \zeta \hat{a}^{\dagger 2})}, \quad (2.16)$$

on the vacuum state $|0\rangle$:

$$|s\rangle = \hat{S}(\zeta) |0\rangle. \quad (2.17)$$

Under squeezing with a real squeezing parameter ζ the quadrature operators transform like:

$$\begin{aligned}\hat{S}^\dagger(\zeta)\hat{q}\hat{S}(\zeta) &= \hat{q}e^{-\zeta}, \\ \hat{S}^\dagger(\zeta)\hat{p}\hat{S}(\zeta) &= \hat{p}e^{+\zeta}.\end{aligned}\tag{2.18}$$

One quadrature gets compressed including its quantum fluctuations and the other gets stretched, that is the reason why squeezing is called *squeezing*. The vacuum state has equal variances for both quadratures. After a squeezing operation this is no longer the case and the variances for the squeezed vacuum read:

$$\begin{aligned}V_s &= (\Delta q)^2 = \frac{1}{2}e^{-2\zeta}, \\ V_a &= (\Delta p)^2 = \frac{1}{2}e^{+2\zeta},\end{aligned}\tag{2.19}$$

with $\sigma = \sqrt{1/2}$ in the quadrature definition, Equation 2.5. For a complex ζ the phase determines the orientation of the squeezing effect in quadrature phase space.

2.1.2 Wigner Function

The Wigner function $W(p, q)$ [26] is an unique representation of a quantum state described by the density operator $\hat{\rho}$:

$$W(q, p) = \frac{1}{2\pi} \int_{-\infty}^{\infty} \left\langle q - \frac{x}{2} \left| \hat{\rho} \right| 1 + \frac{x}{2} \right\rangle dx.\tag{2.20}$$

The probability density $pr_{d_\phi}(q_\phi)$ for a rotated quadrature $q_\phi = q \cos \phi + p \sin \phi$ is obtained by a projection of the Wigner function for the corresponding direction:

$$pr_{d_\phi}(q) = \int_{-\infty}^{\infty} W(q \cos \phi - p \sin \phi, q \sin \phi + p \cos \phi) dp.\tag{2.21}$$

A remarkable property is the overlap formula, which provides the possibility to calculate the expectation value for an operator \hat{F} :

$$\text{tr}(\hat{\rho}\hat{F}) = 2\pi \int_{-\infty}^{\infty} \int_{-\infty}^{\infty} W(q, p)W_{\hat{F}}(q, p) dq dp,\tag{2.22}$$

with $W_{\hat{F}}(q, p)$ for the Wigner function obtained by replacing $\hat{\rho}$ with \hat{F} in Equation 2.20.

2.1.3 Glauber-Sudarshan P-function

In the same year of 1963, Glauber [27] and Sudarshan [28] *invented* the P-function by assuming a state $\hat{\rho}$ to be composed of coherent states $|\alpha\rangle$:

$$\hat{\rho} = \int_{-\infty}^{\infty} \int_{-\infty}^{\infty} P(q, p) |\alpha\rangle \langle \alpha| dq dp, \quad (2.23)$$

with $\alpha = 1/\sqrt{2}(q + ip)$. In general, the P-function cannot be well-behaved like a probability distribution. If this were the case, all quantum states except for the coherent states themselves would be classical mixtures of coherent states. This implies that all pure states, too, would appear as a statistical mixture of coherent states. Already for coherent states, which in a sense mark the border between the classical and the quantum world, the P-function is a singular δ -distribution. Any P-function, which is more singular than a δ -distribution or negative, is considered to represent a non-classical state. In general, it does not even exist for all quantum states.

The P-function and the Wigner function are connected via a convolution with a Gaussian function corresponding to the vacuum:

$$W(q, p) = \frac{1}{\pi} \int_{-\infty}^{\infty} \int_{-\infty}^{\infty} P(q', p') e^{-(q-q')^2 - (p-p')^2} dq' dp'. \quad (2.24)$$

The convolution turns into a simple product for the respective characteristic functions, i.e. the Fourier transforms:

$$\tilde{W}(u, v) = \tilde{P}(u, v) e^{-\frac{1}{4}(u^2 + v^2)}, \quad (2.25)$$

in polar coordinates:

$$\tilde{W}(\xi, \phi) = \tilde{P}(\xi, \phi) e^{-\frac{1}{4}(\xi^2)}. \quad (2.26)$$

As we know from Section 2.1.2, $\tilde{W}(\xi, \phi)$ equals the characteristic functions of the probability densities $\tilde{p}rd_\phi(\xi)$ for the quadrature angle ϕ . Thus, $\tilde{W}(\xi, \phi)$ must be always well-behaved and the same must be valid for $\tilde{P}(\xi, \phi)$.

2.2 Purification and Distillation

2.2.1 Purity of Quantum States

In order to discriminate, whether a state described by the density operator $\hat{\rho}$ is pure or mixed, fundamentally the *von Neumann* entropy S can be used [29]:

$$S = -\text{tr}(\hat{\rho} \ln \hat{\rho}), \quad (2.27)$$

which gives $S = 0$ only for a pure state and $S > 0$ for any mixed state. The *purity* μ with:

$$\mu = \text{tr}\hat{\rho}^2, \quad (2.28)$$

represents a more easily computable quantity with $\mu = 1$ for pure states and $\mu < 1$ for mixed states. This can be seen from the diagonal representation of $\hat{\rho}$. The elements represent probabilities. Hence, they are positive and not larger than 1:

$$\text{tr}\hat{\rho}^2 = \sum_k \rho_k^2 \leq \sum_k \rho_k = 1. \quad (2.29)$$

Within the valid range of ρ_k we find $1 - \rho_k \leq -\ln \rho_k$. This gives a lower bound for the *von Neumann* entropy:

$$S \geq 1 - \mu. \quad (2.30)$$

For Gaussian states, which are represented by the covariance matrix γ , the purity is given by:

$$\mu = \frac{1}{\sqrt{\det \gamma}}, \quad (2.31)$$

with *det* denoting the determinant. This property follows from the Wigner overlap formula, see Equation 2.98.

2.2.2 Phase-Diffused Squeezed States

In general, a squeezed state can have an arbitrary orientation in phase space, denoted by the rotation angle ϕ starting from an amplitude squeezed state. The Wigner function of such a state with the rotated quadratures $q_\phi = q \cos \phi + p \sin \phi$ and $p_\phi = -q \sin \phi + p \cos \phi$ reads:

$$W_r[q, p, \phi] = \frac{1}{2\pi\sqrt{V_s V_a}} e^{-\frac{q_\phi^2}{2V_s} - \frac{p_\phi^2}{2V_a}}. \quad (2.32)$$

The variances of the squeezed and anti-squeezed quadratures are denoted V_s and V_a . The probability distribution $prd_q(q, \phi)$ of the amplitude quadrature can be obtained via integration over p :

$$prd_q(q, \phi) = \int_{-\infty}^{\infty} W_r[q, p, \phi] dp \quad (2.33)$$

$$= \frac{1}{\sqrt{2\pi V_q(\phi)}} e^{-\frac{q^2}{2V_q(\phi)}}, \quad (2.34)$$

with the variance of the amplitude quadrature $V_q(\phi)$:

$$V_q(\phi) = V_s \cos^2 \phi + V_a \sin^2 \phi \quad (2.35)$$

$$= \frac{1}{2} [V_s + V_a + (V_s - V_a) \cos 2\phi]. \quad (2.36)$$

A phase-diffused squeezed state is a statistical mixture of squeezed states with a rotation corresponding to the phase diffusion. The Wigner function $W_d(q, p)$ of the diffused state with the probability density of the diffusion phase denoted $\Phi(\phi)$ reads:

$$W_d[q, p] = \int_{-\infty}^{\infty} \Phi(\phi) W_r[q, p, \phi] d\phi. \quad (2.37)$$

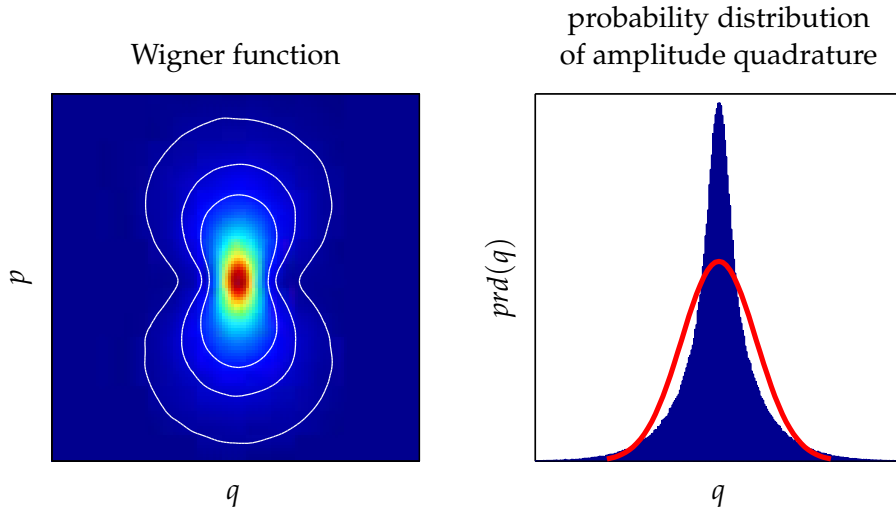


Figure 2.1 - Left: Wigner function of a phase-diffused squeezed state with an initial squeezed variance of -10 dB and $\sigma_\phi = 0.6$. Note the shape of the contour lines is not at all an ellipse as for a squeezed state. Right: probability distribution of the amplitude quadrature (blue) compared to a Gaussian fit (red). The state is obviously non-Gaussian.

For the variance $V_{q,d}$ of the amplitude quadrature of such a state we obtain:

$$V_{q,d} = \int_{-\infty}^{\infty} \Phi(\phi) V_q(\phi) d\phi. \quad (2.38)$$

For the experiments presented in Chapter 3 the phase diffusion was Gaussian with zero mean, characterized by the standard deviation σ_ϕ . In this case we can solve Equation

2.38 and obtain for the variance $V_{q,g}$ of the amplitude quadrature:

$$V_{q,g}(\sigma_\phi) = \frac{1}{2} \left[V_s + V_a + (V_s - V_a) e^{-2\sigma_\phi^2} \right]. \quad (2.39)$$

Note that the variances are insufficient to describe a phase-diffused squeezed state. See Figure 2.1 for the Wigner function and the probability distribution of the amplitude quadrature, which would be squeezed without phase diffusion.

2.2.3 Distillation of Phase-Diffused Squeezed States

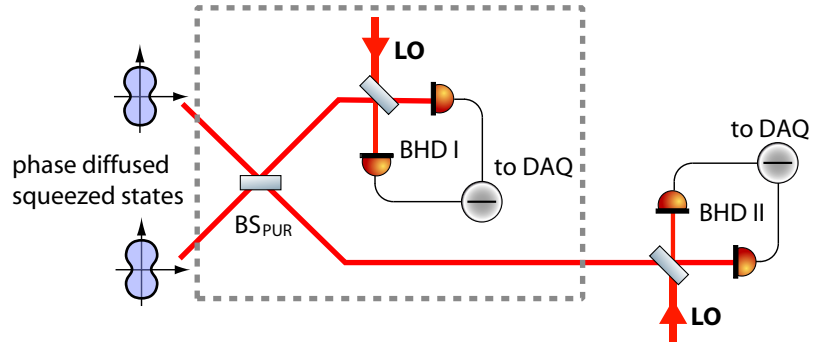


Figure 2.2 - Scenario for the purification/distillation of phase-diffused squeezed states. Two copies of a phase-diffused squeezed state are superimposed on a balanced (50/50) beam-splitter (BS_{PUR}). Two balanced homodyne detectors (BHD I and BHD II) in combination with a digital data acquisition system synchronously recorded time series of measured quadrature values. Note that the elementary components for the protocol can be considered as a box with two inputs for phase-diffused squeezed states and an output for the distilled/purified state.

The following section will describe our distillation / purification protocol for phase-diffused squeezed states and derive the basic properties. For a more general description see [18, 30]. The frame for this protocol is depicted in Figure 2.2. The protocol prepares a new state from two phase-diffused states, with more squeezing and a higher purity. The properties of a phase-diffused squeezed state, which this protocol relies on, can be found in the previous section.

The quadratures measured with the balanced homodyne detectors (BHD) are termed $q_{1\theta} = q_1 \cos \theta + p_1 \sin \theta$ for the first balanced homodyne detector, BHD I, and $q_{2\phi} = q_2 \cos \phi + p_2 \sin \phi$ for BHD II. The protocol is based on marking the output state valid or invalid depending on the measurement result of BHD I. A positive purification/distillation trigger signal will be provided, if $|q_{1\theta}| < Q$ with a certain threshold value of Q . We assume that before phase diffusion the q quadratures of each input beam is squeezed and that there are no correlations between q and p quadratures. The covariance matrix of each squeezed mode thus attains a diagonal form, $\gamma = \text{diag}(V_s, V_a)$, where V_s and V_a denote variances of q and p quadratures, which are assumed to be of equal value for both states. For the vacuum state we have $V_q = V_p = 1$ and the mode will be squeezed, if $V_q < 1$. Recall that $V_q V_p \geq 1$ as a consequence of the Heisenberg uncertainty relation.

Let us assume for a moment that the random phase shifts ϕ_j on each mode are fixed. Let $V_{qj} = V_s \cos^2 \phi_j + V_a \sin^2 \phi_j$ and $V_{pj} = V_a \cos^2 \phi_j + V_s \sin^2 \phi_j$, $j = 1, 2$ denote the variances of the phase shifted squeezed states impinging on BS_{PUR} . For a fixed ϕ_j , the two-mode state at the output of BS_{PUR} and prior to conditioning measurement is Gaussian. Consequently, the joint probability distribution of quadratures $q_{1\theta}$ of mode 1 and q_2 of mode 2 at the output of BS_{PUR} is also Gaussian and reads:

$$P_{12}(q_{1\theta}, q_2) = \frac{1}{2\pi\sqrt{D}} \exp \left[-\frac{Bq_{1\theta}^2 + Aq_2^2 - 2Cq_{1\theta}q_2}{2D} \right]. \quad (2.40)$$

Here, $D = AB - C^2$, A and B are variances of quadratures $q_{1\theta}$ and q_2 evaluated for the state at the output of BS_{PUR} ,

$$\begin{aligned} A &= \frac{V_{q1} + V_{q2}}{2} \cos^2 \theta + \frac{V_{p1} + V_{p2}}{2} \sin^2 \theta \\ &\quad + \frac{V_a - V_s}{4} [\sin(2\phi_1) + \sin(2\phi_2)] \sin(2\theta), \\ B &= \frac{V_{q1} + V_{q2}}{2}. \end{aligned} \quad (2.41)$$

The correlation between the quadratures $C = \langle \Delta q_{1\theta} \Delta q_2 \rangle$ reads:

$$C = \frac{V_{q1} + V_{q2}}{2} \cos \theta + \frac{V_a - V_s}{4} [\sin(2\phi_1) - \sin(2\phi_2)] \sin \theta. \quad (2.42)$$

The non-normalized distribution of q_2 conditional on $|q_{1\theta}| < Q$ reads:

$$P_{\text{cond}}(q_2) = \int_{-Q}^Q P_{12}(q_{1\theta}, q_2) dq_{1\theta}. \quad (2.43)$$

If the phase fluctuations are symmetric, $\Phi(-\phi) = \Phi(\phi)$ then the mean value of the quadrature q_2 of the purified state will be zero. This is assumed to be the case throughout this thesis. Under these conditions the variance V_{out} of the quadrature q_2 becomes equal to $\langle q_2^2 \rangle$ calculated from the conditional probability distribution (Equation 2.43), averaged over all random phase shifts and properly normalized,

$$V_{\text{out}} = \frac{1}{\mathcal{P}} \int_{\phi_1} \int_{\phi_2} \int_{-\infty}^{\infty} q_2^2 P_{\text{cond}}(q_2) dq_2 \Phi(\phi_1) \Phi(\phi_2) d\phi_1 d\phi_2, \quad (2.44)$$

where:

$$\mathcal{P} = \int_{\phi_1} \int_{\phi_2} \int_{-\infty}^{\infty} P_{\text{cond}}(q_2) dq_2 \Phi(\phi_1) \Phi(\phi_2) d\phi_1 d\phi_2, \quad (2.45)$$

is the probability of successful purification/distillation. The integration over q_2 can be

explicitly carried out and after some algebra we arrive at:

$$V_{\text{out}} = \frac{1}{\mathcal{P}} \iint \left[B \operatorname{erf} \left(\frac{Q}{\sqrt{2A}} \right) - \sqrt{\frac{2}{\pi}} \frac{C^2 Q}{A^{3/2}} e^{-\frac{Q^2}{2A}} \right] \Phi(\phi_1) \Phi(\phi_2) d\phi_1 d\phi_2. \quad (2.46)$$

We also obtain a simplified formula for the success probability:

$$\mathcal{P} = \int_{\phi_1} \int_{\phi_2} \operatorname{erf} \left(\frac{Q}{\sqrt{2A}} \right) \Phi(\phi_1) \Phi(\phi_2) d\phi_1 d\phi_2. \quad (2.47)$$

For comparison we refer to the variance of the q quadrature of the phase-diffused state before purification/distillation:

$$V_{\text{in}} = \int_{\phi} (V_q \cos^2 \phi + V_p \sin^2 \phi) \Phi(\phi) d\phi. \quad (2.48)$$

Successful purification/distillation increases the squeezing, which is indicated by $V_{\text{out}} < V_{\text{in}}$. Note that $V_{\text{out}} \geq V_x$ would always hold as the purification/distillation cannot reduce V_{out} below the variance V_x of the original state before transmission through a noisy channel. However, the method can restore the squeezing lost due to the phase fluctuations (or other non-Gaussian noise). After purification/distillation, the state also becomes Gaussified and its purity increases [18, 21, 22], which clearly demonstrates that our method meets all requirements imposed on a proper purification/distillation protocol.

This protocol can be extended for more than two input copies, see [30].

2.2.4 Entanglement

In general, a pure bipartite state $|\psi\rangle$ with the subsystems labeled a, b is a linear combination of tensor products of states of the subsystems:

$$|\psi\rangle = \sum_{kl} c_{kl} |a_k\rangle_a |b_l\rangle_b. \quad (2.49)$$

According to [31] a basis exists for each subsystem $\{|u_k\rangle_a\}$ and $\{|v_k\rangle_b\}$, for which the so-called *Schmidt decomposition* reads:

$$|\psi\rangle = \sum_k c_k |u_k\rangle_a |v_k\rangle_b. \quad (2.50)$$

The state will be entangled, if and only if more than one nonzero coefficients, the *Schmidt rank*, is needed for this decomposition. For a general mixed state $\hat{\rho}_{ab}$ it was shown [32] that the quantum state of the bipartite system will be separable, i.e. not

entangled, if it is a mixture of product states of the subsystems:

$$\hat{\rho}_{ab} = \sum_k c_k \hat{\rho}_{k,a} \otimes \hat{\rho}_{k,b}. \quad (2.51)$$

This property, in general, is hard to judge, but a convenient criterion for the separability based on the transposition of one of the subsystems was found in [33]. For separable states the partial transposition:

$$\hat{\rho}_{ab}^{T_a} = \sum_k c_k \hat{\rho}_{k,a}^T \otimes \hat{\rho}_{k,b}, \quad (2.52)$$

yields again a density operator, i.e. an operator with unit trace and nonnegative elements in the diagonal form, because $\hat{\rho}_{k,a}^T = \hat{\rho}_{k,a}^*$ is a valid density operator. This condition is necessary for separable states. Thus, the existence of a single negative eigenvalue of $\hat{\rho}_{ab}^{T_a}$ is a sufficient condition for entanglement. This is called the *npt-criterion* (negative partial transpose).

Based on the partial transposition a quantity called the *logarithmic negativity* $E_{\mathcal{N}}$ can be defined [34]:

$$E_{\mathcal{N}} = \log_2 \|\hat{\rho}_{ab}^{T_a}\|_1 = \log_2 \text{tr} \sqrt{\hat{\rho}_{ab}^{T_a*} \hat{\rho}_{ab}^{T_a}}, \quad (2.53)$$

with $\|\cdot\|_1$ denoting the trace norm. The logarithmic negativity can be regarded as a measure for the *npt*-ness of the state and thus for the strength of the entanglement.

2.2.5 Gaussian Entanglement – Two Mode Squeezing

Here we describe the kind of entanglement, which we prepared in the experiment. For a detailed description, see e.g. [35]. We take two squeezed modes as described in Equation 2.18 with the squeezing parameters ζ_1 and ζ_2 :

$$\hat{q}_i = e^{-\zeta_i} \hat{q}_i^{(0)}, \quad \hat{p}_i = e^{+\zeta_i} \hat{p}_i^{(0)}, \quad (2.54)$$

with the superscript (0) indicating the vacuum state. These states are superimposed on a 50:50 beam splitter, for which the two output amplitudes $\hat{b}_{1,2}$ are related to the two inputs $\hat{a}_{1,2}$ by:

$$\begin{aligned} \hat{b}_1 &= \frac{1}{\sqrt{2}}(\hat{a}_1 + \hat{a}_2), \\ \hat{b}_2 &= \frac{1}{\sqrt{2}}(\hat{a}_1 - \hat{a}_2), \end{aligned} \quad (2.55)$$

with $\hat{a}_{1,2}$ chosen to be in phase for the interference. The input-output relations for the

quadratures are identical. With \hat{q}_{bi} and \hat{p}_{bi} for the quadratures of \hat{b}_i we obtain:

$$\begin{aligned}\hat{q}_{b1} &= \frac{1}{\sqrt{2}}(\hat{q}_1 + \hat{q}_2) = \frac{1}{\sqrt{2}}(e^{-\zeta_1}\hat{q}_1^{(0)} + e^{-\zeta_2}\hat{q}_2^{(0)}), \\ \hat{p}_{b1} &= \frac{1}{\sqrt{2}}(\hat{p}_1 + \hat{p}_2) = \frac{1}{\sqrt{2}}(e^{+\zeta_1}\hat{p}_1^{(0)} + e^{+\zeta_2}\hat{p}_2^{(0)}), \\ \hat{q}_{b2} &= \frac{1}{\sqrt{2}}(\hat{q}_1 - \hat{q}_2) = \frac{1}{\sqrt{2}}(e^{-\zeta_1}\hat{q}_1^{(0)} - e^{-\zeta_2}\hat{q}_2^{(0)}), \\ \hat{p}_{b2} &= \frac{1}{\sqrt{2}}(\hat{p}_1 - \hat{p}_2) = \frac{1}{\sqrt{2}}(e^{+\zeta_1}\hat{p}_1^{(0)} - e^{+\zeta_2}\hat{p}_2^{(0)}).\end{aligned}\quad (2.56)$$

If we choose an equal amount of squeezing and equal orientation of the squeezing ellipses: $\zeta = \zeta_1 = \zeta_2$, we will find:

$$\begin{aligned}\hat{q}_{b1} &= e^{-\zeta_2}\hat{q}_{b1}^{(0)}, \\ \hat{p}_{b1} &= e^{+\zeta_2}\hat{p}_{b1}^{(0)},\end{aligned}\quad (2.57)$$

and the same for the other output with $q_{b1}^{(0)}$ denoting the vacuum output mode derived from Equation 2.55. In this case there is obviously no entanglement, as the two output modes can be expressed independently.

In contrast, if we choose a perpendicular orientation: $\zeta = -\zeta_1 = \zeta_2$, we will find:

$$\begin{aligned}\hat{q}_{b1} &= \cosh \zeta q_{b1}^{(0)} + \sinh \zeta q_{b2}^{(0)}, \\ \hat{q}_{b2} &= \cosh \zeta q_{b2}^{(0)} + \sinh \zeta q_{b1}^{(0)},\end{aligned}\quad (2.58)$$

and the same for the p quadratures. Here we cannot see the separation of the former case. We can see the entanglement by looking at the covariance matrix γ of the four output quantities $\hat{q}_{b1}, \hat{q}_{b2}, \hat{p}_{b1}, \hat{p}_{b2}$. For Gaussian states as considered here, this is a unique description of the state. For this purpose we go back to Equation 2.56, because there we have independent mode operators $\hat{q}_i^{(0)}, \hat{p}_i^{(0)}$ and find:

$$\gamma = \begin{pmatrix} \cosh 2\zeta & 0 & \sinh 2\zeta & 0 \\ 0 & \cosh 2\zeta & 0 & -\sinh 2\zeta \\ \sinh 2\zeta & 0 & \cosh 2\zeta & 0 \\ 0 & -\sinh 2\zeta & 0 & \cosh 2\zeta \end{pmatrix}, \quad (2.59)$$

which we normalized to the quadrature variance of the vacuum state. On the diagonal we see that the individual quadratures are very noisy. We also find a correlation of the two amplitude quadratures and an anti-correlation in the phase quadratures, leading

to the fact, that the difference of the q quadratures and the sum of the p quadratures each are very quiet:

$$\begin{aligned}\frac{\langle(\hat{q}_{b1} - \hat{q}_{b1})^2\rangle}{\langle(\hat{q}_1^{(0)})^2\rangle} &= 2e^{-2\zeta}, \\ \frac{\langle(\hat{p}_{b1} + \hat{p}_{b1})^2\rangle}{\langle(\hat{p}_1^{(0)})^2\rangle} &= 2e^{-2\zeta}.\end{aligned}\quad (2.60)$$

This is equivalent to the EPR Gedanken-experiment [1], which the so called EPR-criterion for the presence of entanglement in the EPR sense was derived from in [36, 37] and applied in e.g. [38]. In the idealized case considered here this boils down to the inequality:

$$\frac{\langle(\hat{q}_{b1} - \hat{q}_{b1})^2\rangle}{\langle(\hat{q}_1^{(0)})^2\rangle} \frac{\langle(\hat{p}_{b1} + \hat{p}_{b1})^2\rangle}{\langle(\hat{p}_1^{(0)})^2\rangle} \geq 1, \quad (2.61)$$

which will be violated, if the entanglement is strong enough to demonstrate the EPR-paradox, i.e. if by measuring q_{b1}, p_{b2} an inference of q_{b2}, p_{b1} is more accurate than the vacuum fluctuation will allow. Under these idealized conditions this is the case for a squeezing factor of -3 dB for the two input modes.

For our experiments we will take the simpler approach to generate so-called *v-class* entanglement [39] by using only one squeezed field and a vacuum field. For the corresponding calculation this means $\zeta_2 = 0$ and $\zeta_1 = \zeta$. The corresponding covariance matrix γ_v reads:

$$\gamma_v = \frac{1}{2} \begin{pmatrix} 1 + e^{-2\zeta} & 0 & 1 - e^{-2\zeta} & 0 \\ 0 & 1 + e^{+2\zeta} & 0 & 1 - e^{+2\zeta} \\ 1 - e^{-2\zeta} & 0 & 1 + e^{-2\zeta} & 0 \\ 0 & 1 - e^{+2\zeta} & 0 & 1 + e^{+2\zeta} \end{pmatrix}, \quad (2.62)$$

which again is normalized to the quadrature variance of the vacuum state. For the difference/sum of the q/p quadrature we find:

$$\begin{aligned}\frac{\langle(\hat{q}_{b1} - \hat{q}_{b1})^2\rangle}{\langle(\hat{q}_1^{(0)})^2\rangle} &= 2e^{-2\zeta}, \\ \frac{\langle(\hat{p}_{b1} + \hat{p}_{b1})^2\rangle}{\langle(\hat{p}_1^{(0)})^2\rangle} &= 1.\end{aligned}\quad (2.63)$$

In the perfectly lossless case more than -6 dB of input squeezing is required for the EPR-criterion. For the characterization of the experiment we chose a weaker criterion for separability, which is derived in [40] and solely based on the Heisenberg uncertainty

and the Cauchy-Schwarz inequality. This criterion does not assume Gaussian states:

$$I = \frac{\langle (a\hat{q}_{b1} - \frac{1}{a}\hat{q}_{b1})^2 \rangle + \langle (a\hat{p}_{b1} + \frac{1}{a}\hat{p}_{b1})^2 \rangle}{\langle (\hat{q}_1^{(0)})^2 \rangle} \geq 2 \left(a + \frac{1}{a} \right). \quad (2.64)$$

We term I the *total variance*, which necessarily fulfills the inequality for separable states, with a being an arbitrary nonnegative real number. See [38] for an experimental investigation of different entanglement criteria.

2.2.6 Phase-Diffused Entangled States

Relating to the experiments we restrict ourselves to the special case of Gaussian entangled states as considered in the previous section. In order to describe a phase-diffused entangled state, we use the four dimensional quadrature phase space with the labeling (q_1, p_1) for the quadratures of the first subsystem and (q_2, p_2) for the second. We follow the approach of Section 2.2.2 and use the two-mode Wigner function. Analogous to the single mode case in Section 2.1.2, a projection on a plane $[q_{1\theta_1}, q_{2\theta_2}]$ yields the joint probability distribution $P(q_{1\theta_1}, q_{2\theta_2})$ for the quadratures $\hat{q}_{i\theta_i} = \hat{q}_i \cos \theta_i + p_i \sin \theta_i$. For Gaussian states with the covariance matrix γ the Wigner function reads [35]:

$$W(\xi) = \frac{1}{4\pi^2 V_0^2} e^{-\frac{1}{2V_0} \xi \gamma^{-1} \xi}, \quad (2.65)$$

with $\xi = (q_1, p_1, q_2, p_2)$. Keep in mind that γ is normalized to the quadrature variance of the vacuum $V_0 = \langle (\hat{q}_1^{(0)})^2 \rangle$. For the Wigner function of the *s-class* entanglement from the previous section we obtain:

$$W(\xi) = \frac{1}{4\pi^2 V_0^2} e^{-[e^{-2\zeta}(q_1+q_2)^2 + e^{-2\zeta}(p_1-p_2)^2 + e^{+2\zeta}(q_1-q_2)^2 + e^{+2\zeta}(p_1+p_2)^2]/4V_0}. \quad (2.66)$$

Let us now analyze the phase diffusion of such state, by for a moment assuming a fixed phase shift θ_1 for the first subsystem and θ_2 for the second. This corresponds to a rotation of the quadratures: $\hat{q}_{i\theta_i} = \hat{q}_i \cos \theta_i + p_i \sin \theta_i$ and $\hat{q}_{i\theta_i} = \hat{p}_i \cos \theta_i - q_i \sin \theta_i$. The Wigner function of the phase shifted state is obtained from Equation 2.66 inserting the rotated quadratures: $W(q_{1\theta_1}, p_{1\theta_1}, q_{2\theta_2}, p_{2\theta_2})$. After some algebra we find the discrepancy of the phase shifted state to the initial one of Equation 2.66. There are two extra terms in the square brackets of the exponential, which read: $(p_1 p_2 - q_1 q_2) [\cos(\theta_1 + \theta_2) - 1] - (q_1 p_2 + p_1 q_2) \sin(\theta_1 + \theta_2) \sinh 2\zeta$.

We find that the discrepancy depends only of the sum of the individual phase shifts. In order to characterize the phase diffusion we can use the probability distribution $\Phi(\theta)$ of the sum of the individual phases $\theta = \theta_1 + \theta_2$. Like in Section 2.2.2 the phase-diffused state represented by W_d is a mixture of rotated states according to the probability dis-

tribution of the phase noise:

$$W_d(\xi) = \int_{-\infty}^{\infty} W(q_{1\theta_1}, p_{1\theta_1}, q_{2\theta_2}, p_{2\theta_2}) \Phi(\theta) d\theta. \quad (2.67)$$

2.2.7 Distillation of Phase-Diffused Entangled States

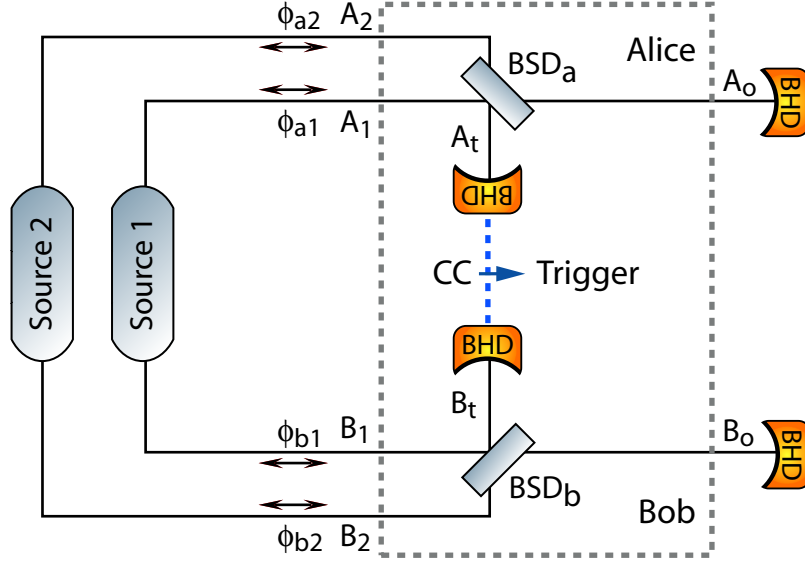


Figure 2.3 - Sketch of the entanglement distillation scenario. Source 1 and 2 each generate a pair of entangled modes, which are considered to be copies. Each of the four fields are affected by independent phase diffusion $\Phi_{1..4}$. Alice and Bob superimpose their halves of the entangled states on a 50:50 beam splitter ($BSD_{a,b}$). Balanced homodyne (BHD) was performed on one of the outputs of each beam splitter. A trigger for the validity of the output is generated via classical communication (CC).

We assume a scenario, which requires the distribution of an entangled two-mode squeezed state to Alice and Bob, see Chapter 1. During the distribution the transmitted states suffers from decoherence caused by random phase shifts for each of the subsystems. From the previous section we already know, that only the sum of the individual phases is relevant. The distillation procedure we describe here requires only local operations and classical communication, as depicted in Figure 2.3. A detailed analysis can be found in [18]. As an input the procedure needs two copies of phase-diffused entangled states. Alice and Bob each superimpose the parts of the states they received (A_1, A_2 and B_1, B_2) on a balanced beam splitter, Figure 2.3 ($BSD_{a,b}$). The interference is controlled such, that without phase diffusion it would appear in phase. They each perform a balanced homodyne measurement of the q -quadratures of one of the superimposed fields A_t and B_t . This means Alice measures: $q_A = 2^{-1/2}(q_{A_1} - q_{A_2})$, and Bob measures: $q_B = 2^{-1/2}(q_{B_1} - q_{B_2})$. They combine their measurement results via classical communication and calculate the difference: $\delta q = 2^{-1/2}(q_A - q_B)$. This displays the trigger

signal for the success of the distillation protocol. It will succeed, if $|\delta q| < Q$ turns out to be smaller than a certain adjustable value Q , similar to squeezing distillation protocol from Section 2.2.3.

Two-mode squeezing exhibits squeezing in the two commuting quadratures: $q_- = 2^{-1/2}(q_{A_0} - q_{B_0})$, and: $p_+ = 2^{-1/2}(p_{A_0} + p_{B_0})$. We quantify our entanglement by means of the total variance from Equation 2.64:

$$I = \langle (\hat{q}_-)^2 \rangle + \langle (\hat{p}_+)^2 \rangle. \quad (2.68)$$

Although the total variance is not a true entanglement measure for non-Gaussian states, it still quantifies the amount of non-local correlations and is easy accessible in the experiment. By applying the protocol both variances $\langle (\hat{q}_-)^2 \rangle$ and $\langle (\hat{p}_+)^2 \rangle$ will be decreased. Regarding q_- the situation is exactly equivalent to squeezing distillation as both the output q_- and the trigger δq represent the (non-local) squeezed quadratures. Thus we can use the same equations as in Section 2.2.3. The two independent phase fluctuations are in this case: $\phi_1 = \phi_{a1} + \phi_{b1}$, and: $\phi_2 = \phi_{a2} + \phi_{b2}$. In order to figure out the effect on the p_+ quadrature we again for a moment assume fixed phase shifts ϕ_1 and ϕ_2 . In this case measurements of both p_+ and δq show a Gaussian distribution with the variance A from Equation 2.41. For this instant our trigger condition $|\delta q| < Q$ is satisfied with a probability according to the error function $\text{erf}(Q/\sqrt{2A})$. This quantity gives us the weights for averaging the variance of p_+ properly over the phase distributions $\Phi_1(\phi_1)$ and $\Phi_2(\phi_2)$:

$$\langle (p_+)^2 \rangle = \frac{1}{\mathcal{P}} \int_{-\infty}^{\infty} \int_{-\infty}^{\infty} A \text{erf}\left(\frac{Q}{\sqrt{2A}}\right) \Phi_1(\phi_1) \Phi_2(\phi_2) d\phi_1 d\phi_2, \quad (2.69)$$

with \mathcal{P} is the overall success probability given in Equation 2.47. This weighted averaging can be understood such, that momentarily large values for A are suppressed by the momentarily small success probability $\text{erf}(Q/\sqrt{2A})$. Thus in the average for the variance of p_+ their contribution is attenuated.

For the experiments of Section 4.11 and Section 4.4 we used *v-class* entanglement, which is not explicitly treated here. The course of reasoning should be very similar, although due to the asymmetry of *v-class* entanglement the individual phases must be taken into account rather than their sums. Yet we warrantably confided in the proper functionality of the protocol, which was confirmed by the experiments, see Section 4.11. The protocol presented here can also be applied in an iterative way, as it provides the entangled output state in two open output port, which can be fed into another subsequent distillation stage, see Section 4.4.

2.3 Quantum State Measurement

2.3.1 Homodyne Detection

Virtually every continuous variable quantum optics experiment relies on homodyne detection of one or the other kind. It is based on the detection of the beat note between a strong coherent field and the signal field whose quadrature distributions are to be measured. Usually pin-photodiodes are used as photo-sensitive elements. A pin-photodiode is an insulator for a reverse bias voltage unless an electron is pushed over the band gap by the energy of a photon. Thus, the electrical current $I_{\text{PD}} = e_c \langle \hat{n} \rangle_{\text{D}}$ is proportional to the photon flux of the incident field on the detector surface D . In this section \hat{n} denotes the photon flux. Following [23], we can express \hat{n} in terms of the flux density operator $\hat{\phi}(\vec{x}, t)$ of the incident field:

$$\hat{n} = \iint_{\text{D}} \hat{\phi}^\dagger(\vec{x}_{\text{D}}, t) \hat{\phi}(\vec{x}_{\text{D}}, t) d^2x_{\text{D}}, \quad (2.70)$$

with D indicating the integration over the detector surface. For a single frequency ω the flux operator reads $\hat{\phi}(\vec{x}, t) = \hat{a}v(\vec{x})e^{-i\omega t}$, with the spatial shape determined by $v(\vec{x})$. As subject to the Helmholtz equation the spatial shape function must be composed of eigenfunctions $\{v_i\}$ of the Laplace operator, which are orthonormal:

$$\int_{-\infty}^{\infty} \int_{-\infty}^{\infty} \int_{-\infty}^{\infty} v_i^*(\vec{x})v_j(\vec{x}) d^3x = \delta_{ij}. \quad (2.71)$$

Assuming that the detector surface is large enough to cover the whole beam profile, the finite integration limits over the detector surface in Equation 2.70 can be extended over the whole x - y plane. Additionally we consider only beam-like fields propagating toward the detector surface in z -direction. This allows us to use the paraxial approximation and treat z as a time-like variable $z = ct$. A real photo diode has a finite band width corresponding to a response time τ greater than zero. This means the detector performs a temporal averaging of the incident photon flux, i.e. an integration over $z = ct$:

$$I_{\text{PD}}(t) \propto \frac{1}{\tau} \left\langle \int_{t'}^{t'+\tau} \int_{-\infty}^{\infty} \int_{-\infty}^{\infty} \hat{\phi}^\dagger(\vec{x}_{\text{D}}, t) \hat{\phi}(\vec{x}_{\text{D}}, t) dx dy dt' \right\rangle. \quad (2.72)$$

The simplest version of a homodyne detector is a single photo diode illuminated by a bright beam $\hat{\phi}_{\text{D}} = \hat{\phi}_{\text{LO}} + \hat{\phi}_{\text{s}}$ consisting of a single strong (classical) coherent field $\phi_{\text{LO}} = \alpha_{\text{LO}}v_{\text{LO}}e^{i\omega t}$ with α_{LO} chosen to be real and a weak signal component $\hat{\phi}_{\text{s}} = \sum_{\mathbf{k}} \hat{a}_{\mathbf{k}}(t)v_{\mathbf{k}}e^{i\omega t}$. Note that different spectral components of $\hat{\phi}_{\text{s}}$ are expressed by $\hat{a}_{\mathbf{k}}(t) = \int \hat{a}_{\mathbf{k}}(\Omega)e^{i\Omega t} d\Omega$.

Inserting this into Equation 2.72 we find:

$$I_{\text{PD}} \propto \left\langle \int_{t'}^{t'+\tau} \int_{-\infty}^{\infty} \int_{-\infty}^{\infty} (\hat{\phi}_{\text{LO}} + \hat{\phi}_s)^\dagger (\hat{\phi}_{\text{LO}} + \hat{\phi}_s) dx dy dt' \right\rangle$$

$$\approx \alpha_{\text{LO}}^2 + \alpha_{\text{LO}} \left\langle \sum_{\mathbf{k}} \int_{t'}^{t'+\tau} \int_{-\infty}^{\infty} \int_{-\infty}^{\infty} (\hat{a}_{\mathbf{k}}(t) + \hat{a}_{\mathbf{k}}^\dagger(t)) v_{\mathbf{k}}^* v_{\text{LO}} dx dy dt' \right\rangle + \mathcal{O}(\hat{a}_{\mathbf{k}}^2). \quad (2.73)$$

The linearization in the last line is valid provided that the local oscillator is much stronger than anything else. Under this condition, it is the spatial mode shape of the local oscillator and the time τ , which define the detection mode and the corresponding annihilation operator:

$$\hat{a}_s(t) = \int_{t'}^{t'+\tau} \int_{-\infty}^{\infty} \int_{-\infty}^{\infty} \hat{a}_{\mathbf{k}}(t) v_{\mathbf{k}}^* v_{\text{LO}} dx dy dt'. \quad (2.74)$$

Note that the detector bandwidth only sets a lower limit to τ , which is usually determined by the subsequent apparatus measuring I_{PD} . Finally, we obtain:

$$I_{\text{PD}} \propto \alpha_{\text{LO}}^2 + \alpha_{\text{LO}} \langle \hat{q}(t) \rangle = \alpha_{\text{LO}}^2 + \alpha_{\text{LO}} q(t), \quad (2.75)$$

with $\hat{q}(t) = \hat{a}_s(t) + \hat{a}_s^\dagger(t)$ denoting the amplitude quadrature operator and q the amplitude quadrature amplitude.

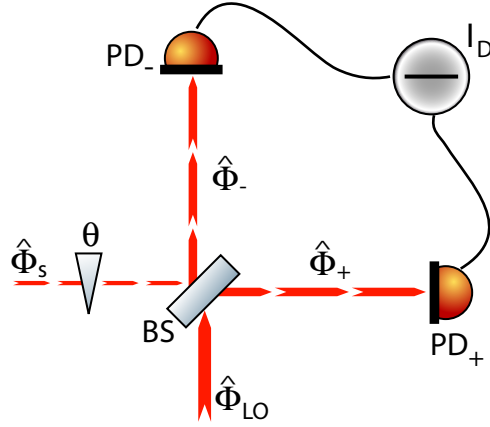


Figure 2.4 - Sketch of a balanced homodyne detector. The balanced beam splitter is used to superimpose the signal $\hat{\Phi}_s$ and the strong local oscillator $\hat{\Phi}_{\text{LO}}$. A phase shifter can tune the mutual phase θ of the local oscillator and the signal.

If not only the amplitude quadrature needs to be measured – like in the case of tomography or for the evaluation of entanglement criteria – a more flexible setup will be required. A balanced homodyne detector, see Figure 2.4 displays exactly this feature.

A balanced beam splitter is used to superimpose the strong (classical) local oscillator $\Phi_{\text{LO}} = [\alpha_{\text{LO}}^0 + \alpha_{\text{LO}}(t)]v(\vec{x})e^{i\omega t}$ with noise represented by $\alpha_{\text{LO}}^0(t)$ and the signal $\hat{\Phi}_s$ defined as above. The phase θ of the signal is adjustable and referenced such that for $\theta = 0$ the two fields are in phase, accounting for all other phase shifts that occur at the beam splitter. For the output ports of the beam splitter $\hat{\Phi}_{\pm}$ we obtain the sum and the difference of the two inputs due to the energy conserving phase flip of the beam splitter:

$$\hat{\Phi}_{\pm} = \frac{1}{\sqrt{2}}(\Phi_{\text{LO}} \pm e^{i\theta}\hat{\Phi}_s). \quad (2.76)$$

Following the above considerations and assuming perfect spatial mode matching of the two fields we obtain for currents I_{\pm} of the two detector in the output ports PD₊ and PD₋:

$$I_{\pm} \propto [\alpha_{\text{LO}}^0 + \alpha_{\text{LO}}(t)]^2 \pm [\alpha_{\text{LO}}^0 + \alpha_{\text{LO}}(t)]\langle e^{i\theta}\hat{a}_s + e^{-i\theta}\hat{a}_s^\dagger \rangle + \langle \hat{a}_s^\dagger\hat{a}_s + h.c. \rangle. \quad (2.77)$$

If we assume that α_{LO}^0 will by far be the strongest component the difference of the two detector currents $I_D = I_+ - I_-$ simplifies to:

$$\begin{aligned} I_D &\propto \alpha_{\text{LO}}^0 \langle e^{i\theta}\hat{a}_s + e^{-i\theta}\hat{a}_s^\dagger \rangle \\ &=: \alpha_{\text{LO}}^0 \langle \hat{q}_\theta \rangle, \end{aligned} \quad (2.78)$$

with $\hat{q}_\theta = \hat{q} \cos \theta + \hat{p} \sin \theta$ being a rotated quadrature in phase space, which is composed of the amplitude quadrature \hat{q} and the phase quadrature \hat{p} . Hence, a BHD can measure a rotated quadrature component of the signal field with the rotation angle determined by the mutual optical phase of signal and local oscillator. Also note that the noise on the local oscillator is canceled by the subtraction.

On the other hand, the sum of the two detector currents: $I_S = I_+ + I_-$ does not contain the interference terms:

$$I_S \propto [\alpha_{\text{LO}}^0 + \alpha_{\text{LO}}(t)]^2 + \langle \hat{a}_s^\dagger\hat{a}_s + h.c. \rangle. \quad (2.79)$$

This equals the sum of the individual detection of the local oscillator and the signal.

For a typical experiment however, there is usually a lot of technical noise in the low frequency components of \hat{a}_s and hence also in I_D , which covers any quantum signal. This necessitates to observe only those parts of the spectrum, which are free of technical noise. Without loss of generality we consider only the amplitude quadrature. With the tilde denoting the Fourier transform we obtain:

$$\begin{aligned} \tilde{I}_D(\Omega) &\propto \langle \tilde{\hat{q}}(\Omega) \rangle \\ &= \langle \tilde{\hat{a}}_s(\Omega) + \tilde{\hat{a}}_s^\dagger(\Omega) \rangle \\ &= \langle \tilde{\hat{a}}_s(\Omega) + \tilde{\hat{a}}_s^\dagger(-\Omega) \rangle, \end{aligned} \quad (2.80)$$

with the last line being the property of the Fourier transform under conjugation. Thus, the frequency components of I_D correspond to two fields at different optical frequencies centered around the fundamental frequency ω . We call this a modulation mode, see [41, 42]¹ for the algebra, which turns out to behave just like ordinary bosonic operators. The modulation modes perfectly suit the description of an OPA, which emits pairs of photons with frequencies $\omega \pm \Omega$. Note that a mean value of $\tilde{q}(\Omega)$ or $\tilde{p}(\Omega)$ different from zero corresponds to a classical amplitude or phase modulation at the frequency Ω . This means that coherent states of the modulation mode are classical modulations. In summary, the detection mode of a BHD is defined by the mode – the spatial shape, the frequency and polarization – of the local oscillator, the time for which the photocurrent is recorded and the choice of spectral components of the BHD signal. Regarding the spatial mode matching a special case related to many experimental implementations can be considered. In most cases the signal under consideration is prepared in a single spatial mode (TEM₀₀) while all other modes carry the vacuum. The experimentalist's goal is to match this signal mode to the local oscillator at the BHD which works really good but not perfect. The mode matching is usually quantified by the visibility v . The light power P_o in one of a balanced beam splitter output ports for fields of equal frequencies at the input ports is given by

$$P_o = \frac{1}{2} \left(P_1 + P_2 + 2v \sqrt{P_1 P_2} \cos \theta \right), \quad (2.81)$$

with P_1 and P_2 being the powers of the input fields and the mutual phase θ of the input fields in the output port. With respect to θ there is a minimal P_{\min} and a maximal power P_{\max} in the output ports, which – given equal input powers – yields the visibility via:

$$v = \frac{P_{\max} - P_{\min}}{P_{\max} + P_{\min}} = 1 - 2 \frac{P_{\min}}{P_{\max} + P_{\min}} \approx 1 - 2 \frac{P_{\min}}{P_{\max}}, \text{ for small } P_{\min}. \quad (2.82)$$

Note that the power is proportional to the flux via the photon energy. How does a visibility smaller than unity affect the measurement? Using the spatial mode $v(\vec{x})$ of the local oscillator and $v_s(\vec{x})$ of the excited mode of the signal, we define the quantity

$$\sqrt{\eta_{\text{mm}}} = \iiint v_s^*(\vec{x}) v(\vec{x}) d^3x, \quad (2.83)$$

with $v_s(\vec{x})$ referenced such, that a non-negative real number is obtained. From the annihilation operators $\hat{a}_{0,k}$ of all modes $v_{0,k}$ of the vacuum part of the signal field, i.e. all modes but the excited TEM₀₀, the operator \hat{a}_v can be spawned:

$$\sqrt{1 - \eta_{\text{mm}}} \hat{a}_v = \sum_k \hat{a}_{0,k} \iiint v_{0,k}^*(\vec{x}) v(\vec{x}) d^3x. \quad (2.84)$$

¹ Note that Caves and Shumaker term a single squeezed beam *two mode squeezing* because of the two optical frequencies at $\omega \pm \Omega$, which contribute to the squeezing of the modulation mode. Nowadays in contrast, the term *two mode squeezing* often refers to an entangled state, which is a superposition of two squeezed modulation modes. Thus, *single mode squeezing* usually refers to the squeezing of a single modulation mode. For Caves and Shumaker this was the degenerate limit ($\Omega \rightarrow 0$).

Thus, the annihilation operator \hat{a} of the mode perfectly matching the local oscillator can be constructed:

$$\hat{a} = \sqrt{\eta_{\text{mm}}}\hat{a}_s + \sqrt{1 - \eta_{\text{mm}}}\hat{a}_v. \quad (2.85)$$

It can be shown that \hat{a}_v is an ordinary bosonic annihilation operator corresponding to a vacuum mode. Thus, an imperfect mode matching in this case leads to exactly the same situation as for loss modelled by a beam splitter with transmittance η_{mm} . The relation to the visibility v can be obtained by putting the fields considered here into Equation 2.73 with an extra phase for the signal flux:

$$v^2 = \eta_{\text{mm}}. \quad (2.86)$$

Until now we have assumed a perfect photo detection efficiency. However, a real photo detector shows an efficiency η_D smaller than unity, which is modeled by a beam splitter of transmittance η_D in front of an ideal photo detector. In the case of the balanced homodyne detector, Figure 2.4, the fields toward the individual detectors $2^{-1/2}(\hat{a}_{\text{LO}} \pm \hat{a}_s)$ must be replaced by $2^{-1/2}\eta_D^{1/2}(\hat{a}_{\text{LO}} \pm \hat{a}_s) + (1 - \eta_D)^{1/2}\hat{a}_{v\pm}$. For the sake of clarity we assume a single signal mode and perfect mode matching and instead of Equation 2.77 for the difference current we obtain:

$$I_D \propto \alpha_{\text{LO}} \left\langle \eta_D \hat{q}_\theta + \frac{1}{2} \sqrt{1 - \eta_D} \sqrt{\eta_D} \left(e^{-i\theta} (\hat{a}_{v+} - \hat{a}_{v-}) + e^{i\theta} (\hat{a}_{v+}^\dagger - \hat{a}_{v-}^\dagger) \right) \right\rangle. \quad (2.87)$$

This expression is simplified by tracing $\hat{a}_{v\pm}$ back through the beam splitter and using a local oscillator $\alpha'_{\text{LO}} = \sqrt{\eta_D} \alpha_{\text{LO}}$ compensating the loss:

$$I_D \propto \alpha'_{\text{LO}} \left\langle \sqrt{\eta_D} \hat{q}_\theta + \sqrt{1 - \eta_D} \hat{q}_{\theta,v} \right\rangle, \quad (2.88)$$

with $\hat{q}_{\theta,v}$ corresponding to a vacuum mode which matches the signal. Hence, for balanced homodyne detection non-unit detection efficiency can be modeled by loss on the signal field.

2.3.2 Quantum State Tomography

The imaging of an object's cross-sections which in general are located inside the object and not accessible directly is referred to as *tomography*. Although not being accessible, an image of the cross-section can be tomographically reconstructed from its marginal projections for many different directions [43]. Nowadays, the concept of tomography displays a widely used imaging and analyzing technique in various fields. Most prominently tomography constitutes an important technique in medical diagnostics. The two most important techniques are nuclear magnetic resonance tomography and computer-aided X-ray tomography (CT). The latter gives an ostensive example of the flavour of tomography:



Figure 2.5 - Illustration of X-ray tomography. The central picture represents a slice of a human head with different tissues exhibiting different X-ray absorption. The slice is illuminated with X-rays from various angles. The stripes distributed around the central picture represent the X-ray shadow for the corresponding angle. From these shadow images the central image can be reconstructed via the so called inverse Radon transform.

The various tissues in the human body show different X-ray absorption coefficients, which attenuate a beam passing through the body according to the integrated absorption along the direction of propagation. These marginal projections are taken from many different directions, i.e. the X-ray source and screen are rotated around the body, yielding a *shadow* of the cross-section under consideration for each direction, see Figure 2.5. From these shadows the image of two dimensional cross-sections of the human body can be reconstructed, see Figure 2.7 and Figure 2.6.

The spatial resolution of the reconstructed image depends on the spatial resolution of the *shadow* detector itself, see Figure 2.6. Thus, the size of the smallest structure, which is intended to be reconstructed, determines the pixel size of the detector. However, smaller pixels require a higher X-rays flux density to maintain a reasonable signal to noise ratio for each pixel. Hence, in case of X-ray tomography the acceptable effective radiation dose limits the pixel size. The effective dose for X-ray tomography varies in the range of one to ten millisievert (mSv). A typical chest X-ray screening yields 0.1 mSv. In Germany the natural background dose ranges from 0.5 mSv in the northern lowlands to 2 mSv in the mountains of the Erzgebirge.

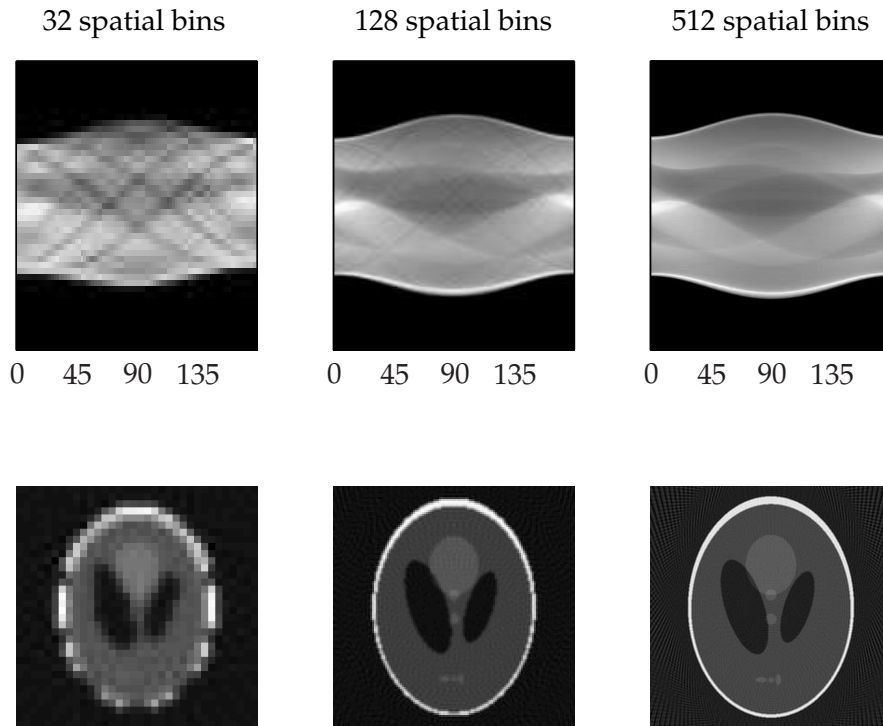


Figure 2.6 - Lower row: Tomographic reconstructions for different spatial resolutions (columns). The angular resolution is fixed at 2° . The upper row displays the projections for all angles (x-axis).

The angular resolution, i.e. the number of different directions of illumination per revolution has a less obvious impact on the resolution. Here, not only the size but also the shape and the location of the smallest structure to be resolved is crucial. The stronger the angular variation of a structures contribution to the absorption is, the higher is the angular resolution required to resolve this structure. This is displayed in Figure 2.7. The tiny light grey disks in the centre already show up in the left most column with only eight projections, while the three light grey structures in the lower part of the figure can only be distinguished with the highest angular resolution. However, increasing the angular resolution necessitates increasing the number of projections and thus the total X-ray dose.

The above considerations come in handy when it comes to quantum state tomography (QT). In general, we cannot determine all properties of a quantum state at a time, because of Heisenberg's uncertainty relation. A quantum state cannot be represented by a single dot in the phase space spanned by two non-commuting observables. We cannot e.g. determine position and momentum of a particle or amplitude and phase quadrature of a light mode (one of the objectives of this thesis) simultaneously. What we want to image is obscured by the thing itself. All we can do, is to measure the projection of one of these quantities at a time. Believing in the ergodic hypothesis to acquire the knowledge of the statistics of a state is not necessary to perform measurements on a whole ensemble, but it is equivalent to prepare many individuals the same way one at

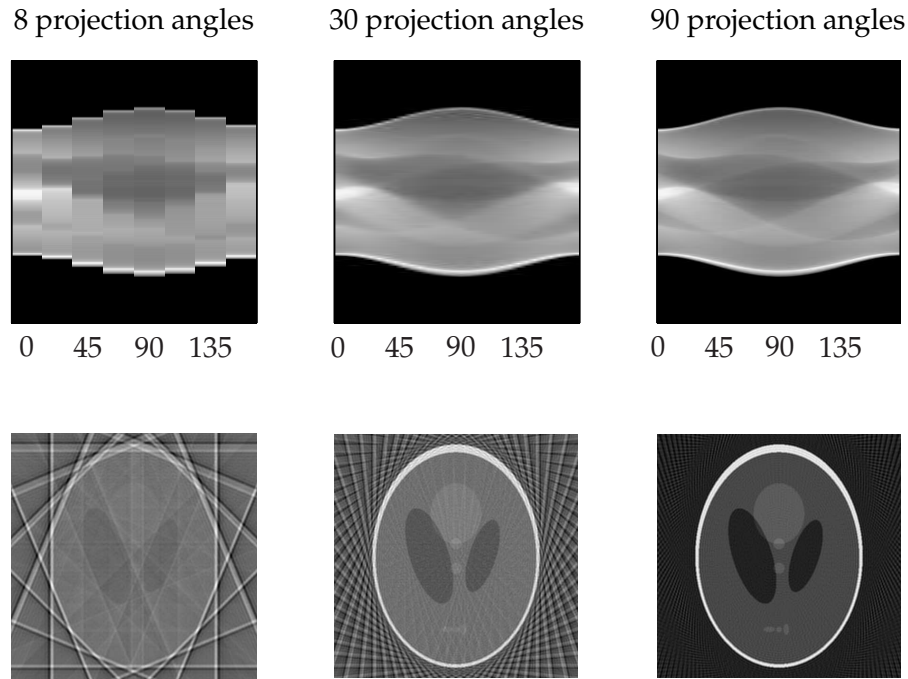


Figure 2.7 - Lower row: Tomographic reconstruction for different angular resolutions ranging from 22.5° to 2° . The spatial resolution is set to 512 bins. The upper row displays the projections for all angles (x-axis).

a time and perform measurements on each. With a reliable state preparator it is possible to measure the probability distribution of e.g. a light mode's amplitude quadrature and take it as a state's (estimated) probability density for this quantity. At a different time the phase quadrature or any quadrature rotated arbitrarily in phase space can be addressed.

In quantum mechanics there is an object in phase space whose marginal projections for different directions yield the probability densities for the corresponding quantity. This is the Wigner function, which uniquely characterizes a state. An integral over the Wigner function in a certain direction in phase space results in the probability density for the corresponding quantity similar to the integrated X-ray absorption results in the shadow along the beam direction, see [44]. As this is equivalent in the case of the CT, the same procedure can be used to reconstruct the Wigner function from its measurable projections, which is called quantum state tomography. The analogy goes even further. While in case of CT the imaging quality is limited by the acceptable radiation dose, in case of QT it is limited by the finite number of ensemble representatives because of a finite flux of the state preparator on the one hand and a finite time you are able to sit in the laboratory on the other hand.

Turning to the scope of this thesis, for the quantum state tomography of a light mode the shadow detection for different directions corresponds to the measurement of probability distributions $prd(q_\theta)$ of differently rotated (θ) quadratures q_θ , which are

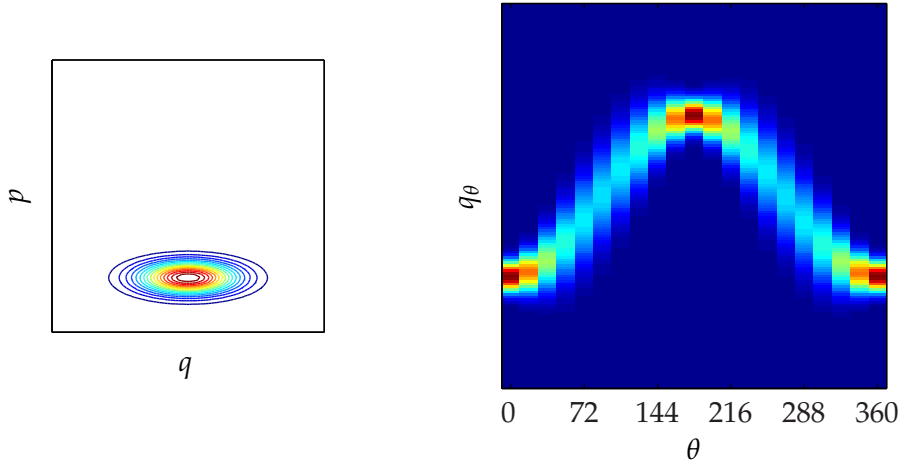


Figure 2.8 - Left: Wigner function of a bright squeezed state. Right: Marginal probability distribution with the projection angle θ on the x -axis. For the sake of clarity the projections are shown for a full revolution, although half a revolution already contains all information as the second half is nothing more than a mirror image of the first. The angular resolution is 18° , which is sufficient for a good reconstruction due to the simple angular structure of the Wigner function.

known to be the marginals of the Wigner function $W(q, p)$, see Section 2.1.2 and Figure 2.8 for an illustration:

$$prd(q_\theta) = \int_{-\infty}^{\infty} W(q \cos \theta - p \sin \theta, q \sin \theta + p \cos \theta) dp. \quad (2.89)$$

This is experimentally accomplished by varying the optical detection phase of a balanced homodyne detector (BHD), see Section 2.3.1. The histograms of the measurement values for a reasonable amount of samples of the BHD signal form the probability distribution for the quadrature rotated corresponding to the detection phase: $prd(q_\theta) = \langle q | \hat{U}(\theta) \hat{\rho} \hat{U}^\dagger(\theta) | q \rangle$ with the phase shift operator $\hat{U}(\theta)$, see Section 2.1. Of course, it is necessary to precisely know the detection phase. Thus, the mutual phase of signal and local oscillator has to be measured, see Section A.1, where a scheme is presented, which yields a signal linear in phase for an arbitrary phase. Given this, the experimental procedure of addressing the necessary phase settings can be used to build a control loop which controls the homodyne detection phase at a tunable set point from the predefined set of different phases. Once a phase is set and a reasonable number of measurements is recorded, the homodyne detector is tuned to the next set point, which is the procedure for the presented work as well as for the pioneering experiment carried out by Smithey, Beck, Raymer, and Faridani in 1993 [45]. However, sometimes the experiment is yet too complex or simply not focussed on tomography and a full phase readout scheme is unavailable. Usually, even in this case there is a signal depending sinusoidally on the detection phase, which can be used to determine the phase at least twice per revolution. The phase can then be swept under the assumptions that the sweep is linear in time or at least representable by a low order polynomial. In the latter case, a fit of the sinusoidal signal can be used to determine the polynomial coefficients.

The continuous stream of sampled homodyne data can be sliced into pieces according to the desired set of phases, see [46]. For an implementation at the AEI, see [47].

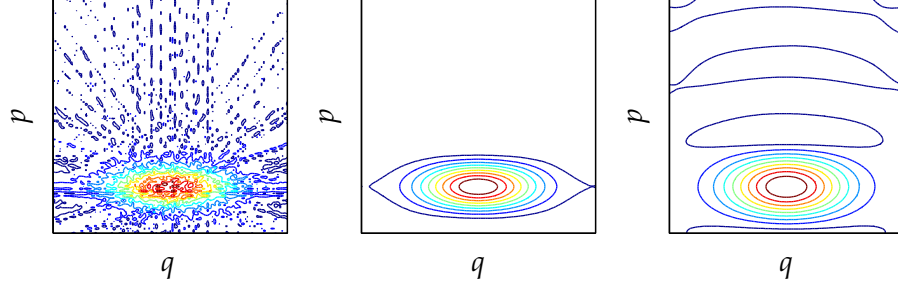


Figure 2.9 - Reconstructed Wigner functions of a bright squeezed state with statistical noise corresponding to 100 000 BHD signal samples for each of the ten projections. Left: Filtered back projection with no additional filtering applied but what is necessary for a stable integration, see Equation 2.97. Middle: Optimal filtering suppressing the fine ripples caused by statistics without changing the structure of the Wigner function. Right: Excessive filtering detecting the Wigner function itself as a *ripple*.

The reconstruction of the Wigner function from its projections is based on the approach to Wigner's formula, Equation 2.20, and the fact, that the characteristic functions $\widetilde{prd}(u_\theta, \theta)$, i.e. its Fourier transform, of the marginal probability distributions are polar cuts according to the projection angle θ through the characteristic function $\widetilde{W}(u, v)$ of the Wigner function:

$$\widetilde{prd}(u_\theta, \theta) = \widetilde{W}(u_\theta \cos \theta, u_\theta \sin \theta). \quad (2.90)$$

The inverse Fourier transform yields the Wigner function from its characteristic function. In polar coordinates that is:

$$\begin{aligned} W(q, p) &= \frac{1}{(2\pi)^2} \int_{-\infty}^{\infty} \int_0^{\pi} \widetilde{W}(u \cos \theta, u \sin \theta) |u| e^{iu(q \cos \theta + p \sin \theta)} du d\theta \\ &= \frac{1}{(2\pi)^2} \int_{-\infty}^{\infty} \int_0^{\pi} \int_{-\infty}^{\infty} prd(x, \theta) e^{iu(q \cos \theta + p \sin \theta - x)} du d\theta dx, \end{aligned} \quad (2.91)$$

which is nice to know but lacks usability. As the prd function does not care about the u -integration, we can introduce the kernel $K(z)$:

$$K(z) = 1/2 \int_{-\infty}^{\infty} |u| e^{iuz} du, \quad (2.92)$$

and obtain a simpler result:

$$W(p, q) = \frac{1}{(2\pi)^2} \int_0^\pi \int_{-\infty}^{\infty} prd(x, \theta) K(q \cos \theta + p \sin \theta - x) d\theta dx. \quad (2.93)$$

The kernel, Equation 2.92, can be treated with quite a bit of maths to end up with the expression $K(z) = -P/x^{-2}$ for the integral in Equation 2.93 equivalent to Cauchy's principal value P , see [23, 48]. This results in a decent expression for the so called inverse Radon transform, which shows how to calculate the Wigner function from a given probability $prd(x, \theta)$:

$$W(p, q) = -\frac{P}{(2\pi)^2} \int_0^\pi \int_{-\infty}^{\infty} \frac{prd(x, \theta)}{(q \cos \theta + p \sin \theta - x)^2} d\theta dx. \quad (2.94)$$

However, a numerical approach certainly requires additional considerations because of the unbound kernel, which brings us to filtering and the *filtered back projection* implementation of the inverse Radon transform. It is reasonable to assume, that the Wigner function does not oscillate with arbitrary high frequencies and that it tends to zero far from the origin. Given this a cut off frequency k_c can be introduced for Equation 2.92:

$$K(z) = 1/2 \int_{-k_c}^{k_c} |u| e^{iuz} du \quad (2.95)$$

$$= (\cos(k_c x) + k_c x \sin(k_c x) - 1) / x^2 \quad (2.96)$$

$$\approx \frac{k_c^2}{2} \left[1 - \frac{k_c^2 x^2}{4} + \frac{k_c^4 x^4}{72} \right]. \quad (2.97)$$

A save choice for z_c to switch from Equation 2.96 to the numerically stable Equation 2.97 is $|k_c z_c| \leq 0.1$. The right choice of k_c depends on the structure of the Wigner function, i.e. its finest structures. A fast implementation of the x convolution in Equation 2.93 can be done using the Fourier transform. The phase integration turns into a sum over the set of tomographically measured phases. Fortunately, such an algorithm is readily implemented in MATLAB, which also supports more sophisticated filtering than the simple cut off. Many interesting things about filtering and the corresponding window function can be found in e.g. [49]. Additionally, see Section 4.1 about how to directly sample the characteristic function.

The same considerations as for the single mode tomography above hold in case of two mode tomography, see [50]. The corresponding four dimensional Wigner function $W(q_1, p_1, q_2, p_2)$ lives in a phase space spanned by the two conjugate quadratures of each of the two modes involved. A projection of the Wigner function on a plane $q_{1\theta}, q_{2\phi}$ yields the joint probability distribution $prd(q_{1\theta}, q_{2\phi})$, see Figure 2.10. This can be thought of as first projecting in the first mode's plane to obtain $wp(q_{1\theta}, q_2, p_2)$ and a subsequent projection in the second mode's plane to obtain $prd(q_{1\theta}, q_{2\phi})$, which is

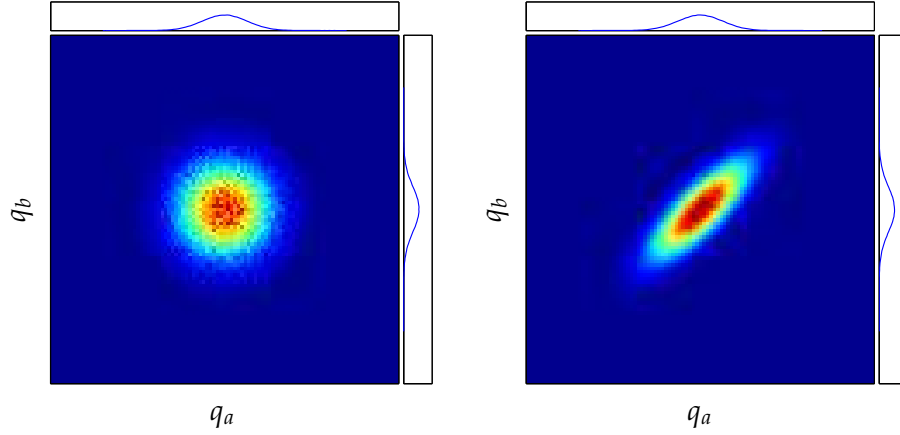


Figure 2.10 - Joint probability distributions (big boxes) from two simultaneously sampled BHDs and individual probability distributions (small boxes surrounding the big ones) of the individual detectors. In a two mode scheme it is not sufficient to record individual probability distributions. The individuals look identical in both cases, while only the joint probability distributions reveal that the two modes in the left case are independent and that there is a correlation (possibly entanglement) on the right.

identical to two subsequent Radon transforms as described above. Thus, also the inversion is already known. First, $prd(q_{1\theta}, q_{2\phi})$ must be inverted with respect to the second mode, i.e. for each combination of $q_{1\theta}, \theta$. The result is $wp(q_{1\theta}, q_2, p_2)$, which now has to be inverted for every combination of q_2, p_2 to yield the two mode Winger function $W(q_1, p_1, q_2, p_2)$. The joint probability distributions can be gained from simultaneously sampling the signal of the first BHD tuned to θ and the second BHD tuned to ϕ . While in the single mode case only a single inverse Radon transform has to be applied, there are of order of 100 000 inversions necessary in the two mode case.

In addition to reconstructing the state's Wigner function based on the tomographic data, it is also possible to reconstruct or rather directly sample the density matrix. If we replace the operator $\hat{\rho}$ in Wigner's formula, Equation 2.20, by the projector for a density matrix element $|a\rangle\langle a'|$, we will obtain the Wigner representation $W_{a'a}(q, p)$ of this projector. The corresponding density matrix element $\rho_{a'a}$ of a given Wigner function $W(q, p)$ can be obtained by overlap integration of $W(q, p)$ and $W_{a'a}(q, p)$:

$$\rho_{a'a} = 2\pi \int_{-\infty}^{\infty} \int_{-\infty}^{\infty} W(q, p) W_{a'a}(q, p) dq dp. \quad (2.98)$$

This as well as the inverse Radon transform is a linear integral transform. As such, a linear expression for the density matrix elements in terms of the probability distributions

must exist:

$$\rho_{a'a} = \int_0^\pi \int_{-\infty}^\infty \text{prd}(q, \theta) F_{a'a}(q, \theta) dq d\theta \quad (2.99)$$

$$= \underbrace{\langle \langle F_{a'a}(q, \theta) \rangle \rangle_{q, \theta}}_{\text{weighted average}}. \quad (2.100)$$

The interesting aspect occurs in the second line. Given the right pattern functions $F_{a'a}(q, \theta)$ for the density matrix, every measurement value of the BHD individually contributes to the density matrix. Thus, the density matrix can be grown by averaging over the individual contributions. This avoids the detour via the Wigner function as well as the filtering, which is necessary for the inverse Radon transform. However, the hard part is to find the right pattern functions for the basis of choice of the density matrix, which can be found in [23, 51, 52].

By combining Equation 2.94 and Equation 2.98 via the characteristic function the expression:

$$\rho_{a'a} = -\frac{P}{\pi} \int_0^\pi \int_{-\infty}^\infty \int_{-\infty}^\infty \frac{\text{prd}(q, \theta) \text{prd}_{a'a}(x, \theta)}{(q-x)^2} dq dx d\theta, \quad (2.101)$$

can be found for the matrix element $\rho_{a'a}$ with the generalized probability functions:

$$\text{prd}_{a'a}(x, \theta) = \langle x | \hat{U}(\theta) | a \rangle \langle a' | \hat{U}^\dagger(\theta) | x \rangle. \quad (2.102)$$

This is just the ordinary formula for the probability distribution with the density operator ρ replaced by the projector $|a\rangle\langle a'|$ and the phase shift operator $\hat{U}(\theta)$.

Choosing the Fock states as a basis the expression Equation 2.102 turns into:

$$\text{prd}_{mn}(x, \theta) = \psi_m(x) \psi_n(x) e^{i(m-n)\theta}, \quad (2.103)$$

with the wave functions $\psi(x)$ of the Fock states $|n\rangle$. Due to the simple phase dependence of the Fock wave functions for the pattern functions we obtain likewise:

$$F_{mn}(q, \theta) = \frac{1}{\pi} f_{mn}(q) e^{i(m-n)\theta}. \quad (2.104)$$

with the real amplitude pattern functions $f_{mn}(q)$ which now can be read from Equation 2.101 and comparing it with Equation 2.99 to be:

$$f_{mn}(q) = -P \int_{-\infty}^\infty \frac{\psi_m(x) \psi_n(x)}{(q-x)^2} dx. \quad (2.105)$$

There was a surprisingly simple formulation for f_{mn} found in [53]:

$$f_{mn}(q) = \partial_x [\psi_m(x)\phi_n(x)]. \quad (2.106)$$

The irregular wave functions $\phi_n(x)$ are the solutions of the Schrödinger equation for the same frequency as for $\psi_n(x)$. Usually they are discarded as they are not normalizable. For a numerical implementation there is a nice recipe in [23] providing a fast and stable computational algorithm for the numerical generation of the pattern functions. This algorithm is based on a stable iterative scheme derived from the algebraic relations among the wave functions. Given this nice formula a general basis can be expressed in the usual way:

$$\rho_{a'a} = \sum_{mn} \rho_{mn} \langle a' | m \rangle \langle n | a \rangle. \quad (2.107)$$

Corresponding to the basis states $|a\rangle$ the time dependent regular wave functions $\psi_a(x, t)$ can be composed from the Fock wave functions:

$$\psi_a(x, t) = \sum_n \langle n | a \rangle \psi_n e^{-i\omega_n t}, \quad (2.108)$$

and likewise for the irregular solutions $\phi_a(x, t)$. This ends up in a simple and yet general formula for the direct sampling of the state in an arbitrary basis:

$$\rho_{a'a} = \langle \langle \partial_x [\psi_{a'}^*(x)\phi_a(x)] \rangle \rangle_{x,t}. \quad (2.109)$$

The concept of state sampling can be expanded to the two mode case as shown in [50]. The tomographic completeness of the measurement with two BHDs is derived in [54]. Note that the completeness also applies to the single mode measurement. For the sampling of the joint density matrix we restrict ourselves to the Fock basis with the matrix elements ρ_{nmjk} :

$$\rho_{nmjk} = \langle n |_a \langle j |_b \hat{\rho} | k \rangle_b | m \rangle_a \quad (2.110)$$

$$= \int_0^\pi \int_{-\infty}^\infty \int_0^\pi \int_{-\infty}^\infty S_{nm}^{jk}(q_a, \theta, q_b, \beta) d\theta dq_a d\beta dq_b \quad (2.111)$$

$$= \langle \langle S_{nm}^{jk}(q_a, \theta, q_b, \beta) \rangle \rangle_{q_a, \theta, q_b, \beta}. \quad (2.112)$$

The subscripts refer to the modes with the detection phases θ at *Alice's* and β at *Bob's* BHDs. The functions $S_{nm}^{jk}(q_a, \theta, q_b, \beta)$ are the pattern functions for a joint density matrix, which is due to the independently measurable degrees of freedom just the product of the single mode sampling functions:

$$S_{nm}^{jk}(q_a, \theta, q_b, \beta) = F_{nm}(q_a, \theta) F_{nm}(q_b, \beta). \quad (2.113)$$

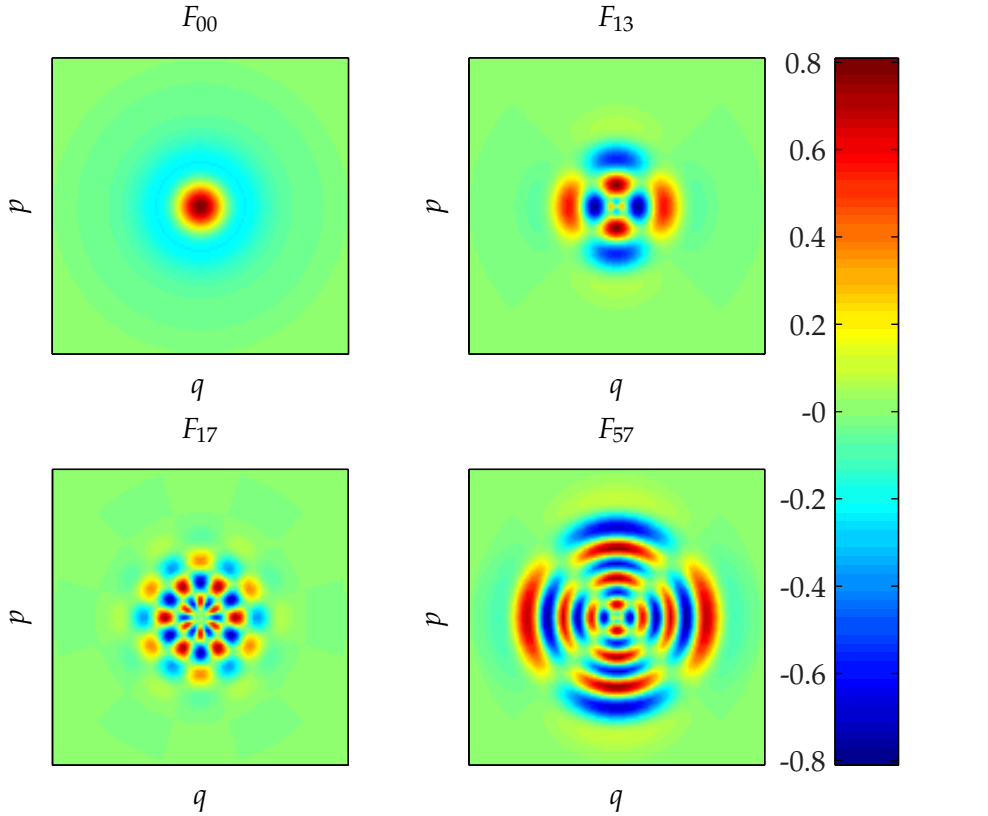


Figure 2.11 - Real part of the pattern functions F_{mn} for different n and m . The angular complexity (number of nodes) is proportional to the photon number difference, while the radial complexity scales with the mean photon number. The overall stretch in phase space depends on the smaller photon number. Thus, as an a priori assumption regarding the maximum significant photon number can be used to estimate the angular and quadrature resolution for the state tomography.

Finally, possible errors in the reconstruction need to be considered. The whole process of tomography works in a discrete manner. First, we consider, that the angular detection interval has to be sliced in a finite set of discrete phases. Secondly, also the quadrature resolution is discrete, because the data acquisition necessarily involves an analogue to digital converter with a finite resolution. Third, the measurement can only last a finite time per detection phase. Hence, there are statistical fluctuations which need to be taken into account.

From Figure 2.11 we can derive a hand waving argument for the number of tomography phases required for a certain number of components of the reconstructed density matrix. As the number of angular nodes in $F_{mn}(q, \theta)$ in the interval $[0, \pi]$ matches the photon number difference, aliasing can occur if the number of detection phases is exceeded. Thus, the angular resolution limits the maximum photon number of the reconstructed density matrix, which equals the largest photon number difference occurring. A detailed analysis can be found in [55]. We will stick to the rule "*maximum photon*

number \leq *tomography phases*".

The second aspect to be read from Figure 2.11 is the radial dependence of the pattern function on the photon number. The frequency of the oscillation in radial direction grows with the photon number. Thus, the quadrature resolution must also increase with the maximum photon number M to be reconstructed. Based on finding an approximation for the frequency of the oscillation in [23] the quadrature period q_M of the most rapid oscillation is found to be:

$$q_M = \frac{\pi}{\sqrt{2M+1}}. \quad (2.114)$$

Aiming at a certain M in the reconstruction this sets an upper limit to the bin width of the quadrature resolution, which should be at least $q_M/2$. This was easily fulfilled by the data acquisition hardware described in Section 3.5 and it was even possible to merge two or more adjacent bins.

For the approach to the statistical error we consider a single bin in the tomography process, i.e. a single quadrature bin at a certain detection phase. The probability of a measurement falling into this bin is given by $prd(q, \theta)$. The filling process is Poissonian as it displays a quantum random number generator. As such the variance is known to be:

$$\sigma_{q,\theta}^2 = \frac{\pi}{N_\theta} prd(q, \theta), \quad (2.115)$$

with N_θ denoting the number of measurements for each detection phase. The filling of each bin is independent from the others. Thus, we can use Equation 2.99 and Equation 2.104 to obtain the variance for the real part of the reconstructed matrix elements caused by statistical fluctuations:

$$\sigma_{mn}^2 = \frac{1}{\pi^2} \int_0^\pi \int_{-\infty}^\infty \sigma_{q,\theta}^2 f_{mn}^2(q) \cos[(n-m)\theta] dq d\theta. \quad (2.116)$$

As the tomography is run in the regime of large numbers N of measurements, for this purpose of estimating the variance directly from the measurement the *ideal* quantum mechanical probability can be identified with the measurement and we can use Equation 2.115 to obtain:

$$\sigma_{mn}^2 = \left\langle \left\langle \frac{1}{\pi N_\theta} f_{mn}^2(q) \cos[(n-m)\theta] \right\rangle \right\rangle_{q,\theta}. \quad (2.117)$$

The same holds for the imaginary part with the sine instead of the cosine.

Key Components of the Experiments

3.1 Laser Sources

Three phase-locked coherent single-mode continuous-wave laser fields were employed for different purposes in the experiments. One field was used as a local oscillator in the homodyne detectors and for control of the squeezed light sources. It is referred to as *fundamental* beam at the near infrared (NIR) wavelength of 1064 nm. A second NIR laser was phase-locked to the fundamental one with a radio frequency offset. The second laser was used for the phase read out and control of the homodyne detectors and is referred to as *auxiliary* laser. The third field oscillated at exactly twice the frequency of the fundamental one and was generated by a second-harmonic generator (SHG) based on $\chi^{(2)}$ non-linear frequency doubling. This field pumped the optical parametric amplifiers and hence is referred to as *pump*. There were several considerations which led us to choosing the wavelength of 1064 nm and 532 nm: First of all, there were well matured, ultra stable, high-power lasers available, which had shown an excellent performance in the squeezing laboratories around the world for years. Secondly, PIN photo detectors at the crucial wavelength of 1064 nm were highly efficient. Thirdly, high quality optical components were available from stock and, after all, these wavelengths were common in the scientific community.

3.1.1 Main Laser

As the main laser source we chose the model Diablo from the local manufacturer InnoLight. This device was a diode pumped solid state laser at 1064 nm with an integrated frequency doubling unit. It provided 350 mW of NIR and 800 mW of green light power each in a single mode.

The active medium for the NIR laser was neodymium doped yttrium aluminium garnet (Nd:YAG) forming a monolithic non-planar ring oscillator (NPRO) pumped by two laser diode arrays at 809 nm. The monolithic nature of the laser cavity ensured a

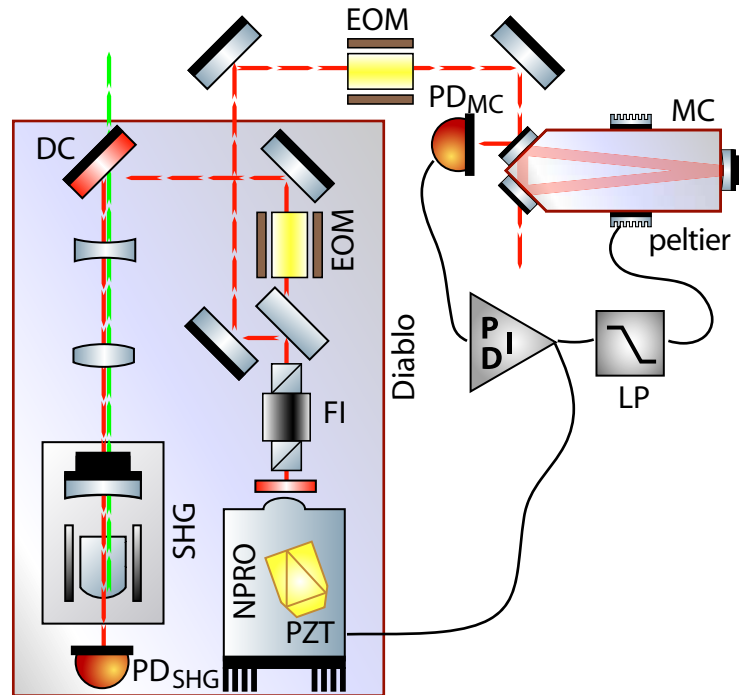


Figure 3.1 - A sketch of the inside of the Diablo with mode cleaning setup. NPRO: NIR laser inside the Diablo. SHG: second-harmonic generator. PD: photo diode. EOM: electro optical modulator. FI: Faraday isolator. MC: mode cleaner. LP: integrator. Peltier: Peltier thermo element attached to MC spacer.

high mechanical stability and thus a high optical frequency stability. The temperature of the laser crystal was stabilized to achieve long term stability.

The laser frequency could be actuated in two ways. Firstly, the set point of the crystal temperature stabilization could be changed yielding a tuning range of up to 30 GHz with -3 GHz per Kelvin and a bandwidth of 1 Hz. Secondly, there was a tiny piezoelectrical crystal transducer (PZT) attached to laser crystal cavity. By slightly squeezing and thus applying stress to the laser crystal, the PZT affected the cavity resonance frequency and thus the laser field. This alternative provided a significantly higher bandwidth of 100 kHz and a tuning range of ± 100 MHz at roughly 1 MHz per Volt.

The laser operated in the so-called *class-B-regime*, with the upper-state lifetime being longer than the cavity damping time. In this regime, changes or fluctuations in pump power led to so-called *relaxation oscillations*. This process caused the output power to show rather strong fluctuations around the relaxation oscillation frequency. As countermeasure a power stabilization control loop called *noise eater* was integrated into the laser head. It consisted of a PIN photo diode monitoring the power of a small fraction of the output beam and a control circuit, which fed back on the current of the pump diodes. The relative intensity noise was suppressed by 30 dB.

Inside the laser head the beam passed a Faraday isolator and a beam splitter, which transmitted 350 mW of light power into the output and reflected the remaining 1.8 W

through an electro optical modulator (EOM) to the integrated frequency doubling unit. Basically, this is equivalent to what is described in Section 3.2, a crystal sitting in a cavity. However, it was operated in such a way that $\chi^{(2)}$ non-linear up-conversion or second-harmonic generation was the dominant process by feeding the strong infrared field through the partially reflecting mirror into the resonator. As the resonator length had to be controlled, the incident infrared beam passed a phase modulating EOM. A common modulation-demodulation technique based on the work of R. V. Pound, R. W. P. Drever and J. L. Hall [56, 57, 58] was used to generate an appropriate error signal, see Section B.1.2. From stock the modulation frequency was set to 12 MHz, which was well within the cavity line width of around 150 MHz. A photo diode behind the highly reflecting end of the cavity measured the residual transmitted power. The signal was sent to the control unit, where it was demodulated and filtered to be fed back onto the cavity length. However, the modulation had to be rather strong to gain a reasonable error signal because of the low modulation frequency. This led to a non-negligible modulation on the generated green field. Furthermore, the modulation frequency was within the frequency band of downstream measurements, which led to our decision to change the modulation frequency.

We chose a frequency of 200 MHz. This frequency was well outside the downstream experiment's detection band. Additionally, this was close to the frequency at which – given the line width – the demodulated signal was the biggest, see Section B.1.3. For equal modulation indices the signal for the 200 MHz modulation was ten times bigger than that for 12 MHz. In order to change the modulation frequency many amendments had to be made to this part of the laser. On the one hand, the EOM had to be replaced. More demanding, on the other hand, was the detection and demodulation stage. We replaced the photo detector with a custom made one to achieve a good performance at the higher frequency, and in the same step we moved the modulation-demodulation stage onto the detector circuit board (see Section A.2.5), which circumvented the transmission of any 200 MHz signal over a longer distance. The demodulated signal was conditioned in such a manner that it suited the existing control circuitry. In total, we could reduce the modulation depth by a factor of 30 and ended up with only 3 mrad of RMS phase fluctuations on the green field. Assisted by the increased modulation frequency the laser was now suitable for the experiments we had in mind.

In order to prepare a high quality (see Section 3.3) local oscillator the fundamental mode was sent through a high finesse mode cleaning cavity (MC) based on the design described in [59]. An efficient spatial mode and frequency filtering was provided by the MC, which was designed to have a line width $\Delta\nu$ of $\Delta\nu = 55$ kHz resulting from a finesse of $\mathcal{F} = 10500$ with a round trip length of $l = 52$ cm. On resonance it transmitted more than 95% of the incident light power. The control circuitry for keeping the fundamental laser on resonance with the mode cleaner followed the PDH scheme, see Section B.1.3. The acquisition of the error signal was straight forward, but the feedback path turned out not to be trivial. After careful investigation the feedback loop was split into two paths for different frequencies to benefit from the higher stability of various components at different frequencies. The low frequency part of up to 0.1 Hz was covered by feeding back to the temperature of the spacer of the mode cleaner and thus on

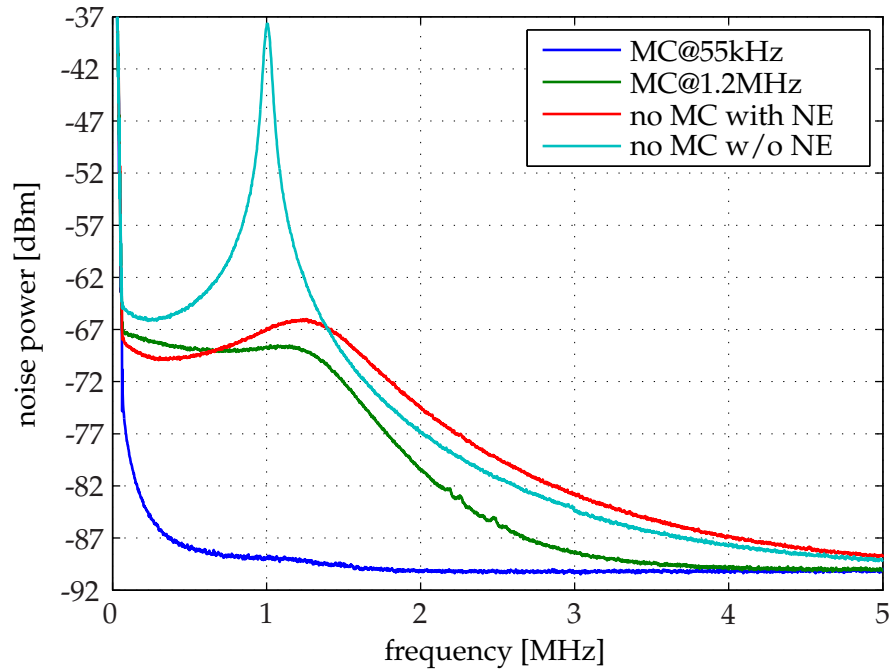


Figure 3.2 - Spectral noise power of the main fundamental laser. MC: mode cleaner. NE: noise eater. The beam power was 5 mW, the spectrum analyzer was set to a resolution band width of RBW=10 kHz and a video bandwidth of VBW=3 Hz. The red and the cyan curve show the spectra of the beam as emitted by the laser with the internal noise eater (see text) turned off (cyan) and on (red). For the blue and green curve the beam passed the mode cleaning cavity (MC), which was operated on the low finesse (green) and high finesse (blue) mode. The shot noise level for the given power is marked by the flat part of the blue curve, see Figure 3.13.

its optical path length. The high frequency part of up to 30 kHz was managed by actuating the laser frequency via the laser crystal PZT. The PZT could be driven directly by a standard operational amplifier omitting any high voltage (HV) components. A low dynamic range in the upper frequency range was fairly sufficient. In an earlier stage the high voltage amplifier caused severe problems; the output voltage was so noisy that a stable operation was impossible. However, the final layout displayed no extra noise in any part of the spectrum.

3.1.2 Auxiliary Laser

The auxiliary laser was a low power version of the infrared stage of the main laser. It was pumped by only one laser diode array and yielded up to 300 mW of output power. The means of adjusting the laser frequency are also right the same and were used to establish a phase-locked loop (PLL) with the fundamental laser. This enabled a phase readout scheme for downstream BHDs for arbitrary detection phases, which is mandatory for quantum state tomography, see Section A.1.

In general, a PLL consists of three components: a phase detector, a feedback path and

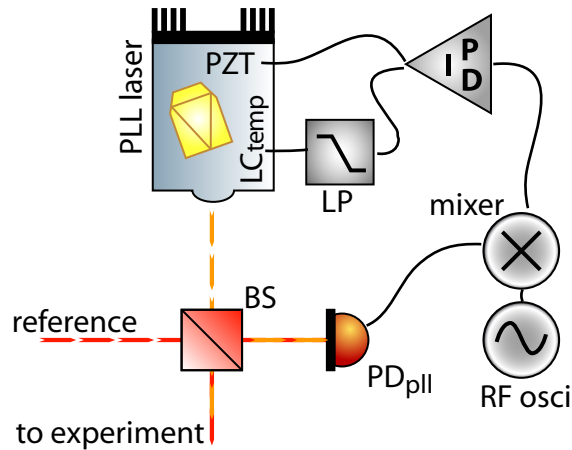


Figure 3.3 - Schematic of the PLL laser system. At the beam splitter (BS) the auxiliary laser (PLL laser) is superimposed with the fundamental (reference). The interference in one port of the BS was detected with a photo diode. Its signal was mixed (mixer) with a radio frequency signal (RF_{osci}), which generates the input for the loop controller (PID). The loop is closed by changing the PLL laser frequency according to the PID signal in two ways: slowly via the temperature of the laser crystal (LC_{temp}) with an additional integrator (LP), and fast via the PZT attached to the laser crystal. With the feedback loop closed, the PLL laser field had a fixed phase with respect to the reference field and a frequency offset determined by RF_{osci} .

a variable oscillator (see Figure 3.3). The latter is the beat note, i.e. the difference of the frequencies of fundamental and auxiliary laser detected with a photo diode. This could simply be done by sending both beams onto a detector and relying on e.g. detector inhomogeneities prohibiting perfect cancellation of the interference fringes. However, the signal gets stronger the higher the interference contrast is. Hence, a beam splitter was used to superimpose the two fields with a reasonable spatial mode-matching yielding a contrast of more than 85%. We chose the difference of the frequencies to be 50 MHz, as this was easy to detect but yet outside the main experiment's detection band.

The phase detector was a double balanced mixer generating the sum and the difference of the frequencies of the beat note signal and a 50 Mhz reference oscillator, see Section A.1.2. A low pass filter suppressed the sum frequency. For equal input frequencies the output signal is proportional to the cosine of the mutual phase and thus was suitable as an error signal at a phase difference of 90 degrees. This error signal was sent to a feedback controller, which actuated the auxiliary laser frequency in two ways: A fast path drove the PZT on the laser crystal, while a slow path varied the crystal temperature. Regarding the stability of the loop there were several issues to keep in mind. The error signal was proportional to the phase while the feedback was applied to the frequency, which is the derivative of the phase for harmonic signals. Thus, in frequency space there was an intrinsic frequency characteristic of $1/f$, which is usually sufficient for a stable control loop. Still there was an additional integrator needed in the controller because otherwise a frequency drift of the fundamental laser could not be compensated without leaving the linear regime of the sinusoidal phase dependence of the error signal. Yet, another integrator was needed in the slow path of the feedback

to ensure the stability of the split feedback system. The details can be found in Section A.1.1. In total, the PLL worked with sufficient stability for hours.

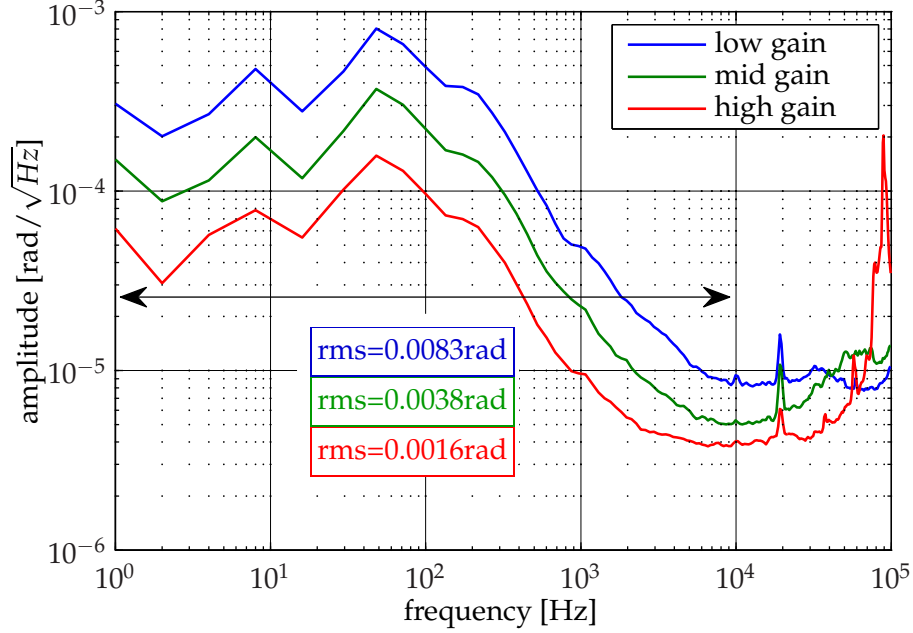


Figure 3.4 - Linear spectral density of the mutual phase of fundamental and auxiliary laser with closed feedback loop. The stability in the relevant frequency band up to 10 kHz for the phase lock of the homodyne detectors was clearly overcoming the requirement of 0.01 rad. The three curves correspond to different loop gains. For the high gain setting a noise amplification due to a lack of phase margin of the loop frequency response could be observed around 90 kHz. This was irrelevant for the downstream homodyne detector phase control, which was designed with a band width of around 1 kHz. Hence, the noise suppression in the lower frequency regime was still beneficial.

3.2 Non-classical Light Sources / Squeezer

The sources preparing the squeezed states throughout this work were constituted of optical parametric amplifiers (OPAs), which utilized the second order term $\chi^{(2)}$ of the non-linear electrical polarization inside a special medium caused by an incident light field. This non-linearity made different frequency components of the light field interact, e.g. the NIR fundamental and the green second-harmonic fields in the presented context. In general, for an OPA there is a strongly dominant *pump* field at a certain frequency ω_p interacting with two other fields called *signal* at the frequency ω_s and *idler* at ω_i . Energy conservation necessitates $\omega_p = \omega_s + \omega_i$. For plane waves, see [60], the conservation of momentum requires $\vec{k}_p = \vec{k}_s + \vec{k}_i$ for the wave vectors k in the medium, which is called *phase-matching*. Here, this special medium was formed by magnesium oxide doped lithium niobate (MgO : LiNbO₃) crystals. We had the crystals cut and polished such that they could be used for a type-I non-critically phase-matched

degenerate OPA. In more detail this means, that the two subharmonic fields, signal and idler, shared the same polarization, which was perpendicular to that of the pump field (type-I). The phase-matching was achieved by tuning the temperature of the non-linear medium in this way, that the refractive indices for the pump field in the ordinary polarization and of the subharmonic fields in the extraordinary polarization matched exactly. This kind of phase-matching is non critical regarding the alignment, because all beams can propagate on the same axis. The frequencies of the subharmonic fields are degenerate to very close (\approx RF) to half of the pump field frequency, which is termed *fundamental frequency*.

The non-linear crystal was surrounded by an optical cavity to increase the effective non-linear interaction as shown in Figure 3.5.

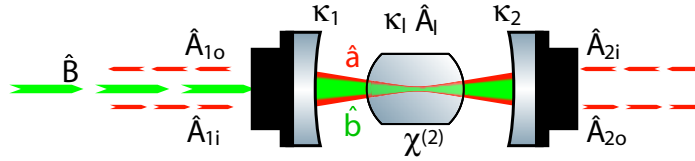


Figure 3.5 - A non-linear crystal $\chi^{(2)}$ in a cavity. The cavity mode annihilation operators are termed \hat{a} for the fundamental and \hat{b} for the pump mode. \hat{A} and \hat{B} are annihilation operators for propagating fields entering or emerging the cavity. The coupling constants determined by the mirror reflectivities are denoted κ . \hat{X}_1 and κ_1 refer to generic loss inside the cavity due to absorption, scattering, diffraction or refraction.

The following brief discussion of the maths of such a device is based on the quantum Langevin equations for damped quantum systems derived in [61] and the quantum interaction of fundamental and harmonic field in [24]. A cavity mode can be treated with the quantum harmonic oscillator formalism of annihilation \hat{a} and creation \hat{a}^\dagger operators. The number of photons $\langle n \rangle$ in the fundamental mode is given by $\langle \hat{n} \rangle = \langle \hat{a}^\dagger \hat{a} \rangle$. Propagating modes can be similarly represented by \hat{A} and \hat{A}^\dagger . The difference is, that the expectation value $\langle \hat{A}^\dagger \hat{A} \rangle$ is a photon flux, i.e. the number of photons per time interval. We assume, that the cavity is tuned to the laser frequency ω . Thus, the frequency of the eigenmode of the cavity addressed by \hat{a} is the same as for the propagating modes (\hat{A}). The Hamiltonian \hat{H}_{II} for a lossless OPA is given by:

$$\hat{H}_{II} = \underbrace{\hbar\omega\hat{a}^\dagger\hat{a}}_{\text{fundamental}} + \underbrace{\hbar2\omega\hat{b}^\dagger\hat{b}}_{\text{pump}} + \underbrace{i\hbar\zeta/2(\hat{a}^{+2}\hat{b} - \hat{a}^2\hat{b}^\dagger)}_{\text{interaction}}, \quad (3.1)$$

with all details of the non-linear interaction, such as the corresponding component of $\chi^{(2)}$, the beam diameter in the medium and the phase-matching are packed into the coefficient ζ . The time evolution of \hat{a} can be derived from $\dot{\hat{a}} = [\hat{a}, \hat{H}_{II}]/i\hbar$ and the damping part from the Langevin equations:

$$\dot{\hat{a}} = -\kappa\hat{a} + \zeta\hat{a}^\dagger\hat{b} + \sqrt{2\kappa_1}\hat{X}_{1i} + \sqrt{2\kappa_2}\hat{X}_{2i} + \sqrt{2\kappa_1}\hat{X}_1. \quad (3.2)$$

The total cavity damping rate κ is given by $\kappa = \kappa_1 + \kappa_2 + \kappa_1$. Since the pump power

is assumed to be strong we can further assume, that the pump is not depleted by the OPA process. Hence, we can treat it as a classical coherent field by replacing \hat{b} with its temporally stationary expectation value β . The combination $g = \zeta\beta$ will be assumed to be real (determined by the phase of β). We reformulate the above equation (and its Hermitean conjugate) in terms of the quadrature operators \hat{q}^+ for the amplitude and \hat{q}^- for the phase (for convenience, instead of \hat{p}):

$$\begin{aligned}\hat{q}_a^+ &= (g - \kappa)\hat{q}_a^+ + \sqrt{2\kappa_1}\hat{q}_{1i}^+ + \sqrt{2\kappa_2}\hat{q}_{2i}^+ + \sqrt{2\kappa_1}\hat{q}_1^+, \\ \hat{q}_a^- &= -(g + \kappa)\hat{q}_a^- + \sqrt{2\kappa_1}\hat{q}_{1i}^- + \sqrt{2\kappa_2}\hat{q}_{2i}^- + \sqrt{2\kappa_1}\hat{q}_1^-. \end{aligned} \quad (3.3)$$

The solution for \hat{q}_a^\pm can be found via a Fourier transform. In the rotating frame of frequency ω the solution reads:

$$\hat{q}^\pm = \frac{1}{\kappa \mp g} \left(\sqrt{2\kappa_1}\hat{q}_{1i}^\pm + \sqrt{2\kappa_2}\hat{q}_{2i}^\pm + \sqrt{2\kappa_1}\hat{q}_1^\pm \right). \quad (3.4)$$

For a certain pump power level P_{thr} the absolute value of g equals κ , which displays the threshold to spontaneous optical parametric oscillation (OPO) at the fundamental frequency. This is similar to a laser, which starts lasing once the population inversion in the active medium is strong enough to yield a gain factor exceeding the laser cavity loss.

To calculate the fields \hat{X}_{no} (\hat{q}_{no}^\pm respectively) we use the input-output-relations $\hat{X}_{\text{no}} = \sqrt{2\kappa_n}\hat{a} - \hat{X}_{\text{ni}}$ [61] and find e.g. for the left one in Figure 3.5:

$$\hat{q}_{1o}^\pm = \frac{1}{\kappa \mp g} \left[(2\kappa_1 - \kappa \pm g)\hat{q}_{1i}^\pm + \sqrt{4\kappa_1\kappa_2}\hat{q}_{2i}^\pm + \sqrt{4\kappa_1\kappa_1}\hat{q}_1^\pm \right]. \quad (3.5)$$

Assuming all input fields are coherent, we replace their variances by $V_{\text{ni},l}^\pm = \langle \langle \hat{q}_{\text{ni},l}^{\pm 2} \rangle \rangle - \langle \hat{q}_{\text{ni},l}^\pm \rangle^2 = 1/4$. The output quadrature variances then read:

$$V_{1o}^\pm = \frac{1}{(\kappa \mp g)^2} \left[\frac{1}{4}(2\kappa_1 - \kappa \pm g)^2 + \kappa_1\kappa_2 + \kappa_1\kappa_l \right]. \quad (3.6)$$

For the left coupling mirror being a perfect mirror, $\kappa_1 = 0$ we find the expected $V_{1o}^\pm = 1/4$. For perfect squeezing, e.g. in the amplitude quadrature $V_{1o}^+ = 0$, each individual term in the square brackets has to vanish as they are all semi-positive. Thus, there must be neither any loss $\kappa_1 = 0$ nor any coupling on the right $\kappa_2 = 0$. Also the gain has to match the coupling on the left hand side $|g| = \kappa_1$.

For an actual implementation this means that for a good squeezer the losses have to be kept low and the cavity has to be single-ended. The design of our OPAs was the result of quite a few iteration steps, which successively led to its current mature state.

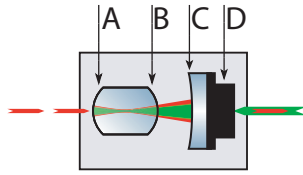


Figure 3.6 - Pictograph of the OPA. The facette A is a high reflectivity ($> 99.95\%$) mirror for the fundamental and harmonic wavelength coated directly onto the non-linear crystal. The opposing surface B carried an anti-reflection coating for both wavelengths. An optical resonator is formed between A and C, which is the coated surface of a movable mirror. The reflectivities of the latter are carefully chosen to provide the target line width for the fundamental and the power build-up for the pump field. The movable mirror is actuated by a PZT D.

3.2.1 Optical and Mechanical Layout

In general, the cavity surrounding the crystal can come in various configurations regarding the geometry and the cavity parameters for the fundamental and the pump field. The idea of using a *semi-monolithic* cavity for an OPA has long since existed [62, 63, 64]. Here, a satisfying balance between tunability and stability was achieved by coating the high reflectivity mirror directly onto the non-linear medium itself (Figure 3.6 A). The partially reflecting coupling mirror (Figure 3.6 C) was movable by means of a piezo-electric transducer (PZT, Figure 3.6 D). This saved one movable and thus unintentionally moving mirror as well as an inevitably lossy intra-cavity anti-reflex (AR) coating, leaving only a single movable one (Figure 3.6 B) remaining. Also the length of such a cavity could be kept short, which limited the amount of air inside the resonator and resulted in a high line width with given mirror reflectivities. A truly monolithic design with both cavity mirrors coated onto the crystal would even increase these beneficial factors. However, that would have made it hard to simultaneously tune more than one OPA on resonance with the laser, because the length of a monolithic cavity cannot be tuned easily to resonate with the laser.

The cavity geometry determined the shape of the cavity eigenmode. On the one hand, a small beam waist radius w_0 enhanced the effective non-linearity due to the higher intensities. On the other hand, the strong divergence of such a beam would make mode-matching hard and could even lead to thermal lensing induced by the inevitable absorption of the strong pump beam. The closest feasible position for a mode-matching lens was roughly $z_{\min} = 10$ cm away from the waist. In order to stay on the safe side the beam radius $w(z_{\min})$ at this position should not be larger than one millimetre to avoid diffraction or aberration for a standard 25 millimetre lens: $w(z_{\min}) < w_{\max} = 1$ mm. The divergence angle ϵ well outside the Rayleigh range for a beam of the wavelength λ and waist size w_0 is given by $\epsilon = \lambda / (\pi w_0)$. This led to the approximation $w(z) = \epsilon z$. Consequently, the waist size is limited from below: $w_0 > z\lambda / (\pi w_{\max}) \approx 30 \mu\text{m}$. In order to relax this constraint we had the substrate of the coupling mirror polished with a meniscus shape as sketched in Figure 3.7 to act as an additional lens. Thus, we could design the cavity to have a waist of $25 \mu\text{m}$ centred in the crystal, while the beam emerging the cavity corresponded to a waist of $42 \mu\text{m}$

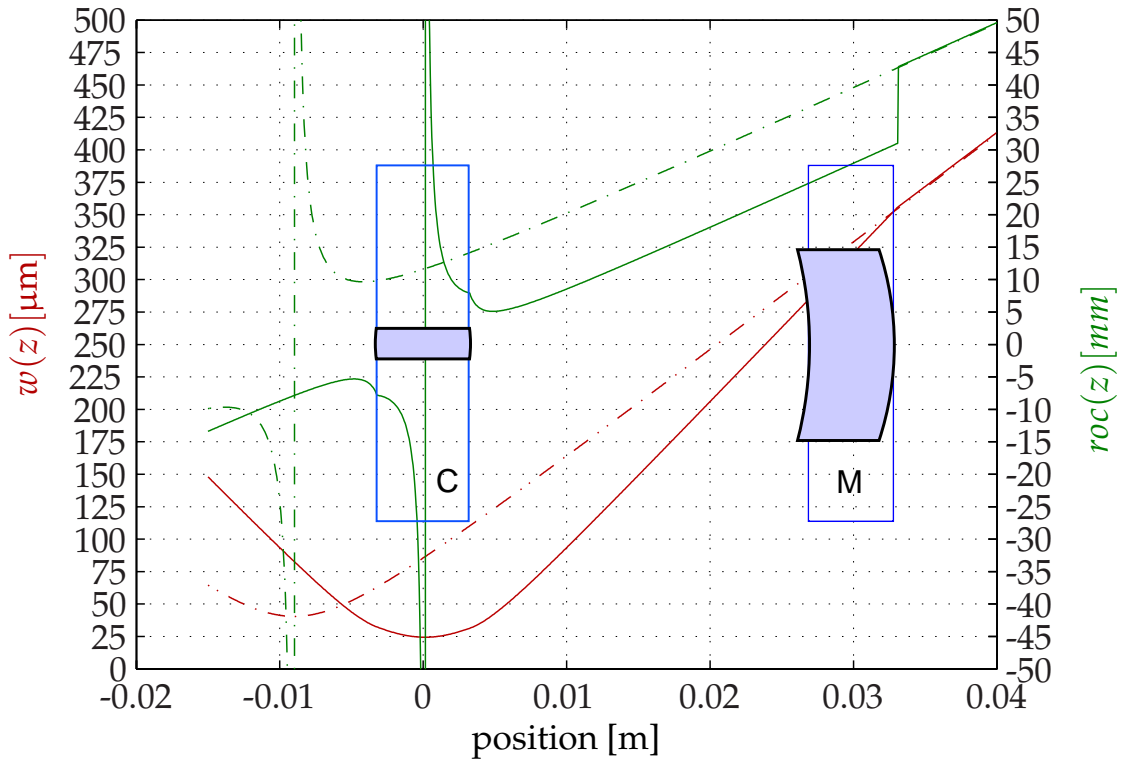


Figure 3.7 - Beam parameters for the OPA cavity geometry. The crystal C had a radius of curvature of 8 mm on both optical faces. In combination with the coupling mirror M curvature of 25 mm at the given position this formed a cavity mode with a waist size of 25 μm in the middle of the crystal (solid lines). The meniscus shape of the coupling mirror on the right side formed an additional lens, which changed the beam parameters of the mode emerging to the right. For a radius of curvature of 20 mm a larger apparent waist size of 42 μm was obtained.

located only a few millimetres behind the crystal.

For a reasonable choice of the coupling constant κ_1 several considerations had to be taken into account. As stated below Equation 3.6, the total cavity loss rate had to be dominated by the coupling mirror κ_1 . A decent high reflectivity mirror as coated on the crystal surface provided a power reflectivity of 99.95%. The absorption in the crystal was measured to be lower than 10^{-3}cm^{-1} , and the AR coating transmitted more than 99.8% of the power. These three contributions summed up to 0.3% loss per round trip. For the cavity dynamics to be dominated by the coupler its transmissivity should be at least ten times larger, i.e. the reflectivity should be less than 97%.

A second need for a large κ_1 arose from the cavity line width, which depended on κ_1 (see Section B.5) and directly mapped onto the squeezing spectrum, see Figure 3.8. As mentioned in Section 3.1.1 the laser was not shot noise limited at low modulation frequencies, and thus the squeezing spectrum had to be wide enough to cover some of the shot noise limited, higher frequency part of the spectrum above 5 MHz. As shown in Figure 3.8 it was necessary to have a cavity line width of the order of 40 MHz to have

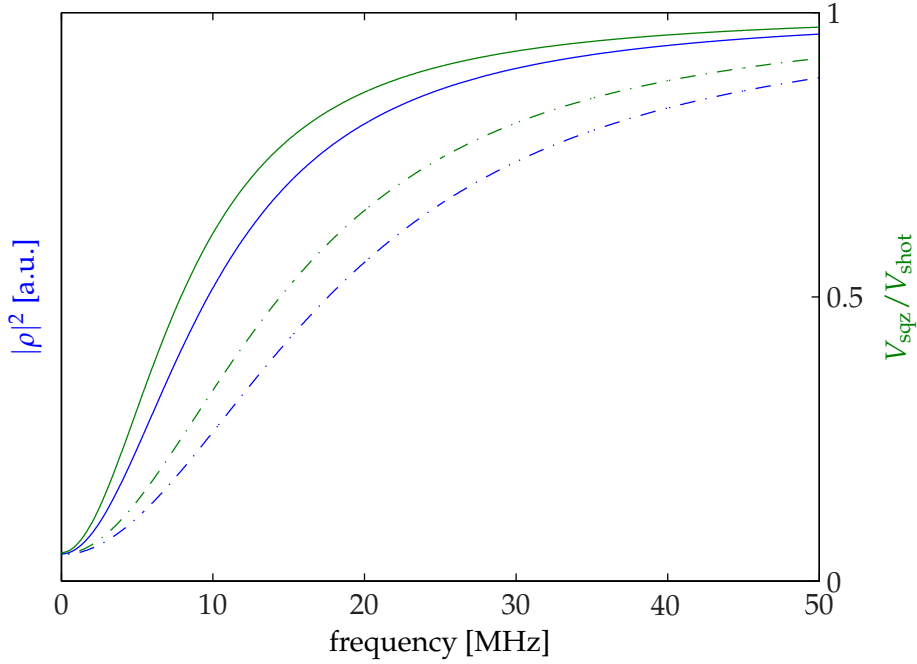


Figure 3.8 - OPA: relative power (blue) reflected from the OPA cavity and spectra of the relative variance of the squeezed quadrature versus the frequency difference to the resonance. The OPA cavity line width is 20 MHz for the solid lines and 37 MHz for the dashed ones. The single pass round trip gain, i.e. the pump power, is adjusted to yield the same level of squeezing at zero frequency. $|\rho|^2$ is scaled to level with the variances at zero frequency. The band width of good squeezing is significantly smaller than the cavity line width.

a decent amount of squeezing up to 10 MHz. Given the geometry of Figure 3.7 with a free spectral range of 4 GHz the power reflectivity r_c of the coupling mirror had to be $r_c \approx 94\%$, which yields a finesse of $\mathcal{F} \approx 100$. On the other hand a large value of κ_1 implied that a large pump power would be required to get close to the threshold, which was limited for several reasons. The most obvious limit was the power limit set by the main laser source, which may be overcome by setting up a cavity for the pump laser around the crystal as well. Another set of limits arose from various non-linear properties of the crystal material, such as non-linear absorption [65], photorefractive damage [66] and green induced infrared absorption (GRIIRA) [67].

For the OPAs used for this work we decided to make the coupler coating in that manner, that it provided a reflectivity of 25% for the pump light, too. This yielded a finesse F_p for the pump field of as low as $F_p = 4.3$ and a power build-up factor of three. The reason was that it was planned to have three OPAs pumped by the main laser source, which could otherwise have led to a lack of pump power. However, such a configuration necessitated that the resonances for fundamental and pump radiation coincide. Although the crystal temperature was controlled to match the refractive indices for the two wavelengths, there were three coatings (A,B,C in Figure 3.6), which had to be designed in such a way, that there is no phase difference for infrared and green light. For

this reason we chose the moderate finesse for the green, which resulted in a high line width providing a power build-up larger than one for one third of a free spectral range. It turned out that the coating company was able to precisely meet our requirements and we could benefit from the maximum power build-up factor of three.

Increasing the magnesium oxide doping from 5% [68] to 7% resulted in a decent phase-matching temperature of $\approx 60^\circ\text{C}$. Compared to the *old* crystals with 5% doping and a phase-matching temperature of over 100°C , this was comfortably achieved with small Peltier elements and rendered the formally required slow heating resistors obsolete.

Two major improvements arose from the present work, see Figure 3.9. The new closed and compact housing of the OPA drastically improved the overall stability and robustness. The slight resonance enhancement of the pump field decreased the necessary input power significantly. Additionally it provided a spatial mode cleaning.

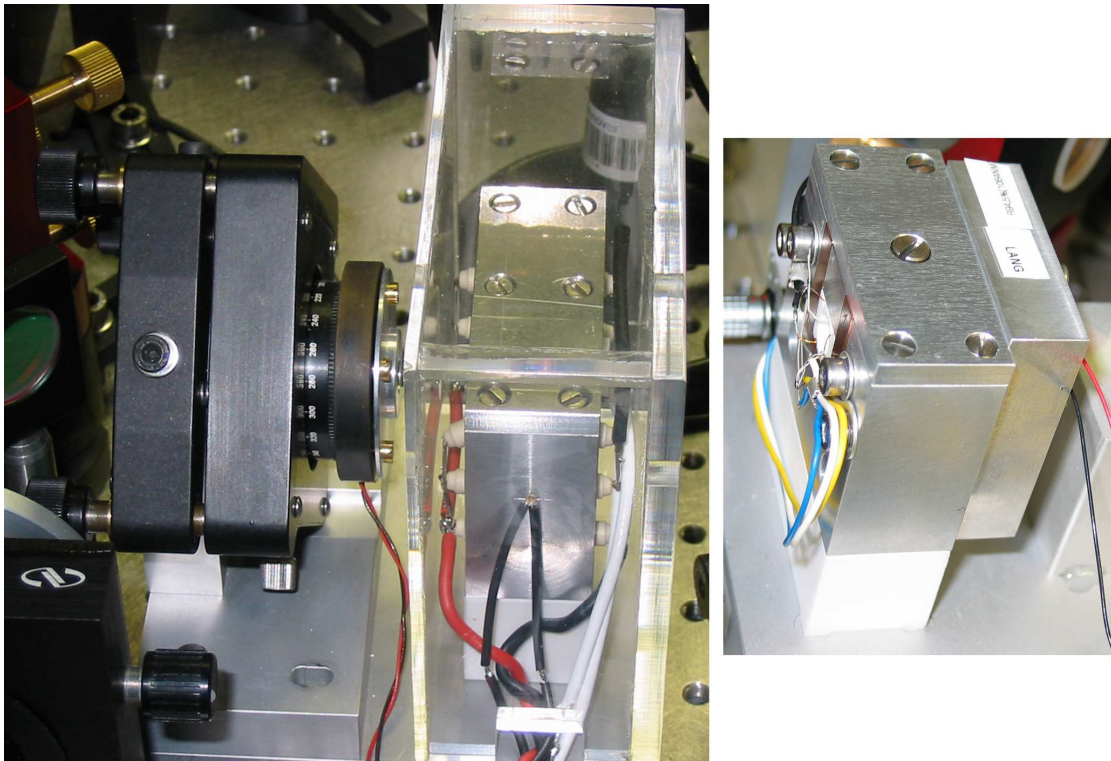


Figure 3.9 - Comparison of the old (left) and new (right) designs of the OPAs. The crystals were housed in the aluminium blocks with the screws on top in both cases. In the old design the whole aluminium housing had to be heated to about 100°C by means of a set of heating resistors. The coupling mirror was carried by the bulky black mirror mount resulting in an unhoused air gap inside the cavity. The relaxed phase-matching temperature of about 60°C of the new crystals could be achieved by Peltier elements sitting inside the aluminium housing very close to the crystal. In the new design the coupling mirror sat inside an extra aluminium block attached directly to the crystal housing (right) and the cavity was completely shielded from the environment.

Usually, the classical (de-)amplification g_{ca} of the power of the fundamental control field is measured. Here we calculate, how that relates to the squeezing that can be expected at zero modulation frequency. From Equation 3.2 and Equation 3.5 we can derive the classical field emerging from the OPA by substituting all \hat{a} and their adjoint by their expectation values $\alpha = \langle \hat{a} \rangle$. Assuming that only $\langle \hat{A}_{2i} \rangle$ and $\langle \hat{B} \rangle$ have a real classical amplitude, we find for $\langle \hat{A}_{1o} \rangle$:

$$\langle \hat{A}_{1o} \rangle = 2\sqrt{\kappa_1\kappa_2} \frac{\kappa + g}{\kappa^2 - |g|^2} \langle \hat{A}_{2i} \rangle. \quad (3.7)$$

The square value of Equation 3.7 yields the power P_{1o} :

$$g_{ca} = \frac{P_{1o}}{P_{1o}|_{g=0}} = \frac{(\kappa + g)^2}{(\kappa^2 - |g|^2)^2}. \quad (3.8)$$

This equation can now be solved for g and plugged into the formula for the output variances, see Equation 3.6:

$$\begin{aligned} V_{1o}^+ &= \frac{1}{4} - \frac{(\sqrt{g_{ca}} - g_{ca})\kappa_1}{\kappa}, \\ V_{1o}^- &= \frac{1}{4} + \frac{(\sqrt{g_{ca}} - g_{ca})\kappa_1}{(1 - 2\sqrt{g_{ca}})^2\kappa}. \end{aligned} \quad (3.9)$$

With reasonably reliable values for κ and κ_1 it is possible to infer the squeezing variances at zero frequency, see Figure 3.10.

3.2.2 Stabilization

There are three control loops discussed in this section. Two of which were necessary for the OPA itself to prepare a squeezed state. These were the microscopic length control of the OPA cavity and the temperature control of the non-linear crystal to meet and preserve the phase-matching condition. The third was mandatory to be able to handle the squeezed state in downstream experiments in a deterministic way. In general, the orientation of the squeezing ellipse maps the phase of the pump field and thus has to be controlled. For this purpose the phase of the pump field was locked to the phase of the fundamental field which was used to control the length of the cavity and hence copropagating with the squeezed field.

In case of the crystal temperature there was a standard temperature stabilization scheme. A resistor with a large negative temperature coefficient (NTC) was put in thermal contact with the crystal. The resistance was measured by an active Wien bridge, see Section B.1.1, which provided a voltage X_{es} proportional to (small) deviations of the resistance of the NTC from that of a reference resistor. This voltage was amplified, appropriately filtered and converted into a proportional current. This current was sent through the Peltier elements attached to the crystal. Chosen the right polarity there was

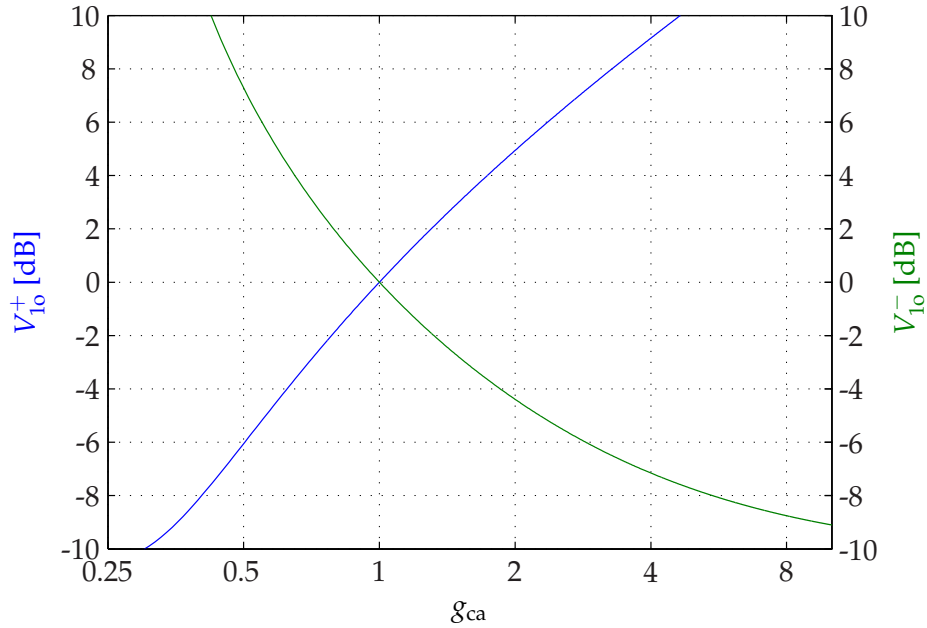


Figure 3.10 - Squeezing variances V_{10}^{\pm} versus the classical (de-)amplification g_{ca} . This example is based on realistic parameters for the coupler reflectivity (95%) and the extra cavity loss (0.3%). Note that a perfect detection is assumed.

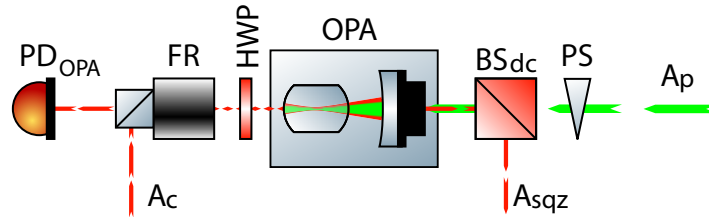


Figure 3.11 - Control scheme around the OPA. E_c : fundamental control field. E_p : second-harmonic pump field. E_{sqz} : beam carrying control fields and squeezing. FR: Faraday rotator. HWP: half wave plate. BS_{dc} : dichroic beam splitter. PS: phase shifter. PD: photo detector.

negative feedback: The crystal is too warm/cold \Rightarrow the NTC had a lower/higher resistance than the comparison resistor $\Rightarrow X_{es}$ is positive/negative \Rightarrow the current through the Peltier elements cooled/heated the crystal. With an appropriate filtering such a loop is stable.

For the optical control scheme, see Figure 3.11, we came up with a ‘two birds with one stone’ strategy, which was to control both the cavity length and the pump phase with a single modulation on the infrared field. A chain of reasoning led to the conclusion that the pump phase was best set such, that the fundamental control field was deamplified which corresponds to amplitude squeezing with respect to the control field. The deamplification was beneficial because the spectral noise power of the fundamental field was well above the shot noise level at low modulation mode frequencies f and

rolled off with $1/f^2$. The squeezed field generated by the OPA was necessarily superimposed with the control field. This means, that the noise on the control field would cover the squeezing. In order to work at the shot noise level at a reasonably low frequency, it was therefore necessary to have as little fundamental light on the squeezed mode as possible. On the other hand, the control beam for the OPA cavity length should be as strong as possible to achieve a good signal to noise ratio for the control signal. However, this was exactly what put fundamental light on the squeezed field. Thus, tuning the pump phase for parametric deamplification was beneficial, as it deamplified the control field emerging from the OPA together with the squeezed field. For a maximum deamplification the light power is obviously extremal with respect to the mutual optical phase of the control field and the pump. In order to derive an error signal for this phase it was thus necessary to modulate the phase and demodulate the detected power, as described in Section B.1.2. The phase modulation could be applied either to the pump or to the control field. The former was done in earlier experiments [68]. However, a modulation of the pump phase also modulated the orientation of the squeezing ellipse. Thus, it was preferable to use a phase modulation of the control field. In such a situation the error signal was obtained by demodulation in phase with the modulation signal, see Section B.1.2.

At the same time the optical OPA cavity length was controlled with a scheme described in Section B.1.3. In this scheme the proper demodulation phase depended on the relation of the modulation frequency Ω_m and the cavity line width Δ_ν . For $\Omega_m \gg \Delta_\nu$ the demodulation had to be in phase and for $\Omega_m \ll \Delta_\nu$ it had to be out of phase. Choosing $\Omega_m \ll \Delta_\nu$ this property allowed us to derive independent error signals for the pump phase and the cavity by the demodulation in / out of phase of only a single phase modulation on the control field.

3.3 Balanced Homodyne Detector

In order to observe quantum quadrature fluctuations we needed a suitable balanced homodyne detector. We required a high quantum efficiency $\eta = I/(e_c n)$ with I for the photo current, e_c for the electron charge and n for the incident photon flux. For our wavelength of 1064 nm the semiconductor material InGaAs (indium-gallium-arsenide) provides a suitable band gap. We chose the photo diode ETX-500 by Epitaxx with a radius of the active area of 500 μm . These devices provided an quantum efficiency of $\eta \geq 93\%$.

The individual photo diodes were run in self made amplifier circuits based on common transimpedance amplification, i.e. the photo current is converted into a voltage. For the calculations of Section 2.3.1 to be valid the amplified signal must be proportional to the photon flux. We checked this property by comparing the output voltage of the individual detectors with the incident optical power detected with a power meter for various values for the power. The dependence was found to be linear within 2%. The linearity also had to be provided for the spectral components of the signal. We checked that by recording power spectra of the detector signal for various power

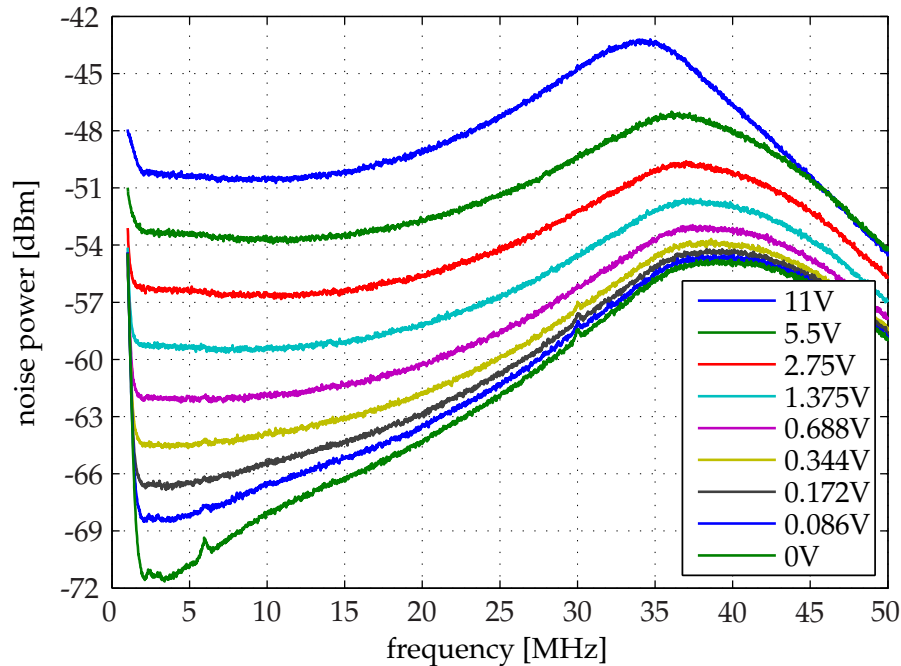


Figure 3.12 - Spectra of the fundamental laser at different power levels detected with a single photo detector. The parameters of the spectrum analyzer were $\text{RBW}=300\text{ kHz}$ and $\text{VBW}=30\text{ Hz}$. For the actual choice of the electronic parameters the voltage given in the legend roughly scales with 1 mW/V for the incident light power, see Section A.2.1. The shape of the curves mapped the detector transfer function because the spectrum of the incident light power was white shot noise, see Figure 3.13. For the highest light power a slight change of the transfer function can be observed due to the onset of saturation of the detector electronics.

levels, see Figure 3.12. For this purpose the laser was filtered by a mode cleaner with a line width of 55 kHz to ensure that we see the shot noise in the spectra, which scales linear with the optical power. In the low power regime the signal was dominated by the electronic dark noise of the detector. Given that the detector dark noise is uncorrelated to the measured shot noise, we could subtract the dark noise level from the other traces and obtained the results shown in Figure 3.13. We found an excellent linearity, as for every factor of two in the optical power the spectra shifted by 3 dB in the relevant power regime.

Given suitable individual detectors, we needed to confirm that the BHD consisting of two photo detectors and an electronic subtractor, see Section A.7, was well-behaved, too. We could confirm the linearity with the same procedure as above. Furthermore, for the quantum state measurements the total electronic dark noise of the whole BHD was required to be much smaller than the signal from the quadrature measurement. For a comparison we chose the shot noise level corresponding to the nominal optical operating power, as shown in Figure 3.14. The dark noise power level was found to be up to 20 dB , i.e. a factor of 100, smaller than the shot noise level. Thus, we considered the dark noise clearance large enough.

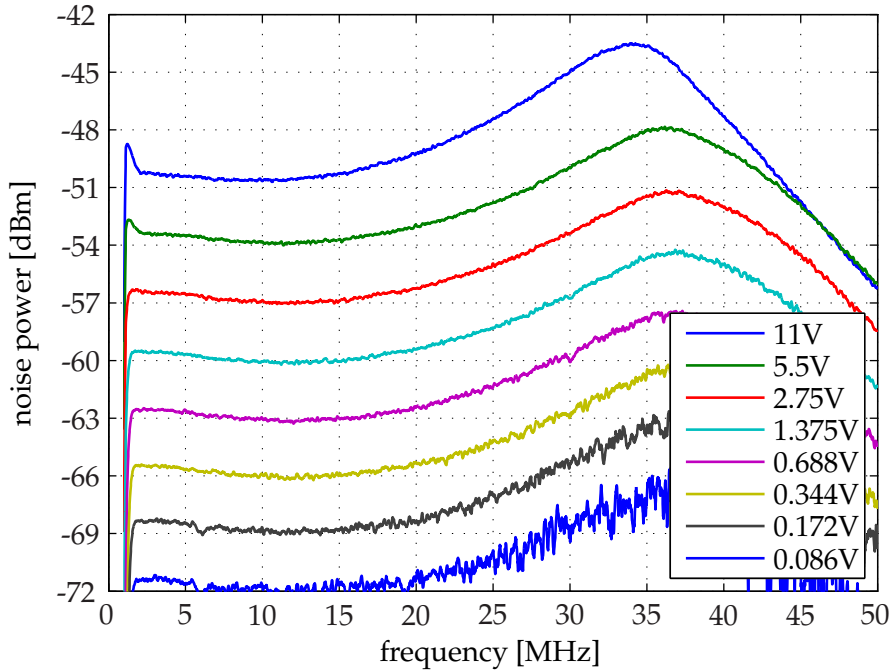


Figure 3.13 - Spectra of the previous (Figure 3.12) corrected for the electronic detector dark noise. For each factor of two of the incident light power (the voltage given in the legend) the spectral power level increases by 3 dB. The detector is linear for two orders of magnitude.

3.4 Quantum State Tomograph

As described in Section 2.3.2 quantum state tomography is based on quadrature measurements with a BHD, for a certain set of well defined detection phases and the sampling of the corresponding probability distributions.

For the quantum state tomography of a single mode quantum state of the kind which we prepared in our experiments, it was usually sufficient to address roughly ten equidistant angles covering half a revolution in phase space. Given enough patience and/or a rock steady experimental setup this could be done by manually setting the desired phase, recording data, setting the next phase and so on. However, in case of the quantum state tomography of a two mode state, e.g. an entangled state, as it was subject of this thesis there were two homodyne detectors. To end up with the same resolution as in the single mode case, every combination of the ten phases per detector had to be measured, totalling in one hundred sequences of setting a phase and recording data. Even a fast experimentalist would probably spend more than a minute for a single setting, and thus would need one and a half hour for a whole tomography. Given a finite lifetime of the experiment and the desire to perform multiple measurements, it was a good idea to implement an automatic tomography machine.

Based on the techniques described in Section 3.5 and Section A.1 a PC based LabView environment was set up to perform this task. There was one PC dedicated to the

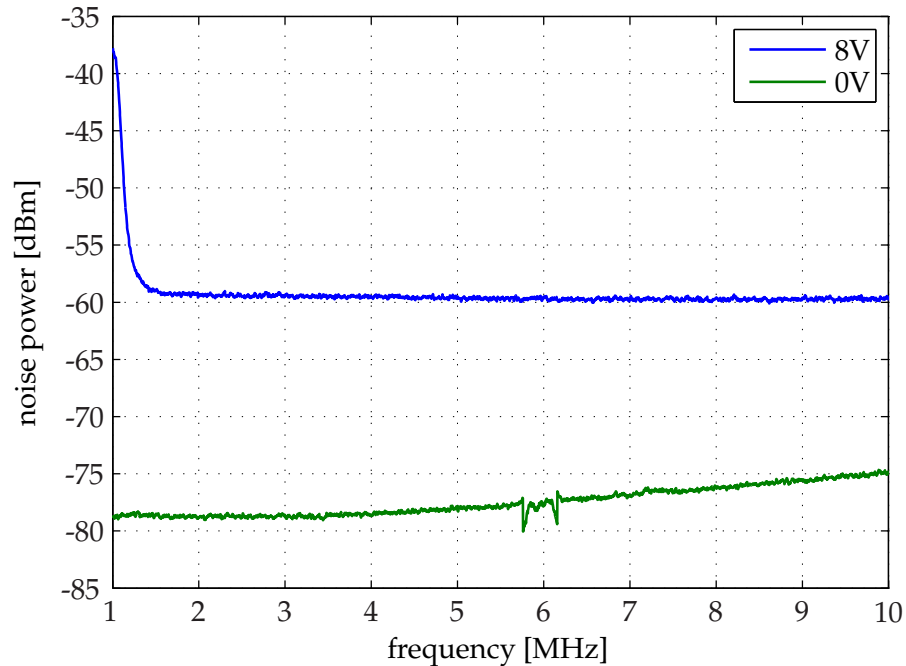


Figure 3.14 - Spectra of the difference signal of the BHD. With both optical inputs blocked we saw the electronic dark noise of the BHD (green). With the local oscillator port opened we obtained the blue curve corresponding to the noise level of the vacuum. The power of the local oscillator was set to the value of nominal operation. The clearance to the dark noise is almost 20 dB in the part of the spectrum relevant for this thesis.

data acquisition (DAQ) because it is crucial that the data are recorded exactly when they are supposed to. Hence, it must be ensured that the machine is not busy with any other task at that moment. A second PC (AUX-PC) was set up to take care of the tomography phase control, which is described in Section A.1 and Section A.1.2. For a successful tomography the data acquisition has to take place *after* the phases are set, and the next phase setting has to take place *after* the data acquisition is complete. A TCP interface between the two PCs was used to establish a communication link between them. The master control program ran on the first PC. The tomography procedure worked as follows:

- initialize the DAQ-PC
- initialize the AUX-PC
- start master program on DAQ-PC
- *DAQ loop start*
- TCP command from DAQ-PC to AUX-PC to set certain detection phases
- DAQ-PC waits for the phase setting to be finished

- DAQ-PC records data
- DAQ loop end

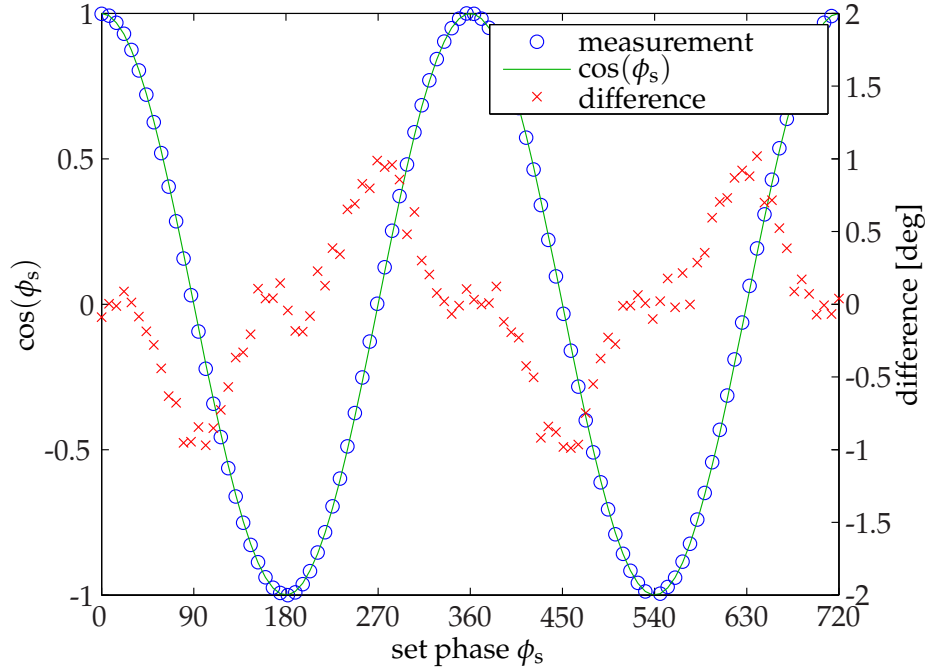


Figure 3.15 - Estimate of the accuracy of the BHD phase control. The control program scanned the phase interval $\phi_s \in [0 \dots 4\pi]$ with 100 steps. The blue circles represent the normalized measurement of the BHD DC signal for each step, which was proportional to $\cos(\phi_a)$ with the actual phase ϕ_a . For comparison, we plotted $\cos(\phi_s)$ (green line). The red crosses represent the difference of the two. The scaling was such, that at the zero crossings the values represent the phase deviation in degree (right axis). The absolute deviation was not bigger than 1° .

In order to check how well the detection phase could be set, we set the control program to scan the phase interval $\phi_s \in [0 \dots 2\pi]$ with 100 steps. For each step we recorded the DC BHD signal X_{DC} . This is proportional to $\cos \phi_a$, with ϕ_a being the actual phase on the BHD beam splitter for the interference of the local oscillator with the fundamental laser component on the signal. With X_{DC} normalized to unity amplitude, we calculated the difference $X_{DC} - \cos \phi_s = \cos \phi_a - \cos \phi_s$. For the zero crossings this quantity represents the difference of the intended phase ϕ_s and the actual phase ϕ_a . The results are shown in Figure 3.15. We found the absolute difference to be not bigger than 1° , and thus more than ten times smaller than the minimal phase interval we used for tomography.

3.5 Data Acquisition

In Section 2.3.1 it is shown, that a BHD provides the ability to measure field quadratures of a quantum light mode. Within the scope of this thesis there are up to six correlated

BHD signals. However, the correlation only exists between measurements at the same time. Therefore, the signals need to be recorded synchronously. Furthermore, lots of measurements have to be collected to obtain significant statistical distributions of the individual signals as well as their correlation. A numeric processing of the collected data is needed to extract meaningful quantities from the signals. The most convenient and flexible way is to digitize the individual signals and store the data on a computer hard disk. Once stored the data can be processed by the computer with virtually arbitrary algorithms, such as of course distillation and purification as well as the quantification of squeezing, entanglement or purity via quantum state tomography.

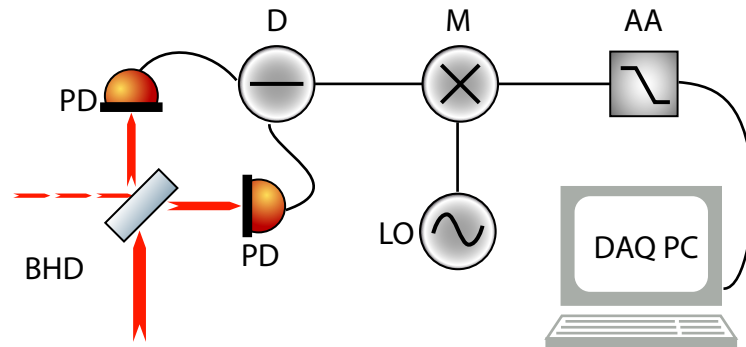


Figure 3.16 - Building blocks of the data acquisition system. D: analog subtractor generating the difference of the signals of the individual BHD photo detectors. M: electronic radio frequency (RF) double balanced mixer to single out the signal of a certain RF modulation mode, see Equation 2.80. LO: local oscillator. AA: anti-aliasing low pass filter. DAQ PC: PC-based analogue to digital converter.

However, care must be taken to correctly map the analogue BHD signals on their digitized forms. Starting from the photo detectors, which convert the photo current of the photo diode into a voltage, the whole chain uses the voltage as quantity to carry the signal. The signals are termed $X_{\gamma}(t)$ with the subscript indicating the node where they occur and have the spectral decomposition $X_{\gamma}(t) = 1/\sqrt{2\pi} \int \tilde{X}_{\gamma}(\omega) e^{i\omega t} d\omega$. Throughout this thesis the frequency of these signals is situated between DC and 50 MHz. The chain of necessary components for this task is shown in Figure 3.16. These components are discussed one at a time.

The quadrature signal is found in the difference of the signals of the two individual photo detectors of a BHD. With Section 2.3.1 in mind, we qualitatively reformulate the photo detector output, i.e. the subtractor input, signal to be $X_{1/2} = g_{1/2}(X_{LO} +/_- X_{\chi})$ with $g_{1/2}$ denoting the electronic gain factors of the two detectors, X_{LO} for the local oscillator contribution and X_{χ} for the quadrature signal. The most crucial quantity for the generation of the difference is the *common mode rejection ration* $CMMR$, which is the ratio of the magnitude, i.e. the absolute value of the amplitude, of the difference signal X_{χ} to the magnitude of the residual sum signal X_{LO} in the output $X_D = X_{\chi} + e^{i\phi} X_{LO}/CMMR$. We require $CMMR > 100$ to render the contribution of X_{LO} to X_D insignificant. The ideal device would generate the output signal $X_D = X_{\chi}$, but in reality the output is contaminated with a small contribution from the sum signal

X_{LO} , which in general can also have a phase shift ϕ_+ . This effect is caused by two major contributions. First, the gain factors for the two input signals can exhibit different frequency characteristics for the magnitude as well as for the phase due to differences between the two detector circuits or impedance mismatching or varying properties of the connection wiring. Secondly, the input and output inevitably couple via the electromagnetic field. Thus, the circuit boards must be designed carefully and the electronic components have to be selected to minimize these effects. In the experiments the difference in magnitude of the gain factors was compensated with variable attenuators for each of the signals.

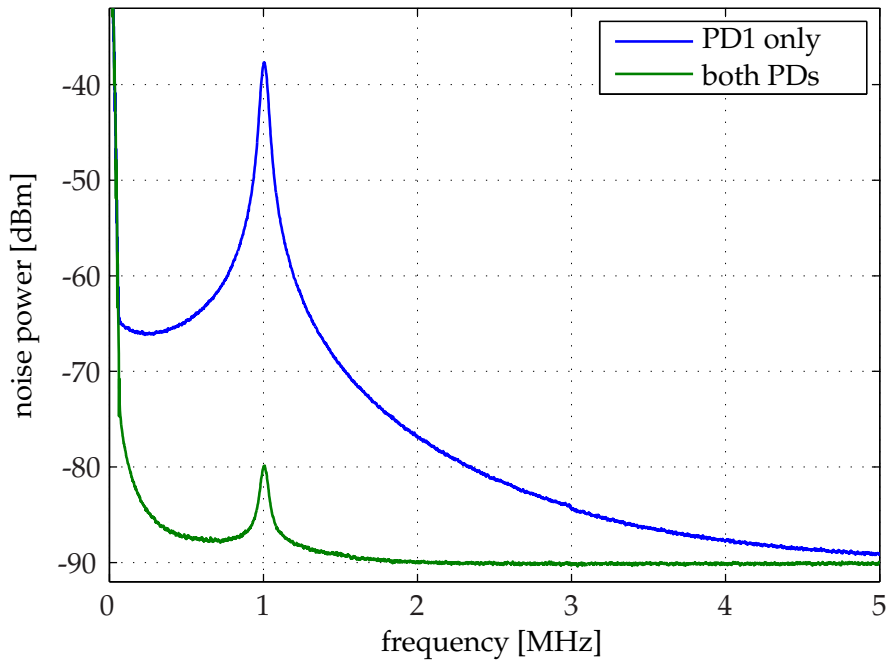


Figure 3.17 - Spectrum of the output X_D of the subtractor. The BHD was run with only the local oscillator at its nominal power and the signal port was blocked. The upper trace is the result of blocking one of the BHD detectors and serves as the reference for half the sum signal power. In case of the lower curve both detectors were illuminated. This displayed that the suppression of the sum signal by the subtractor was more than 40 dB at 1 MHz.

In order to determine the effective $CMRR$ with the components assembled in the experiment the BHD was illuminated with the local oscillator only and the signal port was blocked. Thus, the ideal difference signal power spectrum contains only vacuum noise and the sum maps the intensity noise of the local oscillator. For this measurement an unfiltered fraction of the main laser beam was used, because for the normal operation the intensity noise of the local oscillator was effectively filtered by a high finesse mode cleaner, see Section 3.1.1. However, the unfiltered beam exhibits the intensity fluctuations caused by the laser's relaxation oscillation. With one photo diode of the BHD blocked the output signal turns into $X_D = \frac{1}{2}(X_{LO} + X_X)$, which is dominated by the relaxation oscillation on X_{LO} and serves as a reference for the noise power of X_{LO} .

By comparing this to the spectrum with both BHD detectors illuminated the *CMRR* shows in the difference of the two traces on a logarithmic scale as shown in Figure 3.17. With all components assembled in the experiment it was virtually impossible to measure the common mode rejection for the whole relevant frequency band, because this would have required a strong intensity modulation of the local oscillator in the relevant frequency band. However, since all components were carefully characterized individually beforehand, this measurement was taken to be meaningful for the whole relevant frequency band. When the photo detectors were built they were tuned to show identical transfer functions. The subtractor was checked to have a *CMRR* of more than 40 dB in the frequency range from DC up to 10 MHz, which covers the frequencies of the quantum modulation modes under test.

At the end of the day we want to collect data corresponding to a modulation mode, see Equation 2.80, at the frequency Ω_{mm} in the rotating frame of the fundamental laser field with the bandwidth $\Delta\Omega_{\text{mm}}$ of a quantum light field. The quadrature signal for this mode can be found the BHD difference signal X_{D} in the spectral region of Ω_{mm} and $\Delta\Omega_{\text{mm}}$. Due to technical reasons, see Section 3.1.1 and Section 3.2.2, the preferable frequency range is $5 \text{ MHz} \lesssim \Omega_{\text{mm}} \lesssim 10 \text{ MHz}$, which is too fast for the analogue to digital converter at the end of the chain. For this reason the next link in the chain is the frequency mixer. This device basically multiplies the input X_{D} and the electronic local oscillator X_{eLO} . For the double balanced mixer to work properly, the local oscillator is required to be a square wave signal, see [69, 70]. Thus, the mixer output signal looks like:

$$X_{\text{M}}(t) = X_{\text{D}}(t) \cdot X_{\text{eLO}}(t) = X_{\text{D}}(t) \cdot X_{\text{eLO}} \cdot \text{sign}(\cos(\omega_{\text{eLO}}t + \phi_{\text{eLO}})). \quad (3.10)$$

The spectral decomposition of a square wave with the frequency ω_{eLO} consists of Dirac delta peaks at odd multiples of ω_{eLO} and reads:

$$\tilde{X}_{\text{eLO}}(\omega) = \tilde{X}_{\text{eLO}}^0 \sum_{n=1,3,5,\dots}^{\infty} \frac{1}{n} \delta(\omega - n\omega_{\text{eLO}}). \quad (3.11)$$

The spectral decomposition of X_{M} can be obtained via the Fourier convolution theorem:

$$\tilde{X}_{\text{M}}(\omega) = \frac{1}{\sqrt{2\pi}} \int X_{\text{M}}(t) e^{i\omega t} dt \quad (3.12)$$

$$= \frac{1}{\sqrt{2\pi}} \int X_{\text{D}}(t) X_{\text{eLO}}(t) e^{i\omega t} dt \quad (3.13)$$

$$= \frac{1}{\sqrt{2\pi}} \int_{-\infty}^{\infty} \tilde{X}_{\text{D}}(\omega') \tilde{X}_{\text{eLO}}(\omega - \omega') d\omega'. \quad (3.14)$$

Note that in the last line the integration ranges from $-\infty$ to ∞ . Thus, we extend the spectral decomposition with their *negative frequency* parts, which are the complex conjugate mirror images of the positive parts. With this in mind and inserting Equation 3.11

the integral turns into a sum:

$$\tilde{X}_M(\omega) = \tilde{X}_{eLO}^0 \sum_{n=1,3,5,\dots}^{\infty} \frac{1}{n} [\tilde{X}_D(n\omega_{eLO} - \omega) + \tilde{A}_D^*(n\omega_{eLO} + \omega)]. \quad (3.15)$$

From Equation 3.15 we can read, that we have to choose $\omega_{eLO} = \Omega_{mm}$ to map the desired part of the spectrum around Ω_{mm} of \tilde{X}_D onto the low frequency part around DC of \tilde{X}_M , which is the analogue to digital converter capable of. However, e.g. for $\omega = 0$ we also find contributions from higher frequency components of \tilde{X}_D corresponding to all odd multiples of ω_{eLO} and likewise for all frequencies. Thus, we have to make sure, that all frequency components starting from $3\omega_{eLO}$ and above are sufficiently attenuated to not mask the desired signal. For this purpose a low pass filter with a pass band $1.5\omega_{eLO}$ and a roll-off of 12 dB/octave sits in front of the mixer input. Together with the $1/n$ Fourier expansion coefficients this provides an minimum attenuation of more than 20 dB, which is sufficient, as the level of the unwanted components of X_D is similar to the desired one.

Coming closer to the analogue to digital converter (ADC) we have a first look at the digitizing process (sampling). The ADC converts a Voltage at its input into a binary number representation with a certain number of bits, which can be read by a computer at a certain instant of time and is termed *sample*. Only after a while the computer can read the next sample. Usually, the sampling is done with equidistant time intervals. The corresponding frequency is called sampling rate f_s .

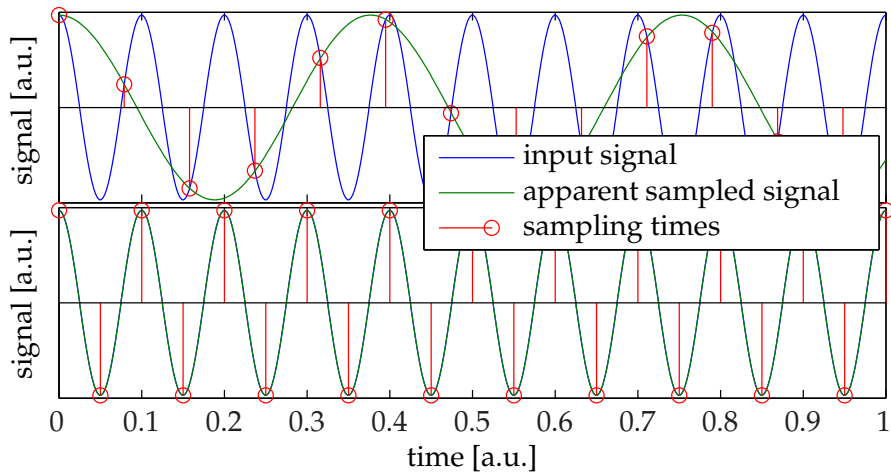


Figure 3.18 - (Aliasing) caused by the signal frequency being too high for the given sampling rate. In the upper part the sampling rate is lower than half of signal (blue) frequency, i.e. between two samples (red circles) a little more than half a signal period has passed. Given the samples only an unbiased guess of the initial signal may result in the green curve, the alias. The lower figure shows the minimum sampling rate required to render the unbiased guess unique, which is twice the signal frequency.

Signal variations, which occur temporally in between two sampling instants, cannot

be detected. The crucial consequence is called *aliasing*, which is illustrated in Figure 3.18. Let $\tilde{X}_s(\omega)$ the Fourier frequency representation of a signal to be sampled. The blue curve in Figure 3.18 represents the highest frequency ω_h component of the signal $X_h(t)$: $\tilde{X}_s(\omega > \omega_h) \approx 0$. If the sampling rate is lower than twice ω_h , the sampled data can be mistaken to originate from an alias signal. For a detailed analysis see [71] or [72]. To be on the safe side and for the sake of simplicity we require:

$$f_s \geq \frac{2\omega_h}{2\pi}. \quad (3.16)$$

Note that in principle aliasing would not be an issue for the experiments within this thesis, because we do not want to know how the signal exactly looked like but are only interested in the statistics. If we could rely on the quantum light field to be prepared in identical states for all modulation frequencies, the aliasing would only define a funny structure of the modulation mode under test, see Equation 2.80. However, for technical reasons, e.g. the laser noise, this was not true, and hence we did not want aliasing.

A low pass frequency filter can be used to suppress the frequency components of the signal beyond $f_s/2$ and prevent aliasing. Such a filter is called anti-aliasing (AA) filter. A good introduction to filters is provided by [73] and [74]. Linear, time invariant filters can be characterized by their transfer functions $\tilde{h}(\omega) = g(\omega) e^{i\phi(\omega)}$ for sinusoids of the frequency ω , i.e. the magnitude or gain $g(\omega)$ and phase $\phi(\omega)$ of the frequency response. In Fourier space the output signal $\tilde{A}(\omega)_{AA}$ as result of the action of the filter on the input signal $\tilde{X}(\omega)_M$ is expressed by $\tilde{X}(\omega)_{AA} = \tilde{h}(\omega)\tilde{X}(\omega)_M$. Another important characteristic of a filter is the *group delay* $\tau_d(\omega)$. This is the time shift after the filter of a slowly varying amplitude envelope of a sinusoid with the frequency ω . The group delay can be derived from the phase of the frequency response via $\tau_d(\omega) = \partial_\omega \phi(\omega)$.

On the one hand, the AA filter should provide sufficient attenuation, see next paragraph, in the stop band above $f_s/2$. On the other hand, the pass band, i.e. the frequency region with $g(\omega) > \sqrt{1/2}g(0)$, should be as wide as possible. This is, because the measurement time required to gather a significant amount of data becomes larger as the signal bandwidth is reduced. Thus, the first idea is to use a filter, whose transfer function is close to the *Heaviside* step function. However, an electronic implementation of a filter like this is hard to build and very sensitive to the actual values of the components determining the filter response. As a rule of thumb: the steeper the roll-off between pass band and stop band must be, the more crucial are the components. By carefully selecting every single key component it is possible to assemble unique filters with a very steep roll-off, but it is virtually impossible to build several exact copies. However, an experiment as presented within this thesis, see Section 4.4, aiming on measuring the correlation amongst simultaneous samples of several signals requires identical filters, because otherwise the correlations may be destroyed. Variations of τ_d , which exceed the sampling period $\tau_s = 1/f_s$, cause a loss of sample-wise synchrony. Hence, a more robust filter design has to be used.

The attenuation g_{sb} required in the stop band can be found by looking at the downstream ADC, which provides a certain resolution, i.e. the number of bits N_r the input

signal is represented by. To make use of the full resolution, i.e. use all of the 2^{N_r} different numbers, the input voltage has to be scaled in such a way, that the maximum voltage V_{\max} occurring is converted into the largest number and the minimal voltage V_{\min} into the smallest with $N_r - 1$ intervals in between. Given a linear ADC, the width of these intervals is voltage resolution $V_{\text{res}} = (V_{\max} - V_{\min})/2^{(N_r - 1)}$. For symmetrical voltage swings symmetrical around zero the resolution is:

$$V_{\text{res}} = V_{\max}/2^{N_r-2}. \quad (3.17)$$

Everything smaller than that counts as zero. Thus, to render the aliases undetected we require $g_{\text{sb}} < 2^{-N_r+2}$.

For the experiments presented within this thesis up to six identical filters were required, see Section 4.4. As these experiments were focussed on the detection of correlation we focussed on a filter design, which is robust under variations of the values of the electronic components. A good starting point was a filter of the *Bessel* [75] type showing a constant group delay within the pass band. The software FilterCAD provided by the semi-conductor component manufacturer Linear Technologies was used to find an appropriate design of the transfer function ending up with a 6th order model. A suitable electronic circuit based on a passive network of inductors and capacitors was designed for the electronic implementation. The component values for this circuit were not uniquely determined by the transfer function. Thus, in a next step the program liso written by Gerhardt Heinzl [76] was used to find a robust compilation of component values. The sampling frequency was fixed at 1 MHz for all experiments presented here, except for Section 4.2. Following Equation 3.16, the filters were required to exhibit a sufficient attenuation above 500 kHz. Our ADC provided a resolution of $N_r = 14$ bit. The signals had symmetric voltage swings and we gave a headroom of a factor of two for the maximum voltage which yielded $V_{\text{res}} = V_{\max}/2^{11}$. Thus, the attenuation of the AA filter above 500 kHz had to be better than $V_{\text{res}}/V_{\max} = 2^{-11} = -66$ dB. The measured transfer functions of all six filters are shown in Figure 3.19, showing that the filters are well suitable for our purpose.

The last link in the DAQ system chain was the ADC. We chose the NI PCI-6133 by National Instruments, which was run in a PC with the graphical programming environment LabView. The ADC provided eight analogue input channels with a resolution of 14bit, which could be sampled simultaneously with up to three million samples per second. On board memory for 32 million samples ensured that samples were collected even when the PC was busy, e.g. drawing the mouse cursor. Numerous LabView programs were written for the online-monitoring of the experiments during the set up and adjustment phase and of course to collect and store the final measurement data. The LabView-environment was also used to control the experiments involving quantum state tomography, see Section 2.3.2.

The process of analogue to digital conversion also introduces extra noise, see [77]. This is because the continuous signal is quantized into discrete values, which differ from the original signal by up to half of the voltage resolution V_{res} , see Figure 3.20. We can estimate the strength of this noise by assuming that the original signal varies

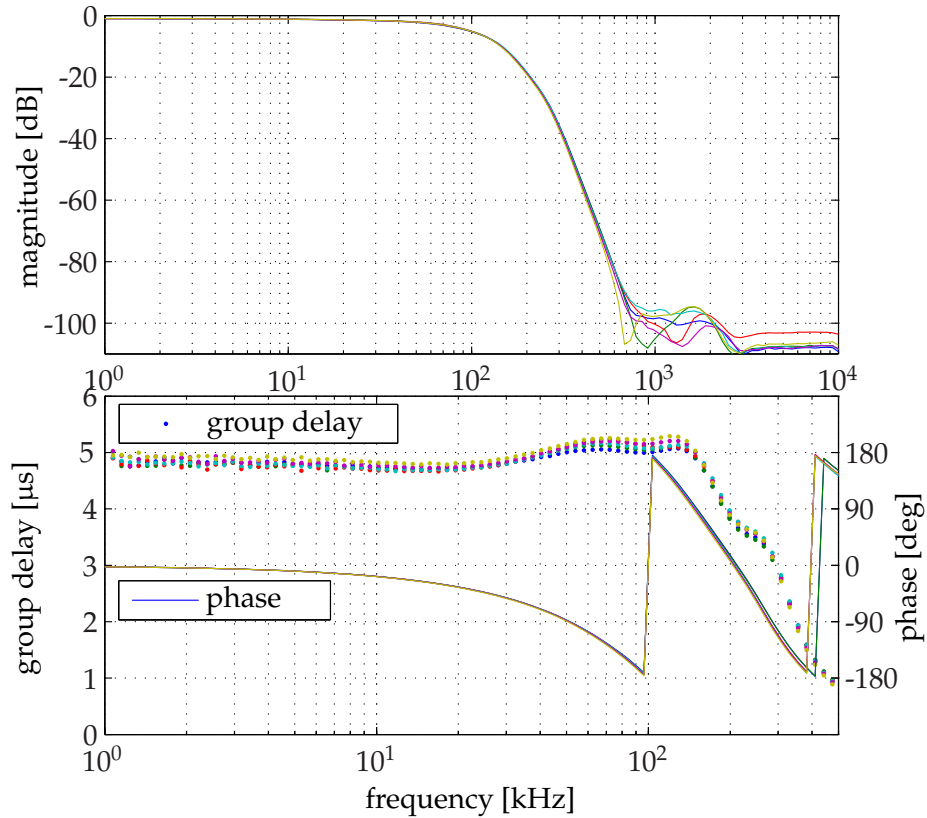


Figure 3.19 - Characteristics of six AA filters. Top: The magnitude of the frequency response was well suitable for an AA filter. The attenuation at 450 kHz was almost -70 dB and even better for higher frequencies. Bottom: The group delay was derived from the phase of the frequency response. It was almost constant within the pass band, and the largest differences amongst all traces is well below the sampling period of 1 μ s.

linearly within the time interval t_q from one quantization step to the next. The deviation of the quantized value from the original then reads:

$$\epsilon(t) = \frac{V_{\text{res}}}{t_d} t, \quad (3.18)$$

with the $t = 0$ at the centre of the considered level. Note that the average is zero and thus the corresponding variance is given by:

$$\sigma^2(\epsilon) = \frac{1}{t_d} \int_{-t_d/2}^{t_d/2} \left(\frac{V_{\text{res}}}{t_d} t \right)^2 dt = \frac{1}{12} V_{\text{res}}^2. \quad (3.19)$$

How did this relate to the experimental parameters? The overall voltage gain in the DAQ-system was set such, that the largest signal fell within the voltage range of the ADC. Strictly spoken this cannot be true for Gaussian noise but we hardly observed a

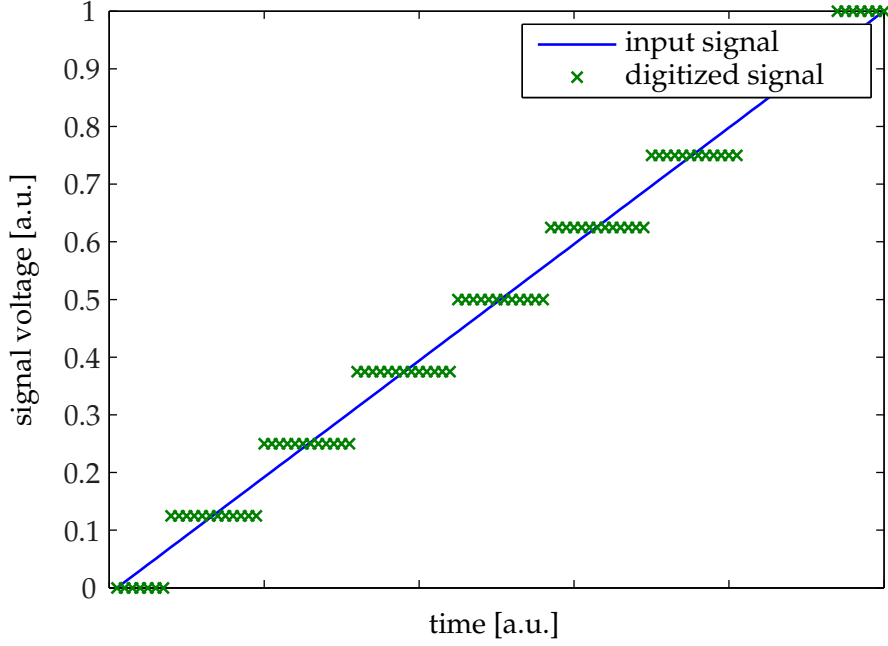


Figure 3.20 - Quantization noise caused by the deviation of the quantized value (green crosses) from the original continuous signal (blue line). The vertical distance between the levels of the green crosses is the voltage resolution V_{res} .

sample at the edge of the input range. The rate was of the order of one out of ten million. Assuming Gaussian noise we could deduce from the error function that the input voltage range must have been roughly five times the standard deviation of the input signal. The largest signal was the noise from the anti-squeezed quadrature measurement, which had a standard deviation three times (10 dB) larger than that for the vacuum noise. The latter, in turn, was ten times (20 dB) bigger than the BHD dark noise. Thus, the input voltage range V_{max} was $3 \cdot 5 \cdot 10 \approx 2^8$ times larger than the standard deviation of the BHD dark noise signal σ_{dn} , or using Equation 3.17 and Equation 3.19:

$$\sigma(\epsilon) = \sqrt{12} V_{res} = \frac{\sqrt{12}}{2^{11}} V_{max} \approx \frac{\sqrt{12} 2^8}{2^{11}} \sigma_{dn} \approx \frac{4}{100} \sigma_{dn}. \quad (3.20)$$

Finally, we did not need to worry about digitizing noise, because it was more than ten times smaller than the dark noise of the BHD.

3.6 Random Phase Diffusion

The controlled diffusion of the optical phase of a quantum light mode played an important role for the underlying work, as it was used in all experiments presented in the next section. The intention was to jiggle the angular orientation of the quadrature axes in phase space rather than to excite the phase quadrature of the modulation mode un-

der test at a few Megahertz, see Equation 2.80. Thus, the spectrum of the applied phase diffusion had to be bound to frequencies far below the frequency of the considered modulation mode, such that when moving into the rotating frame of the modulation mode, the diffused phase can be treated as a slowly varying factor. However, to perform a meaningful quadrature detection the phase had to be stabilized for very low frequencies corresponding to the time it took to collect a significant number of quadrature samples, i.e. at least some milliseconds. These constraints left us with the audio frequency band above 1 KHz for the spectrum of the phase diffusion.

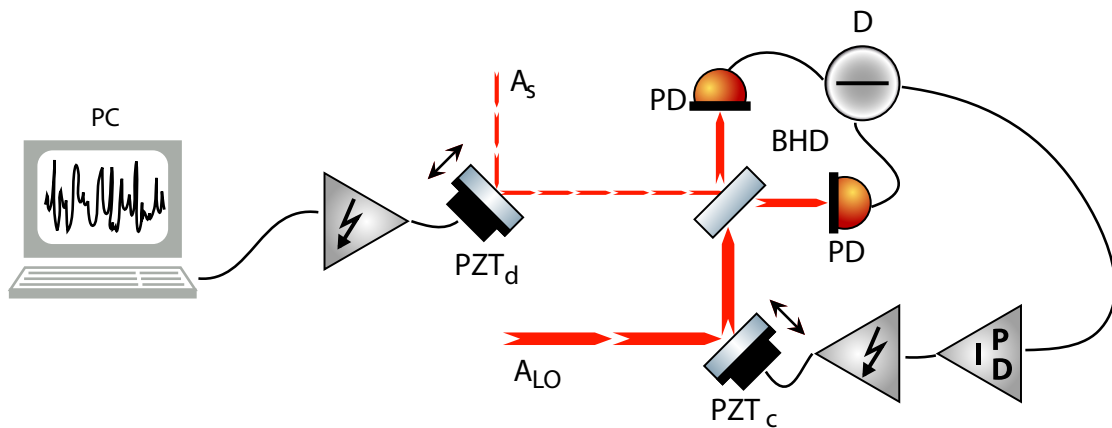


Figure 3.21 - Application of phase diffusion. A (PC) soundcard produced the desired phase diffusion signal to actuate on the phase of the signal beam (X_s) via (PZT_d). The average detection phase of the BHD was controlled by an independent actuator (PZT_c) in the path of the local oscillator (LO).

As shown in Figure 3.21 we used movable mirrors driven by piezo-electric transducers (PZT) to microscopically change the optical path length and thus actuate the optical phase with respect to a fixed reference, e.g. the BHD. Technically this is equivalent the way the optical phase was usually controlled and stabilized for interferometers, e.g. the BHD. A PC sound card was used to produce the desired voltage signal, which had to be amplified by a powerful amplifier. The PZTs we used had an electrical capacitance of around 100 nF and provided a spatial displacement of $1 \mu\text{m}$ per 100 V or a phase displacement of 2π per 100V. Thus, to make the phase diffusion cover a full revolution in phase space, which changes at a rate of more than a Kilohertz, the amplifier was required to provide an amplitude of 100 V at these frequencies. The PZT capacitance led to an impedance Z at 5 kHz of $|Z| = 1/(2\pi \cdot 5 \text{ kHz} \cdot 100 \text{ nF}) \approx 300\Omega$. Hence, the amplifier had to provide a current of a few hundred Milliampere at 100 V at a few Kilohertz. Although this looked like using a Hifi amplifier, we decided to build our own, because they are usually not designed to drive capacitive loads and specification for this regime were hardly available.

The sound file to be played back by the PC for the appropriate signal was a priori generated with a modified random number generator in MATLAB, see Figure 3.23. As stated before, the signal was required to show a certain spectrum. The PZTs showed a

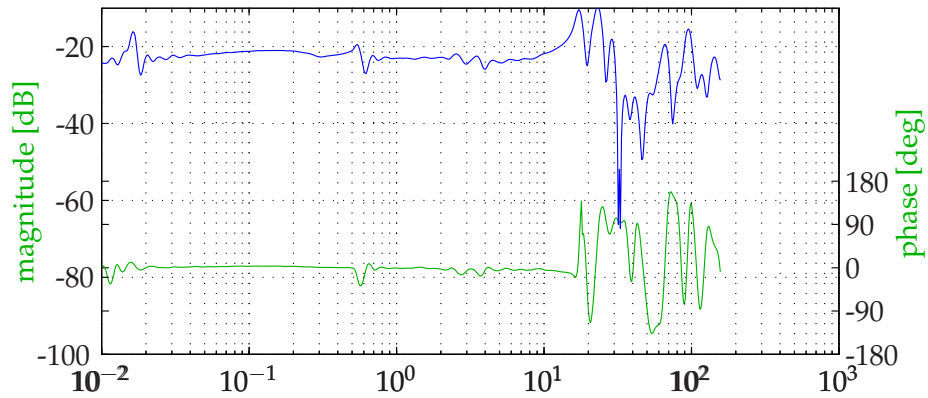


Figure 3.22 - Typical PZT transfer function from amplifier input to optical phase. A BHD was used to detect the phase of a beam which was reflected from a PZT actuated mirror. All tested PZTs showed similar transfer functions. Note the flat part up to 10 kHz.

flat transfer function for frequencies lower than 10 kHz, see Figure 3.22. To make sure, that the PZT truly mapped the input signal onto the optical phase, the frequency range was restricted to 5 kHz from above. The lower limit was set to 1 kHz. This provided enough headroom for the phase diffusion not to interfere with any phase control loop. Additionally, the probability distribution had to be Gaussian to be compatible with the preceding theoretical analysis. These characteristics are shown in Figure 3.23.

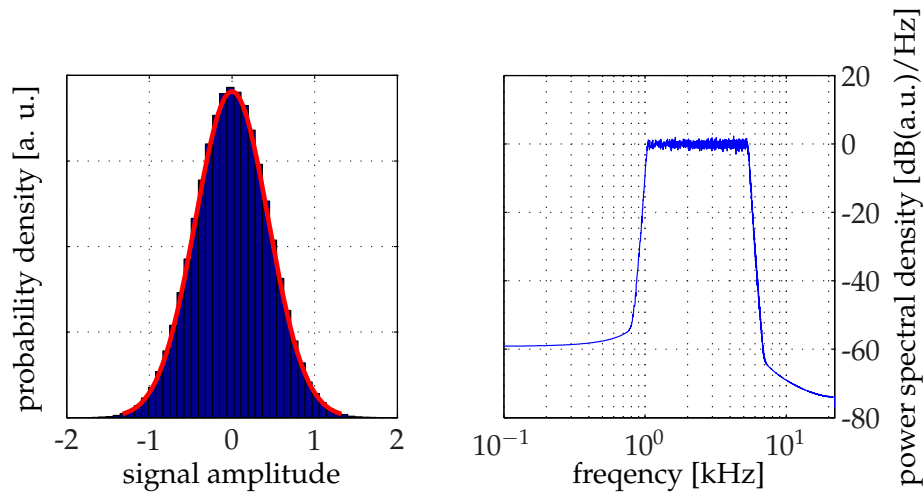


Figure 3.23 - Probability distribution and power spectral density of the phase diffusion signal. The phase distribution was Gaussian as can be seen in the left figure showing a Gaussian fit. The spectrum was well confined between one and five Kilohertz.

The amplifier gain was adjustable by means of a potentiometer to vary the strength of the phase diffusion, which was quantified in terms of the standard deviation σ_ϕ . We assumed a linear relation between σ_ϕ and the potentiometer scale P : $\sigma_\phi = m \cdot P$. To determine m we locked the BHD to measure the phase quadrature and directly

observed the standard deviation of the difference signal X_D without demodulation for different potentiometer settings, as shown in Figure 3.24. However, there were a few considerations necessary to finally obtain m .

With ϕ denoting the deviation from the detection phase corresponding to the phase quadrature, the difference signal reads:

$$X_D = X_D^0 \sin \phi. \quad (3.21)$$

For very small values of σ_ϕ we can assume $\sigma_\phi = \sigma(X_D)/X_D^0 =: \sigma_D$. However, to quantify stronger diffusions we have to find the function f , which maps $\sigma_D = f(\sigma_\phi)$. The probability distribution $p_D(x)$ of the BHD signal X_D/X_D^0 is related to that of the phase $p_\phi(\phi)$ via:

$$p_D(x) = \int_{-\infty}^{\infty} \delta(x - \sin \phi) p_\phi(\phi) d\phi, \quad (3.22)$$

with Equation 3.21 used in the Kronecker delta distribution. To solve the integral we first have to slice the integration in bijective pieces with respect to $\sin \phi$:

$$p_D(x) = \sum_{n=-\infty}^{\infty} \left(\int_{-\pi/2+2\pi n}^{\pi/2+2\pi n} \delta(x - \sin \phi) p_\phi(\phi) d\phi + \int_{\pi/2+2\pi n}^{3\pi/2+2\pi n} \delta(x - \sin \phi) p_\phi(\phi) d\phi \right). \quad (3.23)$$

We change variables $\phi = \arcsin y$ and $d\phi = dy/\sqrt{1-y^2}$ and obtain:

$$\begin{aligned} p_D(x) &= \sum_{n=-\infty}^{\infty} \left(\int_{-1}^1 \frac{\delta(x-y) p_\phi(\arcsin y + 2n\pi)}{\sqrt{1-y^2}} dy + \right. \\ &\quad \left. \int_{-1}^1 \frac{\delta(x-y) p_\phi(\arcsin y + (2n+1)\pi)}{\sqrt{1-y^2}} dy \right) \\ &= \sum_{n=-\infty}^{\infty} \left(\frac{p_\phi(\arcsin x + 2n\pi)}{\sqrt{1-x^2}} + \frac{p_\phi(\arcsin x + (2n+1)\pi)}{\sqrt{1-x^2}} \right). \end{aligned} \quad (3.24)$$

The result for $p_D(x)$ can be used to obtain σ_D via:

$$\sigma_D = \sqrt{\int_{-1}^1 x^2 p_D(x) dx}. \quad (3.25)$$

Given a Gaussian distribution of the phase diffusion $p_\phi(\phi) = \frac{1}{\sqrt{2\pi\sigma_\phi^2}} e^{-\phi^2/(2\sigma_\phi^2)}$

we obtain an expression for $\sigma_D(\sigma_\phi)$ using Equation 3.24 and Equation 3.25 with the assistance of a computer algebra program:

$$\begin{aligned} \sigma_D(\sigma_\phi) = \sum_{n=-\infty}^{\infty} \frac{1}{4} & \left[\operatorname{erf} \left(\frac{(4n+3)\pi}{2\sqrt{2}\sigma_\phi} \right) - \operatorname{erf} \left(\frac{(4n-1)\pi}{2\sqrt{2}\sigma_\phi} \right) \right. \\ & - \Re \left(e^{-2\sigma_\phi^2 - 4in\pi} \operatorname{erf} \left(\frac{(4n+3)\pi - 4i\sigma_\phi^2}{2\sqrt{2}\sigma_\phi} \right) \right) \\ & \left. - \Re \left(e^{-2\sigma_\phi^2 - 4in\pi} \operatorname{erf} \left(\frac{4i\sigma_\phi^2 - 4n\pi + \pi}{2\sqrt{2}\sigma_\phi} \right) \right) \right]. \end{aligned} \quad (3.26)$$

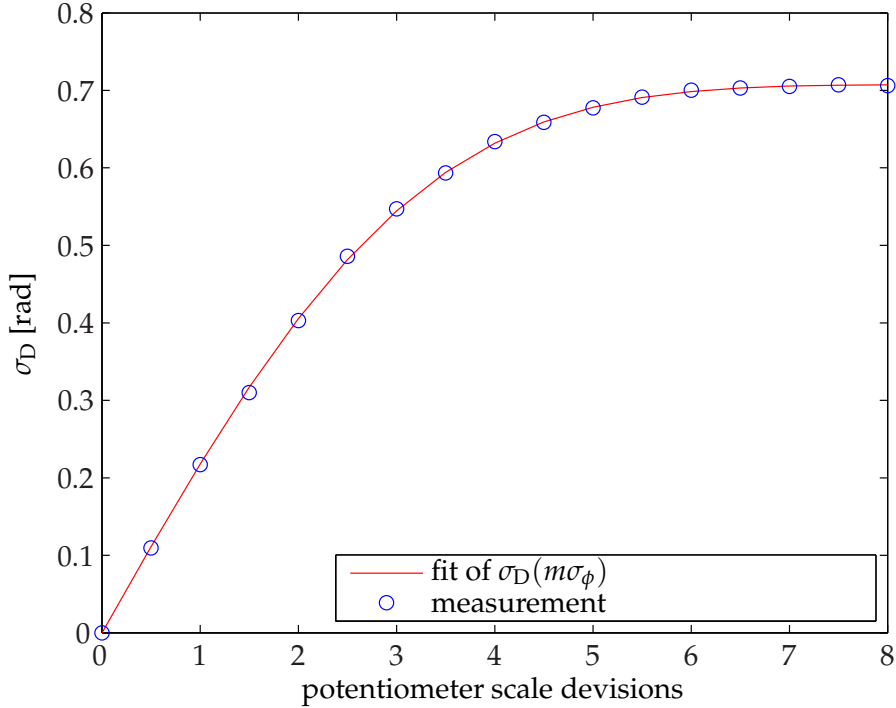


Figure 3.24 - Measurement of the standard deviation of the BHD signal. The strength of the phase diffusion was varied using a potentiometer. A fit of the function $\sigma_D(\sigma_\phi) = \sigma_D(mP)$, see Equation 3.26, was used to obtain m and to gauge $\sigma_\phi = mP$ the potentiometer scale P .

Turning back to the experiment we measured σ_D for various gain settings of the amplifier quantified by the potentiometer scale P , as shown in Figure 3.24. In order to find the slope coefficient m in $\sigma_\phi = m \cdot P$, we fitted $\sigma_D(mP)$ from Equation 3.26 via m . As described in Section 4.4, we used up to six quantum light modes, which needed a phase diffusion to be applied. Because of variations between the various components in the phase diffusion path, the above procedure was carried out for each path individually.

Experiments

All experiments presented in this section rely on the sampling, see Section 3.5, of the quadrature distribution of a quantum light mode, see Section 2.74, by means of balanced homodyne detection (BHD), see Section 3.3.

4.1 Preparation and Characterization of Phase-Diffused Squeezed States

This experiment aimed on the application of a novel criterion [78] for the non-classicality of quantum states, i.e. those states which lack a classical counterpart. The criterion says, that if the characteristic function $\tilde{P}(\zeta, \phi)$ of the Glauber-Sudarshan P-function [79], see Section 2.1.3, exceeds the corresponding function of the vacuum $|\tilde{P}_{\text{vacuum}}| \equiv 1$ the underlying state will be non-classical. With $\beta = \zeta e^{i\phi}$, if

$$\exists \beta : |\tilde{P}(\beta)| > 1, \quad (4.1)$$

the state will be non-classical. It was shown in [78], how to obtain $\tilde{P}(\zeta, \phi)$ from a quadrature sampling experiment, with Q_ϕ representing the samples of the BHD for the detection phase ϕ :

$$\tilde{P}(\zeta, \phi) \cong e^{\zeta^2} \langle\langle e^{i\zeta Q_\phi} \rangle\rangle. \quad (4.2)$$

Note that the approximation symbol indicates, that the right hand side is a statistical estimator for a finite number of samples.

The remarkable properties of the novel criterion are, that it is easy to test from an experimentalist's point of view, and that it is weaker than other criteria, i.e. it can detect a greater class of non-classical states. During a lunch break conversation on a conference with W. Vogel, the author of [78], we found out that phase-diffused squeezed states, see Section 2.2.2 may be suitable to demonstrate the power of the proposed criterion. A subsequent visit of Vogel and two of his students in our group in Hanover clarified

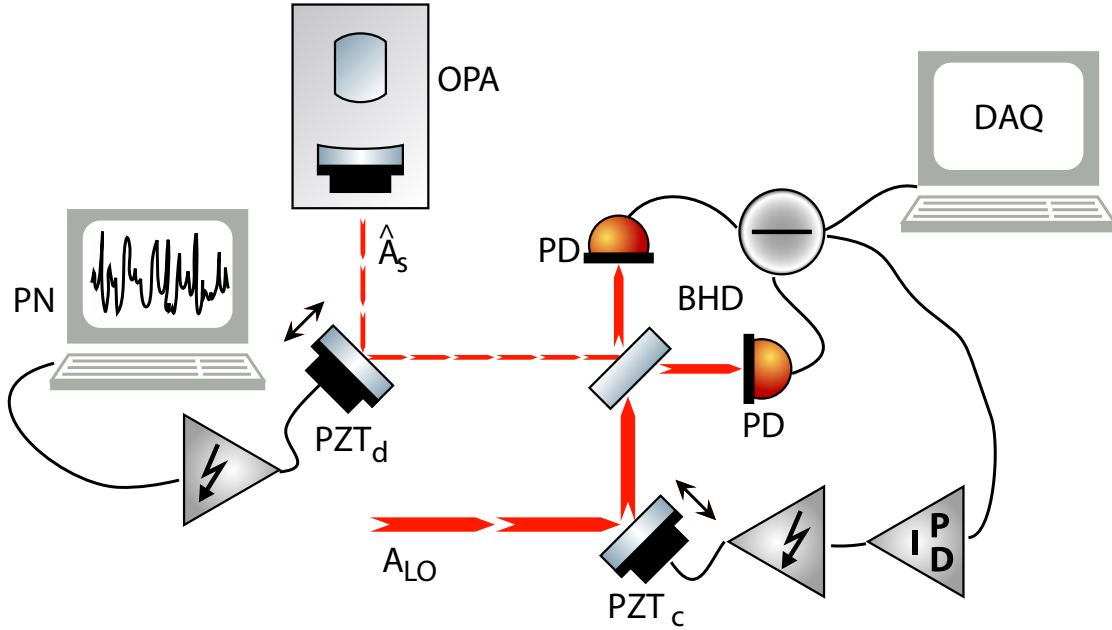


Figure 4.1 - Setup for the generation and detection of phase-diffused squeezed states. Squeezing was generated by an optical parametric amplifier (OPA), and the squeezing orientation was diffused by a noise signal (PN) fed on a phase shifter PZT_d . The detection phase of the BHD was controlled by a feedback loop via PZT_c . The BHD signal was sampled by the data acquisition system (DAQ).

this.

The experimental setup for the generation and detection of phase-diffused squeezed states is shown in Figure 4.1. In a first instance a squeezed state was generated by an optical parametric amplifier (OPA), see Section 3.2. We chose the modulation mode at 6.7 MHz with a bandwidth of 800 kHz as a carrier for state. The OPA was operated such, that it produced a squeezed variance of $V_s = 0.36 = -4.44$ dB and an anti-squeezing of $V_s = 5.28 = -7.23$ dB with respect to the variance of the vacuum normalized to unity. A phase diffusion with Gaussian distribution was applied with four different standard deviations σ_ϕ by a phase shifter (PZT_d , Figure 4.1) between the OPA and the BHD, as described in Section 3.6. The procedure to obtain a gauge for the phase diffusion standard deviation is found in the same section.

Additionally, a fully phase-diffused state with an uniform phase distribution should be prepared. However, the above scheme had a limited maximum amplitude due to a limited power of the amplifier driving the phase shifter. Additionally there were constraints, especially from below, to the spectrum of the phase diffusion. These were imposed to prevent BHD phase control loop from interfering with the phase diffusion. The spectrum was also limited from above because of the $1/f$ roll-off of the electrical impedance of the phase shifter. That means, that the current needed for a constant amplitude scales linear with the frequency. With a truly uniform phase distribution the quadrature measurement cannot depend on the average BHD detection angle. Thus,

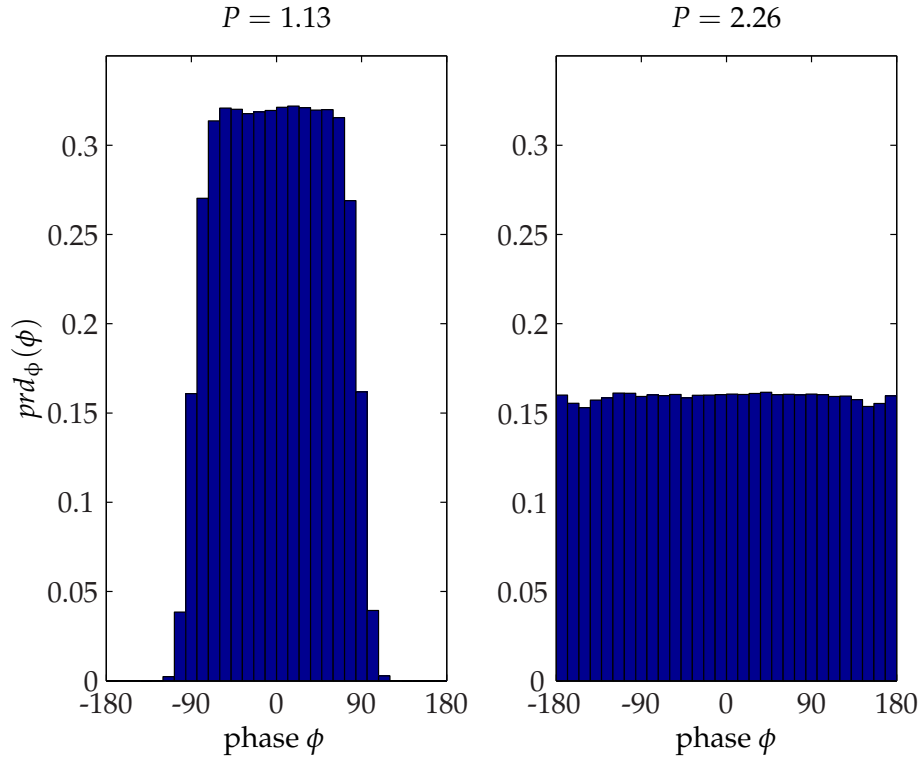


Figure 4.2 - Measured phase distribution of the phase-diffused field for different gain factors P for the width of the distribution. Left: Due to the electro-mechanical low pass characteristic of the phase shifter the phase distribution was not exactly uniform although the driving signal was. Right: With the right setting of P a truly uniform phase could be achieved because phases modulo 2π are indistinguishable.

there was no need to control it and we could release the constraints to the spectrum for low frequencies, which enabled us to increase the amplitude. We also modified the signal driving the phase shifter to have an uniform distribution.

In order to verify a flat phase distribution of the field under test in the first place we needed to measure the phase. The beam carrying the squeezed mode also carried some light from the fundamental laser with a radio frequency modulation. Given this the DC signal of the BHD X_c depended on the phase ϕ with respect to the amplitude quadrature like $X_c = X_c^0 \cos \phi$ and the demodulated signal X_s of the radio frequency modulation looked like $X_s = X_s^0 \sin \phi$, see Section A.1. With the electronic gains adjusted in that way, that $X_s^0 = X_c^0$ we could derive the phase from a simultaneous measurement of these two signals via:

$$\phi = \arg(X_c + iX_s). \quad (4.3)$$

The measured distributions are shown on Figure 4.2. Although the signal driving the phase shifter had an uniform distribution this could not be exactly mapped on the optical phase as long as the width of the distribution was smaller than 2π and the sharp

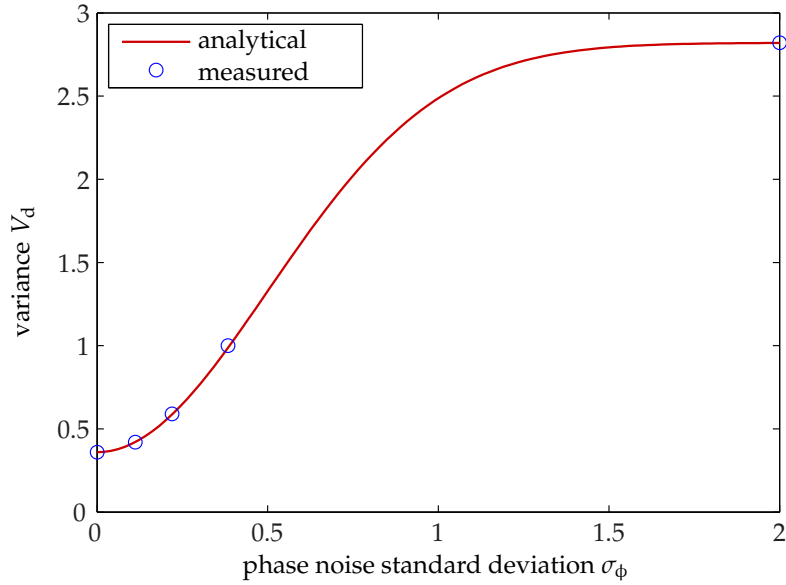


Figure 4.3 - Resulting variance of the initially squeezed quadrature after applying the phase diffusion with different standard deviations σ_ϕ .

edges were eroded. This effect was caused by the low pass characteristic of the transfer function from the electrical input to the optical phase as shown in Figure 3.22. However, we could benefit from the fact that the phase is indistinguishable with a modulus of 2π . For a certain width of the distribution, which was adjustable, the *wing* of one of the eroded edges could fill up the missing part of the other. The right hand side of Figure 4.2 shows that we were able to generate a truly uniform distribution.

We measured the minimum quadrature variances for the different levels of phase diffusion, as shown in Figure 4.3. We found a perfect match of the measured variances and the theoretical prediction of Equation 2.39. We found that for a Gaussian phase diffusion with a standard deviation of $\sigma_\phi = 22.2^\circ$ the squeezing effect of the variance is no longer observable and one would be considered to be classical. However, phase-diffused squeezed states are non-Gaussian and hence cannot be completely characterized by their quadrature variance.

The main results were presented in [80], where also other criteria for non-classicality are considered such as the squeezing of statistical moments higher than the variance [81] or the positive semi-definiteness of certain matrices of normally ordered moments [82]. At least for the completely phase-diffused states these failed to reveal non-classicality. The criterion based on the characteristic function, however, detected non-classicality for all states with a high statistical significance, as shown in Figure 4.4. This result agrees with the ordering of the strength of different criteria in [83].

The results were presented in [80], where it was also shown that the novel criterion could outperform several existing criteria.

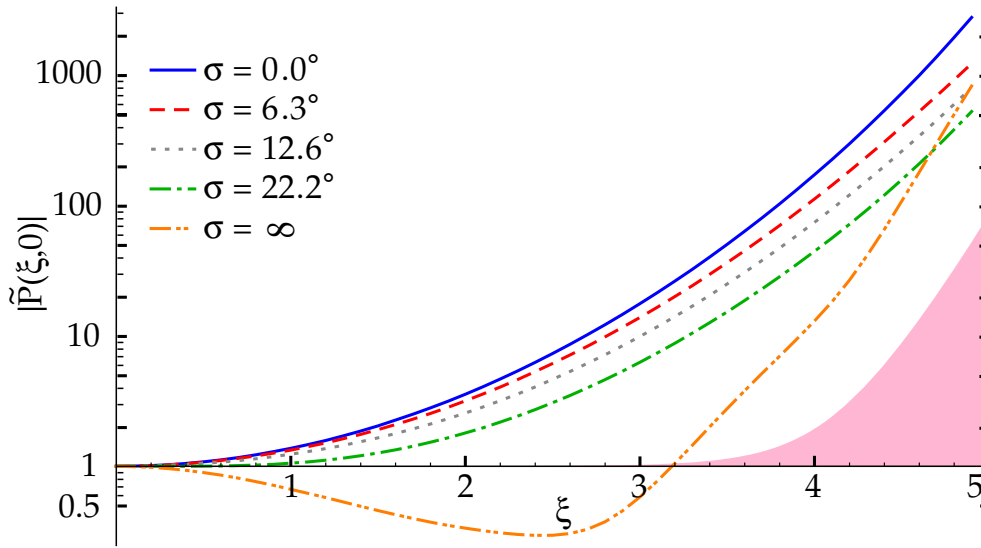


Figure 4.4 - Measured characteristic functions for different phase-diffused states. The reddish area represents one standard deviation, which was added to the classical limit of $|\tilde{P}(\xi, 0)| = 1$ and thus marks the *safe* limit of being non-classical.

4.2 Distillation and Purification of Phase-Diffused Squeezed States

The experiment presented in this section was a precursor for the experiments from the next two sections, which provided great insight on our distillation / purification protocol.

The experimental setup is shown in Figure 4.5. We used two optical parametric amplifiers (OPAs), see Section 3.2, which were operated such in that manner, that both prepared identical squeezed states. The variance of the squeezed amplitude quadrature was -5.0 dB and $+9.3$ dB for the anti-squeezed phase quadrature, both corresponding to the modulation mode of the OPA field at the frequency of 7 MHz with a bandwidth of 80 KHz.

To realistically mimic the effects of noisy optical transmission channels each squeezed beam was reflected off a high-reflective mirror that was randomly shifted by a PZT, see Section 3.6. Hence, random phase shifts were introduced on the beams as they would occur when transmitting the beams through optical fibres of considerable lengths. The voltages driving the PZTs were carefully produced to meet certain criteria. Although no special form of the noise is in principle required for a purification/distillation experiment, we wanted to operate in a regime where the noise has well defined properties and could be easily modelled theoretically. The phase diffusion showed a Gaussian distribution with a spectrum confined in the frequency range 1 – 5 kHz. Performing homodyne detection on each of the beams confirmed that the amount of squeezing degraded in the same way the strength of the phase noise was increased, see Figure 4.6

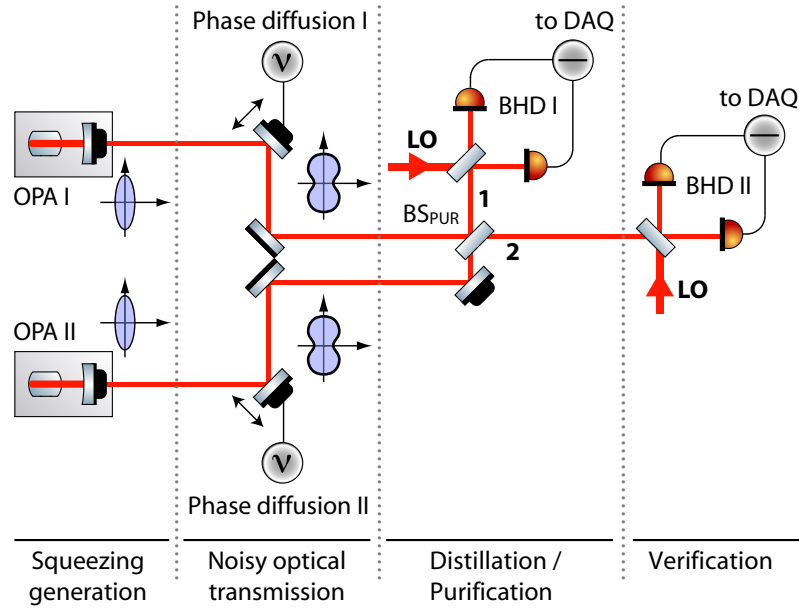


Figure 4.5 - Schematic experimental set-up for the demonstration of purification/distillation of phase-diffused squeezed states. Two OPAs (OPA I and OPA II) produced one amplitude-squeezed beam each. Two piezo-electric transducers PZTs drove mirrors to induce random Gaussian-weighted phase shifts to each beam to mimic the effect of a noisy optical transmission. The two phase-diffused beams were then superimposed on a balanced (50/50) beam-splitter (BS_{PUR}). Two balanced homodyne detectors (BHD I and BHD II) in combination with a digital data acquisition system synchronously recorded time series of measured quadrature values. BHD II serves the purpose of verification and can be replaced by an arbitrary experiment, which requires a squeezed input beam.

(black curve/circles).

In order to demonstrate purification/distillation the two phase-diffused squeezed beams were superimposed on a balanced (50/50) beam splitter. Here, a visibility of 98.2% was achieved. The relative phase of the two beams on the beam splitter was actively controlled (with a control loop bandwidth *below* the phase noise frequency band) using phase modulation side bands present on the squeezed beams. The output beams from the beam splitter were then detected using the homodyne detectors BHD I and BHD II, each of which was servo-controlled to detect the appropriate quadratures using the technique described in the first part of Section A.1. The feedback control loop bandwidths were chosen to be *smaller* than the phase diffusion frequencies. The BHDs were constructed from matched pairs of ETX-500 high-efficiency photo diodes, see Section A.2.1. The visibilities for the BHDs were 98.4% for HD I and 98.7% for HD II. Each detector difference current was subsequently electronically mixed with a 7 MHz local oscillator. The demodulated signals were then filtered with steep low-pass filters (anti-aliasing filters) at 40 kHz and synchronously sampled with 100 kHz, see Section 3.5. The slightly different non-linear phase response of these filters was compensated with appropriate IIR filters after the data were sampled to effectively regain a constant group delay. Both sampled time series of quadrature values from BHD I and BHD II,

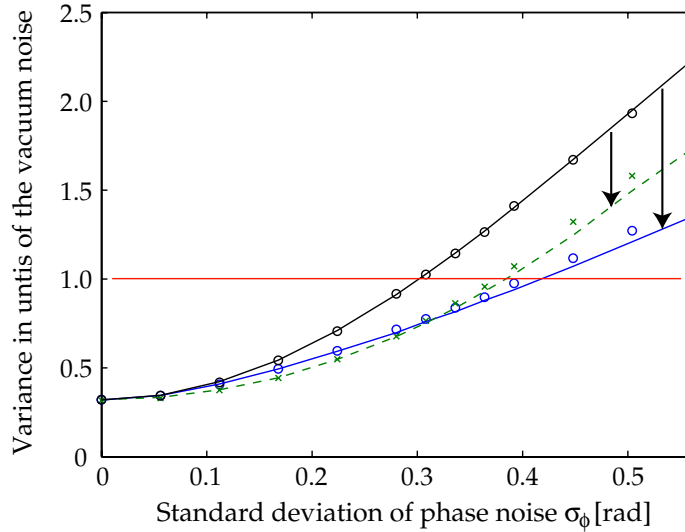


Figure 4.6 - Demonstration of successful distillation of squeezed states for two different trigger strategies versus strength of phase fluctuations σ . Shown are measured variances of the (initially) squeezed quadrature for the phase-diffused input states V_{in} (top, black) and for distilled states V_{out} , when conditioned on the squeezed quadrature $|q_1| < Q$ (circles, blue) and when conditioned on the anti-squeezed quadrature $|p_1| < Q$ (crosses, green), respectively. Theoretical values are represented by solid and dashed lines. Here, the trigger threshold was set to $Q = 1.0$. For $\sigma < 0.3$ conditioning on the anti-squeezed quadrature was more efficient than conditioning on the squeezed quadrature. The red line indicates the shot-noise level. Without phase diffusion the squeezed state variances were measured to $V_s = 0.32$ and $V_a = 8.5$.

respectively, were post processed to perform the purification/distillation protocol with various settings.

For a fixed threshold $Q = 1$ and a varying phase noise σ_ϕ we compared the conditioning on measurements of the originally squeezed (q_1) and anti-squeezed (p_1) quadratures. The results are shown Figure 4.6. Both the experimental data and the corresponding numerical simulations are shown. We could clearly see that the purification/distillation enhances the squeezing and $V_{\text{out}} < V_{\text{in}}$. We could say that the squeezing has been probabilistically concentrated from two noisy de-phased copies of the state into a single copy which thus exhibits higher squeezing. Remarkably, the conditioning on $|p_1| < Q$ not only enhances the squeezing of the quadrature q_2 , but for sufficiently weak phase noise it even leads to higher reduction of fluctuations of q_2 compared to conditioning on $|q_1| < Q$. This was surprising because naively one could expect that conditioning on $|p_1| < Q$ would rather reduce the fluctuations of quadrature p_2 and enhance fluctuations of q_2 . From a semi-classical point of view one could argue that small values of p_1 are detected by HDI with highest probability when the phase shifts ϕ_1 and ϕ_2 are of that kind, that the states impinging on BS_{PUR} are both squeezed in p quadratures. However, this picture is generally oversimplified. Some insight into why conditioning on $|p_1| < Q$ is helpful, can be achieved from the expression of the output variance, see Equation 2.46, which consists of two terms. The first term propor-

tional to B can be interpreted as corresponding to the probing of the channel. In case of measurement of the originally squeezed quadrature q_1 , the factor $\text{erf}(Q/\sqrt{2A})$ is maximized for zero random phase shifts. In this case B attains its minimum value $B = V_a$, so the conditioning acts as a filter that suppresses contributions corresponding to large unwanted random phase shifts. However, Equation 2.46 contains also a second negative term, proportional to C^2Q , that always reduces the variance V_{out} . This second distillation mechanism is of purely quantum nature since it is a consequence of the quantum correlations established by the interference of the two copies of the de-phased state on the purifying balanced beam splitter BS_{PUR} . In case of measurements of squeezed quadrature both above mechanisms contribute to the reduction of V_{out} . In contrast, for measurements of the anti-squeezed quadrature the first positive term increases the V_{out} since in this case the factor $\text{erf}(Q/\sqrt{2A})$ is maximized for phase shifts $\phi_1 = \phi_2 = \pi/2$, when B attains its maximum possible value V_a . Thus, in this case the variance V_{out} is reduced solely due to the second negative term. Remarkably, this quantum distillation mechanism is efficient enough to reduce the fluctuations of q_2 .

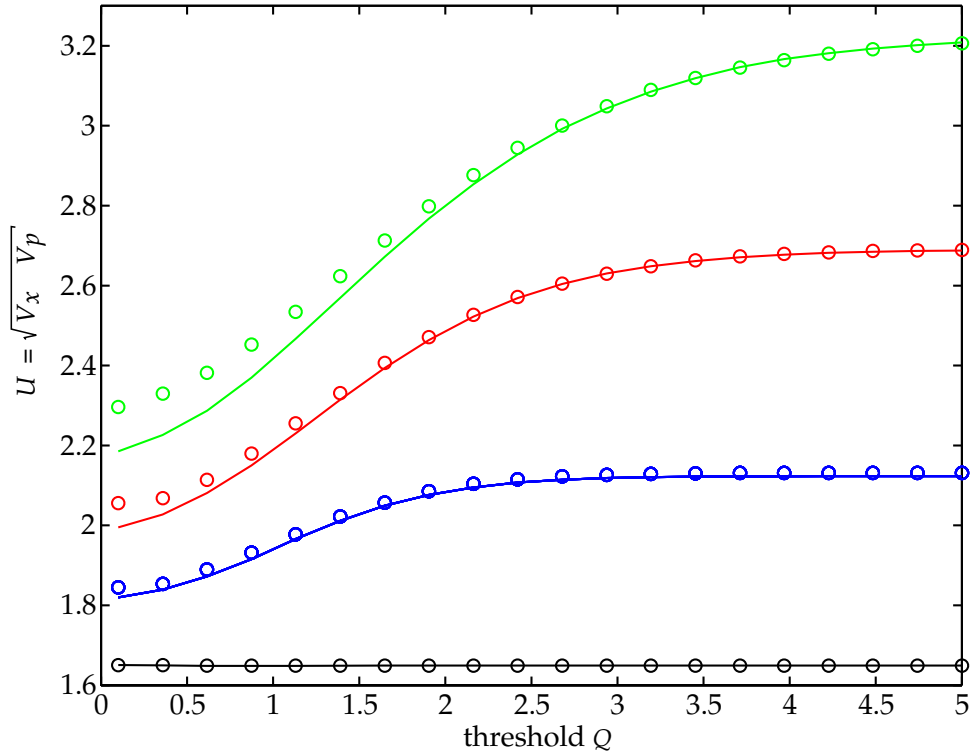


Figure 4.7 - Uncertainty product $U = \sqrt{V_q V_p}$ of the purified states for different phase noise levels ($\sigma_\phi = 0.40$ (green), $\sigma_\phi = 0.28$ (red), $\sigma_\phi = 0.17$ (blue) and $\sigma_\phi = 0$ (black)). Lines represent theoretical simulations while circles illustrate measurements.

So this conjugate purification/distillation is a purely quantum interference effect.

The purification actually reduces the variances of both conjugate quadratures q_2 and p_2 as witnessed by the decrease of the uncertainty product $U = \sqrt{V_{\text{out},q}V_{\text{out},p}}$, see Figure 4.7. The simultaneous suppression of the noise in both conjugate quadratures is a signature of the increase of purity of the state, which for Gaussian states can be evaluated as $P = 1/\sqrt{V_qV_p} = 1/U$.

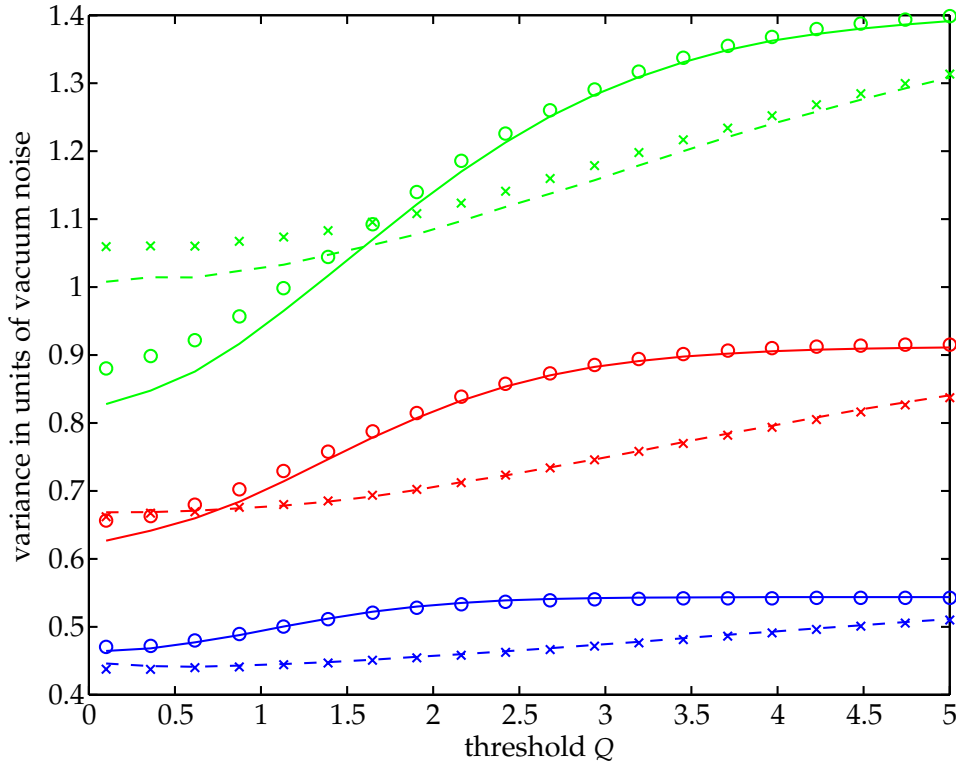


Figure 4.8 - Quadrature variances of distilled squeezed states V_{out} versus trigger threshold Q . V_{out} is plotted for three different levels of phase noise ($\sigma_\phi = 0.40$ (green), $\sigma_\phi = 0.28$ (red) and $\sigma_\phi = 0.17$ (blue)). The results are presented for conditioning on the (initially) squeezed quadrature q_1 (solid lines, circles) and for conditioning on the anti-squeezed quadrature p_1 (dashed lines, crosses). Lines represent numerical simulations while circles and crosses illustrate measurements.

In Figure 4.8 we presented the dependence of the variance V_{out} on the trigger threshold Q for three different strengths of phase fluctuations. As expected, the output variance decreased with a decreasing trigger threshold. In agreement with Figure 4.6 we saw again that for not too strong fluctuations the conditioning on p_1 is superior to conditioning on q_1 and yields a lower variance V_{out} . The probability of success \mathcal{P} monotonically increased with Q , but also depends on the choice of quadrature used for conditioning.

For further comparison we plotted in Figure 4.9 the trade-off between the output

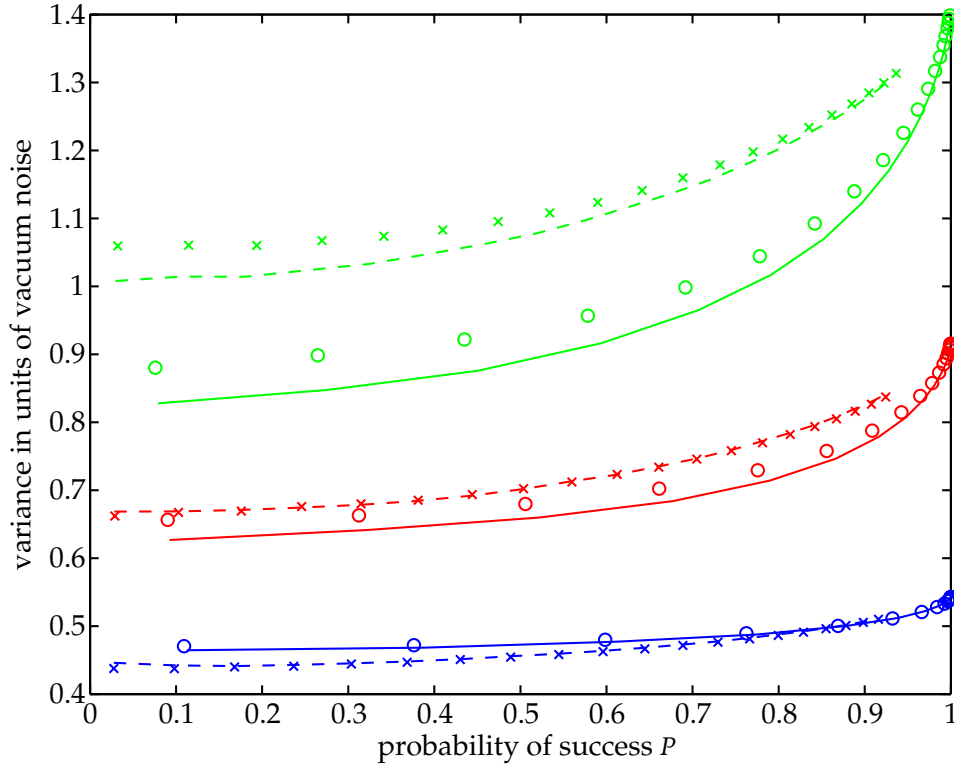


Figure 4.9 - Illustration of the same variance data as in Figure 4.8 – this time plotted over the fraction of distilled states. We refer to Figure 4.8 for the detailed description of parameters used. The graphs clearly show that for weak phase noise (bottom, blue) conditioning on the anti-squeezed quadrature is more efficient than conditioning on the squeezed quadrature. The opposite is found for strong phase fluctuations (top, green).

variance V_{out} and the success rate \mathcal{P} . We can see that we can achieve higher reduction of the noise at the expense of lower success rate \mathcal{P} . Also note that the achieved reduction of squeezed-quadrature variance is almost maximal already for \mathcal{P} of the order of 30%. A further lowering of the success probability results only in marginal improvement of the squeezing. This result is rather generic as confirmed by extensive numerical simulations. We can conclude that a single iteration of the purification/distillation procedure typically exhibits nearly optimum performance for a rather high success probability of several tens of percent. That is remarkable, for weak phase noise the conditioning on originally anti-squeezed quadrature p_1 yields for a given success rate \mathcal{P} a lower variance V_{out} than conditioning on the originally squeezed quadrature q_1 . For strong phase noise, however, it becomes preferential to condition on measurements of q_1 .

We also considered conditioning on measurements of arbitrary quadrature $q_{1\theta}$ and investigated the dependence of the performance of the purification/distillation protocol on θ . We found out that in fact, it does not matter too much, which quadrature $q_{1\theta}$

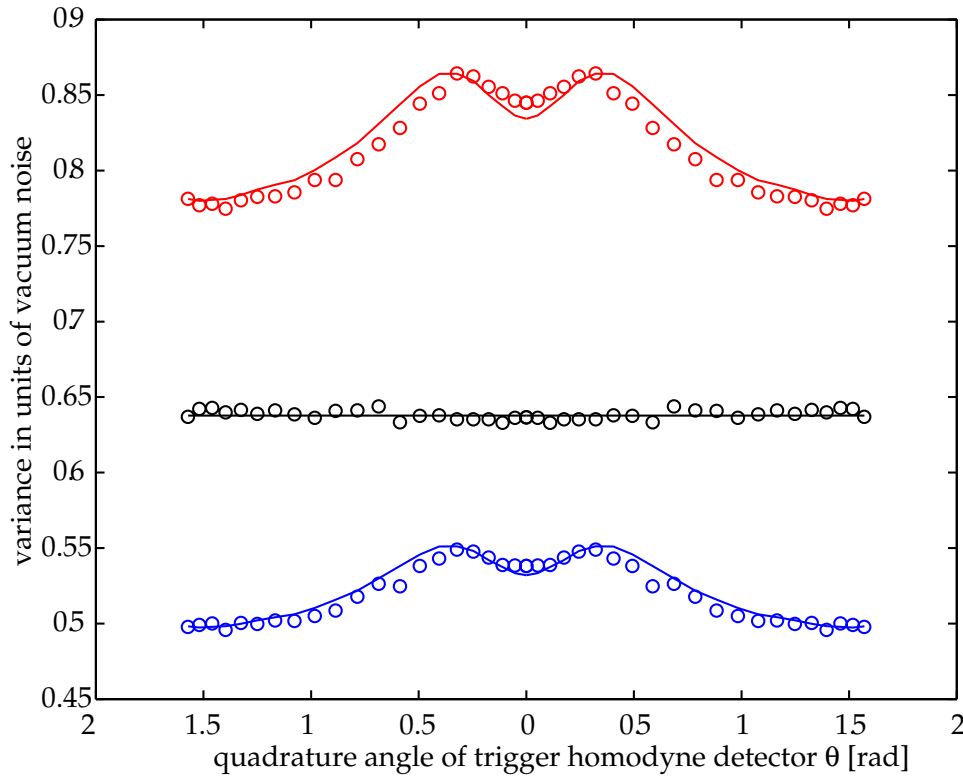


Figure 4.10 - Experimental and theoretical characterization of our distillation protocol for phase noise $\sigma = 0.202$ and trigger threshold $Q = 0.7$. Shown are variances versus the conditioning quadrature angle. The central (black) curve shows the variance of the dephased state's amplitude quadrature V_{in} . The lower (blue) curve shows the variance of the distilled state's amplitude quadrature V_{out} . For this particular parameter regime conditioning on the anti-squeezed quadrature works more efficiently than conditioning on the squeezed quadrature. However, the distillation protocol is successful for conditioning on *any* quadrature. The top (red) curve displays the purified variance V_{out} after normalizing to V_{in} (black curve).

is measured in the homodyne detector BHD I and the purification/distillation actually works well for all θ . Typical dependence of the squeezing of the purified state on θ is depicted in Figure 4.10. We can see that V_{out} exhibits a local minimum at $\theta = 0$, but the global minimum corresponding to the optimal purification/distillation strategy occurs in this case at $\theta = \pi/2$. Importantly, the quadrature fluctuations are suppressed and the squeezing is thus enhanced for any θ . This implies that the purification/distillation works even with phase-randomized homodyning, where the relative phase θ between balanced homodyne detector and signal is varied or randomly fluctuates in time. Interestingly, the phase-randomized homodyning very closely resembles the vacuum projection considered in [84, 85]. The effective Positive Operator Valued Measure

(POVM) element that describes this conditioning measurement reads:

$$\Pi_Q = \frac{1}{2\pi} \int_0^{2\pi} \int_{-Q}^Q |q; \theta\rangle \langle q; \theta| d\theta dq = \sum_{n=0}^{\infty} P_n |n\rangle \langle n|, \quad (4.4)$$

where $|q; \theta\rangle$ is the eigenstate of operator $q_{1\theta}$ with eigenvalue q and the probability for the photon number: $P_n = (\sqrt{\pi} 2^n n!)^{-1} \int_{-Q}^Q H_n^2(x) e^{-x^2} dx$, where $H_n(x)$ denotes the Hermite polynomial. Π_Q is diagonal in the Fock state basis because all off-diagonal terms vanish due to averaging over random phase shift θ . The dominant part of this POVM element is the term proportional to the projector onto vacuum state $|0\rangle$, but Π_Q also contains terms proportional to projectors onto higher Fock states $|n\rangle$. This POVM can be thus considered as an approximate noisy version of the ideal projection onto vacuum.

In conclusion we experimentally demonstrated that the state generated by our protocol showed a higher degree of squeezing compared to the input state indicating that we performed a distillation. We also showed that the variance was not only reduced for the squeezed quadrature but also for the anti-squeezed quadrature, which means that we also performed a purification. By the exploration of different detection quadratures for the trigger signal we revealed the true quantum nature of the protocol.

4.3 Distillation and Purification of Entangled States

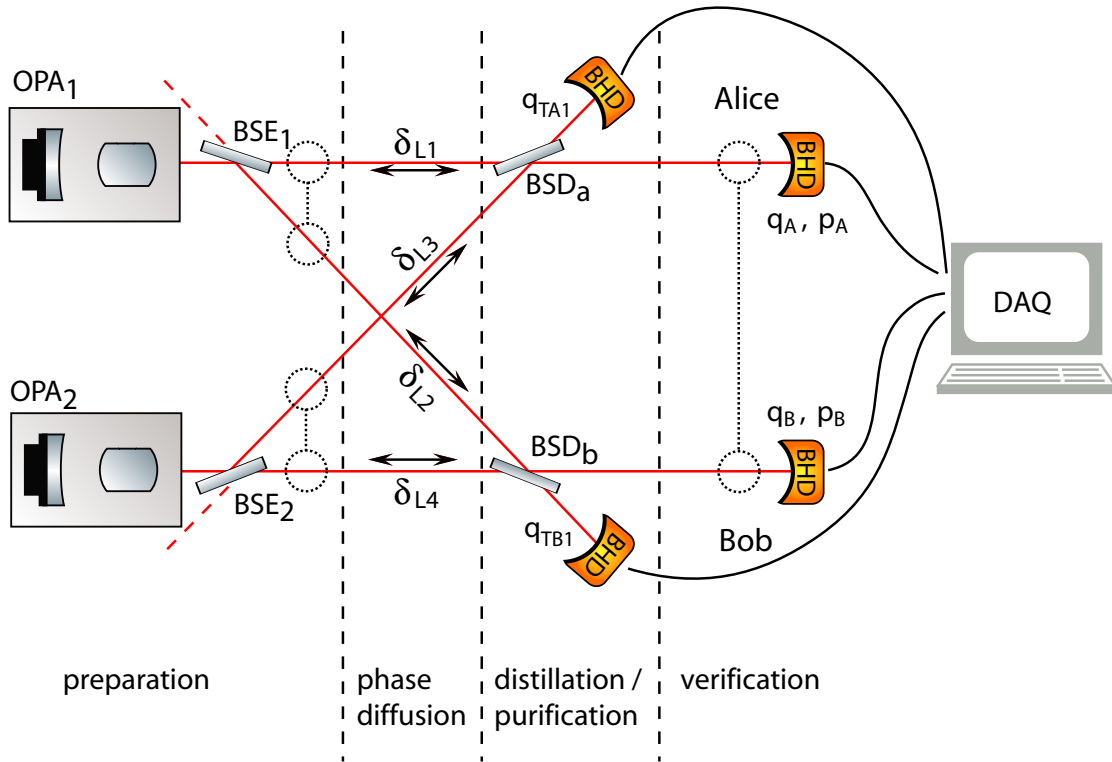


Figure 4.11 - Simplified setup for the demonstration of entanglement distillation and purification. $BSE_{1,2}$: beam splitter generating v -class entanglement. δ_L : mutually independent phase diffusion. $BSD_{a,b}$: distillation / purification beam splitter. BHD: balanced homodyne detector. DAQ: data acquisition system.

In this section we present the first experimental realization of a protocol for the distillation and purification of continuous variable entangled states. For a background description we refer to Section 2.2.7 and the work of J. Eisert et al. [85] and D. Browne et al. [84]. A theoretical description very close to our experiment is presented by J. Fiurášek [18].

A drastically simplified schematic sketch of the experimental setup is shown in Figure 4.11. We refer to Chapter 3 for the details of the individual components. Two optical parametric amplifiers (OPAs), see Section 3.2, provided two continuous wave light fields that carried amplitude squeezed states of light. The experimental parameters, such as the non-classical gain and the corresponding pump phase, were set equally. This ensured that both squeezed states had equal properties and could be considered to be copies. During the assembly phase of the experiment we could examine the squeezed states directly by sending them straight towards a balanced homodyne detector (BHD). The performance of the OPAs had turned out to be robust and reproducible for many days. However, the direct measurement was no longer possible once the first components of the subsequent beam splitter network were set up. From that stage on

we relied on the measurement of various linear combinations of the accessible beams. We did not find any temporal change of the parameters either.

As the first step of the subsequent setup each of the two squeezed modes was split up by a balanced beam splitter, $BSE_{a,b}$ in Figure 4.11. In the quantum world this meant that they were superimposed with the electro-magnetic vacuum field from the *open* port of the beam splitter, see Section 2.2.4. Each pair of output modes was then in a so-called *v-class* entangled state [39]. In general the entanglement from this class is rather weak compared to *s-class* entanglement, where instead of the vacuum a second squeezed field is sent onto the beam splitter with the squeezing ellipses orientated perpendicularly. However, this experiment did not aim on generating the strongest entanglement but rather on a proof of principle for our distillation protocol, which did not rely on the presence of strong entanglement. Hence, the *v-class* approach was preferable because of its experimental simplicity.

All four resulting beams of the two copies of the entangled pairs were transmitted to two parties Alice (A) and Bob (B) through four channels exhibiting independent phase noise. The noisy channels were realized by quasi-random electro-mechanical actuation of mirror positions in the beam paths in order to mimic the phase noise introduced for example in optical fibres. The phase fluctuations applied exhibited a vanishing mean value. This implied that the mean values of the phase of the field was not affected by the phase diffusion. In the following a reference to the phase of one of the phase-diffused fields is understood as the mean phase, unless noted differently. The distribution of the fluctuations was a Gaussian distribution, hence, the standard deviation of the noise σ_ϕ provided a complete characterization of its strength. See Section 3.6 for a detailed description. For the technical implementation we could benefit from the rich experience gained from the precursor experiment, see Section 4.2. The process of phase diffusion deteriorated the quantum properties of the underlying states, such as the non-local total variance or the purity, as shown in Figure 4.13 and Figure 4.16 for the points on the very right hand side. At the same time, the states were rendered non-Gaussian, which is described in Section 2.2.2 and Section 2.2.6. This finalized the preparation stage for the input states to the distillation protocol.

At the distillation stage, see Figure 4.11, Alice and Bob both superimposed their input states by means of a balanced beam splitter, BSD_a and BSD_b . The fringe visibility, see Equation 2.82, was 96.6% for Alice and 97.1% for Bob. The interference phase, $\delta\phi$ in Figure 4.12, was controlled in that way, that the quadratures of the input fields aligned in the output (with a phase flip in one of the outputs). An error signal for the control loop was derived according to Section B.1.2. Due to the way the OPAs were operated there was a phase modulation present on each of the beams. The power in the beam splitter output thus exhibited a corresponding beat signal containing the required information about the interference phase. This power was detected by the subsequent balanced homodyne detector (BHD). For each BHD the detector electronics generated not only the difference but also the sum signal of the individual detectors. The sum signal is equivalent to a simple power detection, as shown in Equation 2.79, and thus provides the required phase information after demodulation.

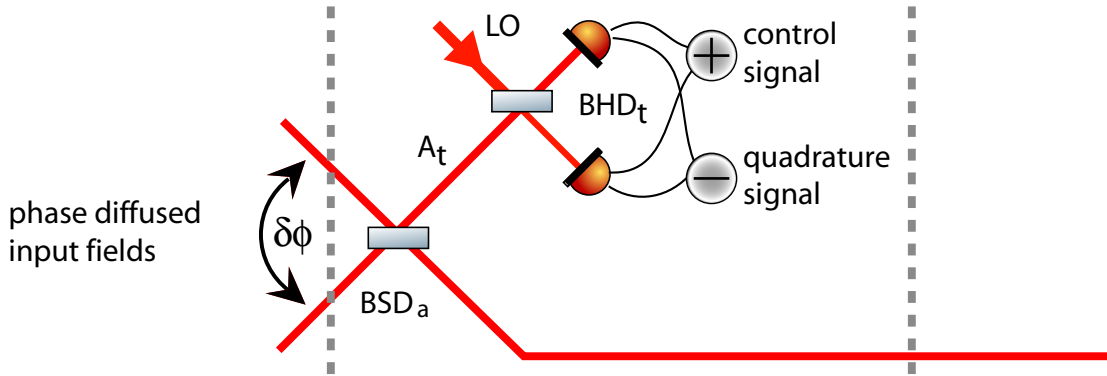


Figure 4.12 - Closer view of the distillation stage of Alice. The sum signal of the BHD was used to generate a control signal for the mean phase difference $\delta\phi$ of the two input fields. The difference signal of the BHD contains the quadrature information of A_t as well as the information about the detection phase.

The same BHDs were used for a quadrature detection, see Equation 2.78. The fringe visibility for the signal and the local oscillator beam was 97.3% for Alice and 97.1% for Bob. The local oscillators were filtered by a mode cleaner cavity as described in Section 3.1.1. This provided an excellent spatial mode as well as a shot noise limited power spectrum for frequencies above 2 MHz, see Figure 3.2. The detection phase of both BHDs was controlled for a detection of the amplitude quadrature. As shown in Section 2.2.5, the sum of the amplitude quadratures showed a quantum correlation according to the squeezing at the very beginning. The trigger condition for successful distillation was derived from these quadrature measurements: The trigger condition would be positive, if the absolute value of the sum of two amplitude measurements $q_T = q_{TA1} + q_{TB1}$ was found to be lower than a certain threshold value Q :

$$|q_T| < Q. \quad (4.5)$$

If this condition was true, the output state would be distilled.

In order to verify the performance of the procedure we also used balanced homodyne detectors for quadrature measurements of the output fields. They showed a fringe visibility of 97.8% for Alice and 98.0% for Bob. Note that the trigger and the verification BHD could swap their role in the setup. We simply chose those who provided a better visibility for the verification. The detection phases of all four BHDs were controlled by the second scheme presented in Section A.1. For the detection mode, see Section 2.74, we chose a frequency of 7 MHz. The bandwidth of this mode was 400 kHz. This was determined by the subsequent data acquisition system, see Section 3.5, which simultaneously sampled the signals delivered by the four BHDs. After the data were recorded, the post selection based on the trigger condition was carried out and the quantities describing the output state were calculated. The software program was based on the MatLab program.

In total, there were six beam splitters for which the incident light modes had to be

matched in order to obtain a good fringe visibility. For this purpose we chose a *lens saving* approach. Instead of placing mode-matching lenses in front of each beam splitter we only used three pairs of lenses. Two of which for the output beams of the two OPAs and one for the local oscillator. Each of the pairs was adjusted such, that the resulting modes exhibited the same waist size. A proper mode-matching was produced by placing each beam splitter such, that the distance to the waist position of the incident modes was equal.

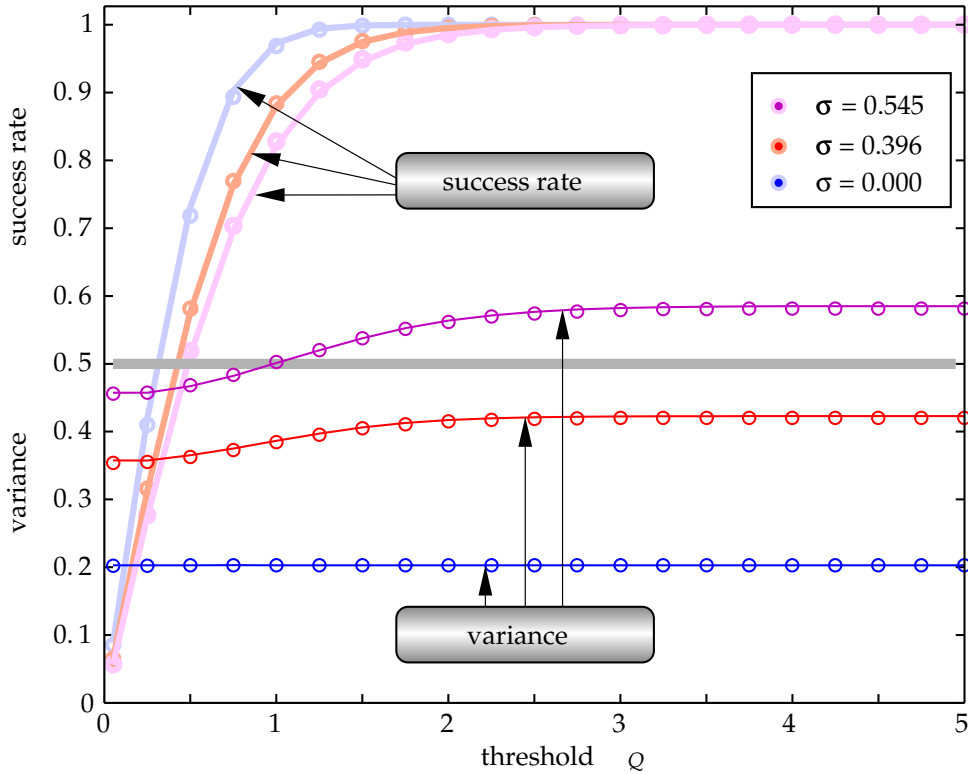


Figure 4.13 - Variance of the sum of the squeezed anti-correlated quadratures, and success rate for different strengths of the phase diffusion σ . The x-axis represents the trigger threshold value Q . For comparison, the grey line represents the value for the variance for a vacuum instead of a squeezed input to the experiment.

In the following presentation of the results we will let q_A and p_A denote the amplitude and phase quadrature of the output field on Alice's site. For Bob's part we will use q_B and p_B . The linear combinations are called $q_{\pm} = q_A \pm q_B$ and $p_{\pm} = p_A \pm p_B$. Because of the particular control scheme there was a phase difference of 180° between Alice's and Bob's detection phase. Hence the measurements of q_+ and p_- correspond to the non-local, EPR-like quadrature operators. We chose the normalization such that for the variances we obtained in case of a vacuum state $\Delta^2 q_{\pm}^{(0)} = 1/4$ and $\Delta^2 p(0)_{\pm} = 1/4$. In a first step we investigated the dependence of the non-local squeezing in $\Delta_{q_+}^2$, see the

points on the very right of Figure 4.13. Without any phase diffusion we found $\Delta_{q_+}^2 = 0.2$ which corresponds to -4 dB of squeezing compared to the variance for a vacuum. For increasing a phase noise strength we found $\Delta^2 q_+ > 1/4$ for $\sigma_p h i > 0.48$.

The figures presented here are based on five sets of data collected for different strengths of the phase diffusion, which is indicated in the legend of each figure. Each set consisted of four subsets, one for each of the combinations: q_A, q_B, p_A, p_B and p_A, q_B and p_A, p_B . Each of the subsets consisted of 100 000 samples of each of the four BHD signals. The *trigger* BHDs were tuned to amplitude quadrature detection for all cases.

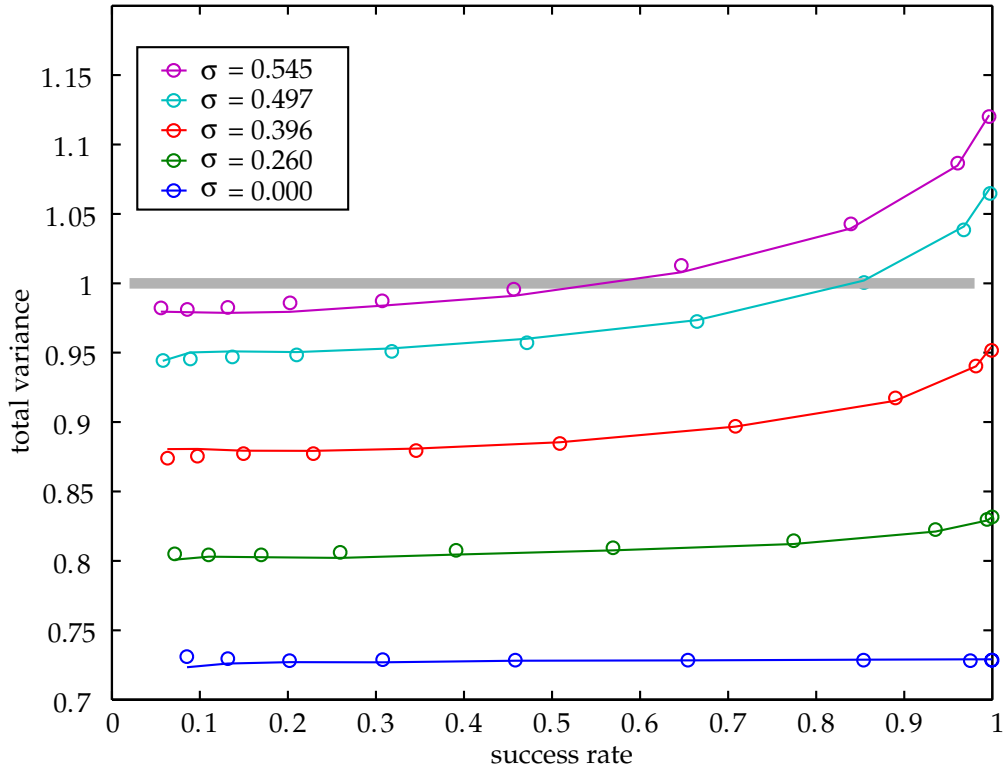


Figure 4.14 - The total variance I for different phase diffusion strengths σ . The x-axis represents the success rate of the protocol. The grey line represents the separability boundary. For a success rate as high as 0.5 the protocol already distilled very efficiently and nearly deployed its full potential.

Figure 4.13 shows the effect of the distillation protocol on the variance of q_+ and corresponding probability of success versus the threshold value Q . The lower the value of Q was set the more selective the protocol worked. This resulted in a decrease of the probability of success and in an improvement of the variance of q_+ . At the same time the variance of p_- decreased slightly, too. Due to the choice of *v-class* entanglement the variance of p_- did not show any non-classical variance. We omit a direct presentation. The results still become evident by looking at the *total variance*: $I = \Delta^2 q_+ \Delta^2 p_-$, see Section 2.2.5. The total variance quantifies the quantum correlations between the two

output modes and the degree of inseparability of the two mode state in the second moment. If $I < 1$, then the state will be entangled.

The improvement of the total variance by distillation is shown in Figure 4.14 versus the probability of success. For the two strongest levels of phase noise the total variance did not show any non-classical behavior without distillation. By applying the distillation protocol we saw that the total variance decreased for all phase-diffused states. For the strongest phase noise settings, too, entanglement was detected by the total variance for a probability of success, which was as high as 0.4. Thus, the protocol worked very efficiently even for high success rates.

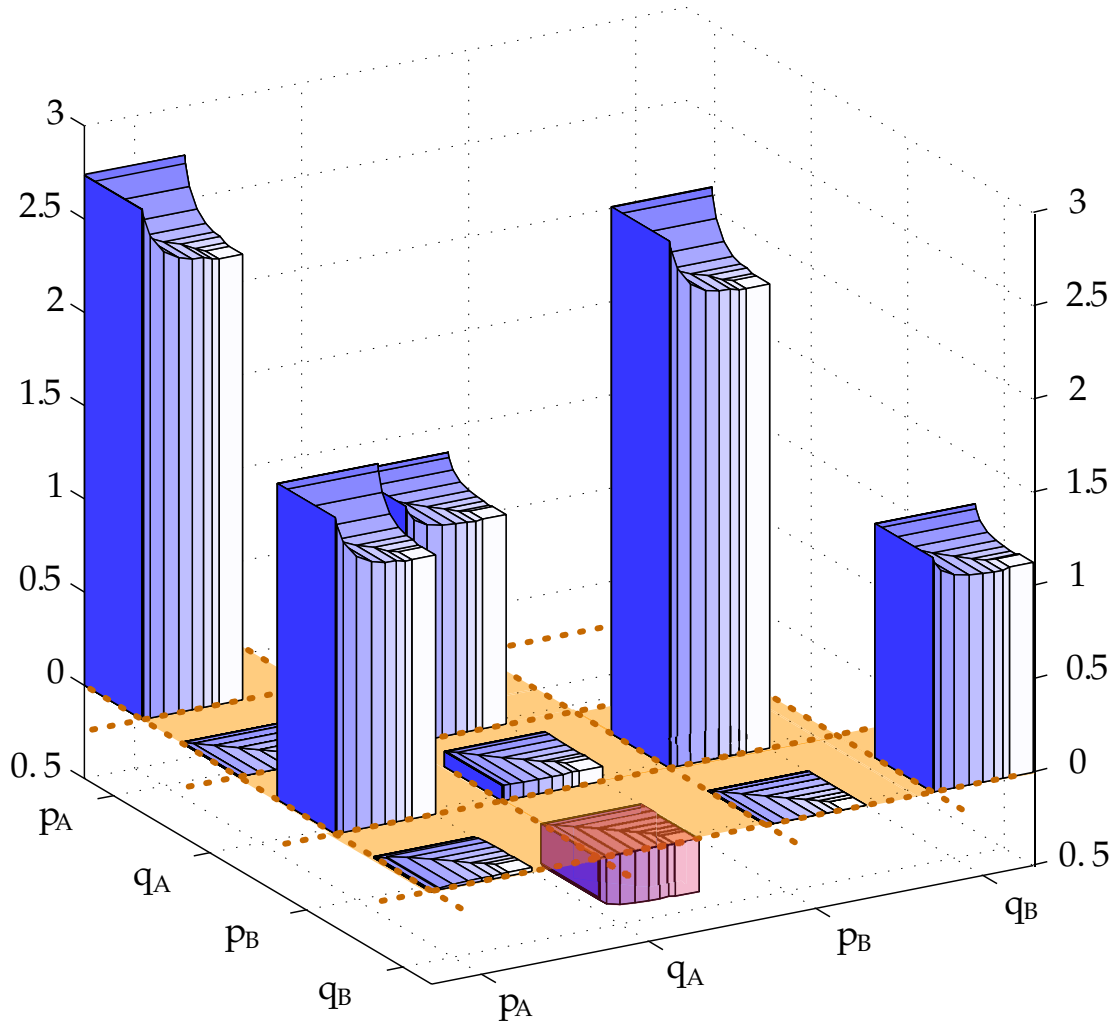


Figure 4.15 - Covariance matrix for Alice's and Bob's quadratures $q_{a,b}$ and $p_{a,b}$. The sub-columns represent the result of the distillation for the different threshold values. The base area of each column is proportional to the success rate. All individual variances on the diagonal decreased simultaneously under distillation. Most remarkably, at the same time the correlation between the amplitude quadratures increased (the negative column).

As stated before we measured all quadrature combinations q_A, q_B, p_A, p_B and p_A, p_B . This enables us to reconstruct the most significant eight of ten independent components of the covariance matrix γ of the distilled output state. The missing components were the intra-modal correlation of the local modes of Alice and Bob, i.e. the correlation of q_A, p_A and q_B, p_B . However, it is reasonable to assume that there is no correlation for two reasons. First, the detected quadratures are the same as the quadratures of the initial squeezing, for which there is no correlation. Second, the distribution of the phase diffusion was symmetric around zero, i.e. there was no mean phase shift introduced by the phase diffusion.

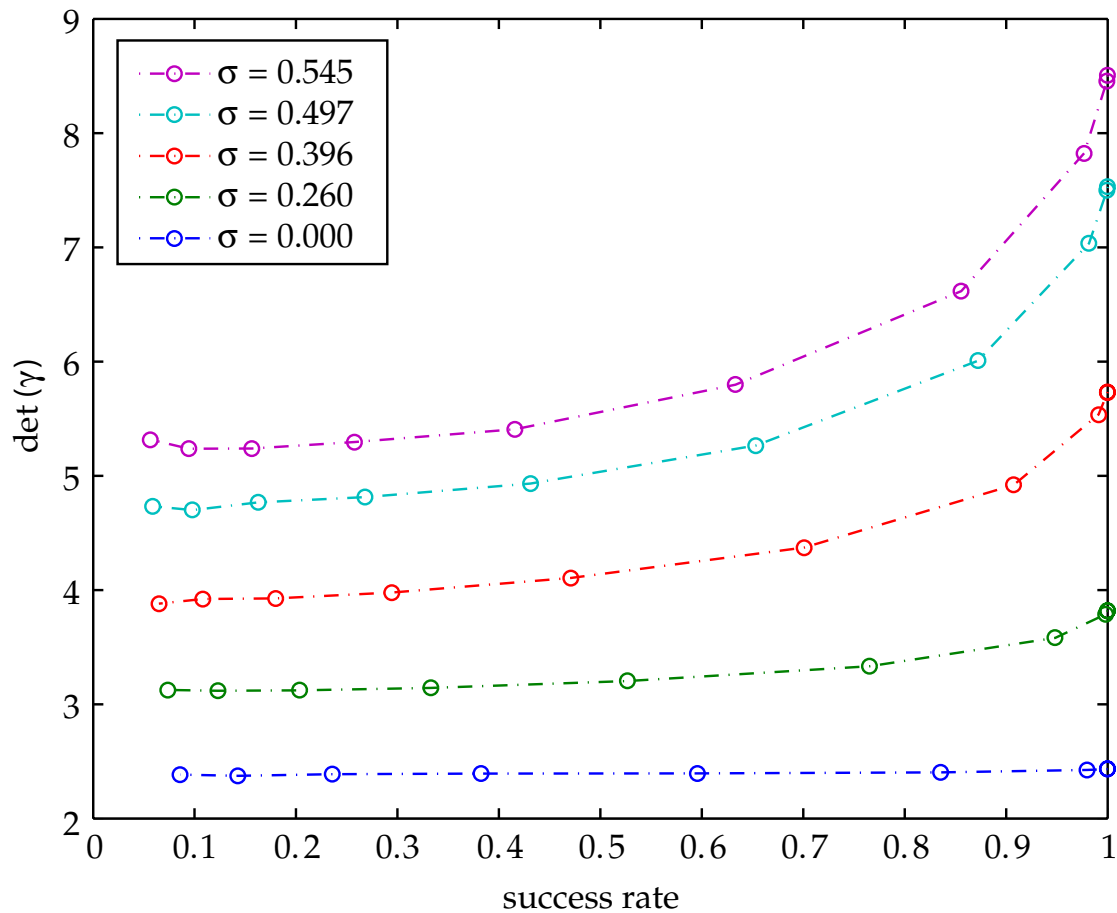


Figure 4.16 - Purity of the final state estimated by the determinant of the covariance matrix. Simultaneously to the increase of entanglement the purity of the state after distillation also increased.

The reconstructed covariance matrix for a phase noise strength of $\sigma_\phi = 0.497$ is shown in Figure 4.15 for ten different threshold values represented by the sub-columns. The base area of each sub-column represents the corresponding probability of success. The individual quadrature variances on the main diagonal simultaneously decrease the stronger the distillation was. At the same time the anti-correlation between the amplitude quadratures became stronger (the reddish column in Figure 4.15). Consequently

the squeezing of the non-local quadrature q_+ was enhanced.

From the reconstructed covariance matrices we calculated their determinant $D = \det(\gamma)$. For a Gaussian state the purity of the state is given by $\mu = 1/\sqrt{D}$, see Section 4.7. In Figure 4.16 the dependence of D on the distillation is shown versus the probability of success. The value of D decreased the stronger the distillation was. This is a strong indicator for increase of the purity of the still non-Gaussian state after distillation.

The experimental results demonstrate the ability of our protocol to prepare an entangled state from a supply of two copies of less entangled states. At the same time the protocol provides a higher purity of the output state compared with the input. The output state is available for an arbitrary downstream application, including a subsequent distillation stage, see the next section. To the best of our knowledge this was the first demonstration [86] of a protocol providing all of the features required for entanglement distillation in the continuous variable regime [13, 14, 85]. The results appeared back-to-back with the work of R. Dong, et.al. [87] in the very same issue of Nature Physics. The authors also report on continuous variable entanglement distillation, which was based on a single input copy and a local conditioning based on one of the input modes.

4.4 Iterative Distillation and Purification of Entanglement

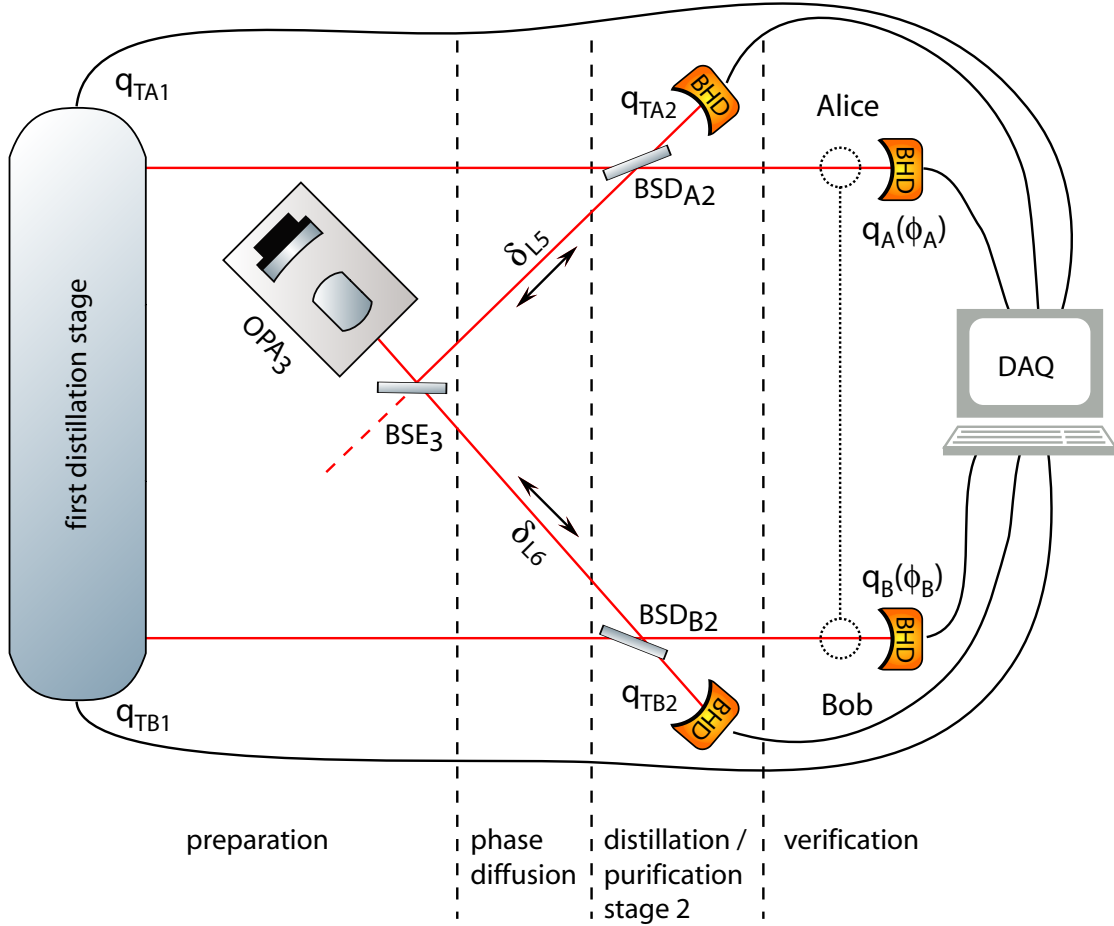


Figure 4.17 - Simplified sketch of the experiment. The first distillation stage was the complete setup from the previous section except for the verification homodyne detectors. A third copy of the entangled input states, was produced by OPA₃ and the subsequent beam splitter BSE₃. The two corresponding fields were phase-diffused, too. The two already distilled output modes of the first state and the newly prepared phase-diffused pair of modes formed the input of the second distillation stage. The output of the second stage ($q_A(\phi_A)$ and $q_B(\phi_B)$) was investigated by means of a full two mode quantum state tomography. The signals (q_{TA1} , q_{TA2} , q_{TB1} , q_{TB2}) of the four *trigger* detectors were simultaneously recorded by the data acquisition system (DAQ), together with the tomography data.

In this section the experimental demonstration of an iterative entanglement distillation scheme is presented.

This experiment consisted of two subsequent distillation stages as described in the previous section, where a detailed description can be found. The output of the first stage, which provided the distilled entanglement, was used as one input pair of modes for the second subsequent stage, see Figure 4.4. The second entangled pair of input modes was provided by a third copy of the two input pairs of the first stage. For the

description of the preparation of the third copy, including the phase diffusion, we also refer to the previous section.

The major difference between the first and the second distillation stage was the choice of the reflectivity of the beam splitter for the superposition of the input modes (BSD_{A2} and BSD_{B2}). Numerical simulations showed that a power splitting ratio of 1:2 was optimal for the second stage. The bigger fraction of the beams from the first distillation stage was transmitted to the output. The smaller fraction was used for the trigger generation, and vice versa for the undistilled input. In total, there were six BHDs: two in the first distillation stage and two in the second stage for the trigger generation. Another two detectors were used to verify the output of the iterative scheme. All six detector signals were simultaneously sampled, see Section 3.5.

The BHDs for the generation of the trigger condition for the success of distillation were tuned to amplitude quadrature detection as it is the case the first stage, too. A positive trigger condition in the first stage would be obtained, if the absolute value of the sum of the two trigger BHDs $q_{T1} = q_{TA1} + q_{TB1}$ were lower than a certain threshold value Q_1 :

$$|q_{T1}| < Q_1. \quad (4.6)$$

The trigger condition for the second stage was equivalently based on $q_{T2} = q_{TA2} + q_{TB2}$

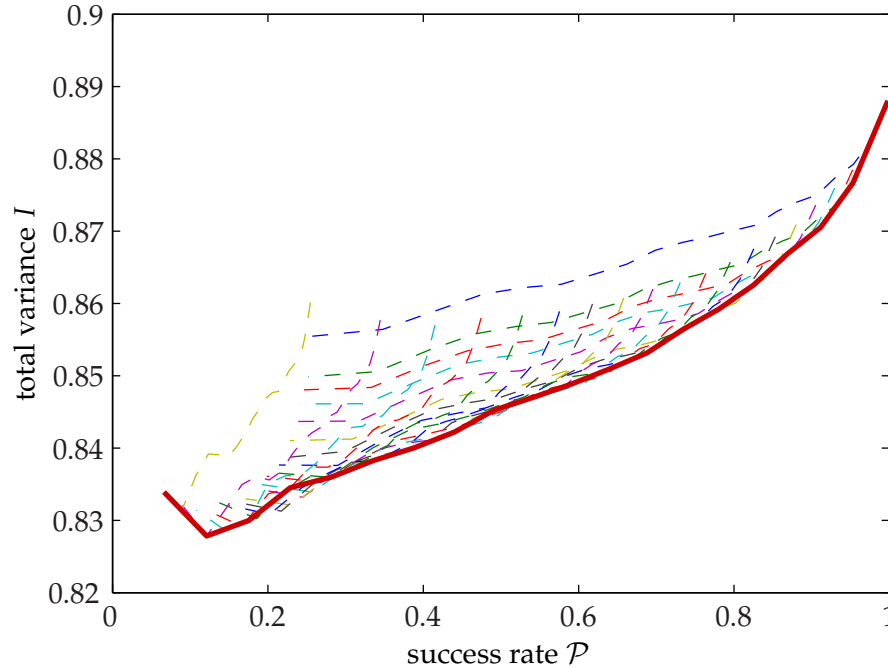


Figure 4.18 - The total variance I after distillation versus the probability of success \mathcal{P} for various values of the trigger threshold Q_1 and Q_2 . Each dashed line was obtained by keeping one of the threshold values fixed while varying the other. The thick red line was obtained for equal values of Q_1 and Q_2 . The distillation worked most efficiently for equal values.

and the threshold value Q_2 . In combination the protocol would only be successful, if both conditions were positive at the same time:

$$(|q_{T1}| < Q_1) \text{ AND } (|q_{T2}| < Q_2). \quad (4.7)$$

We investigated the dependence of the distillation performance on the choice of values for Q_1 and Q_2 . In order to quantify the performance we used the total variance I , which represents the non-local correlation between the two output modes in the second moment, see Section 4.11 and Section 2.2.5. In Figure 4.18 we show the resulting total variance I versus the success rate for various combinations of Q_1 and Q_2 . The best result for a certain success rate was obtained for equal values. This was also true for all the other quantities which we will introduce later in this section. Hence, we always chose equal values.

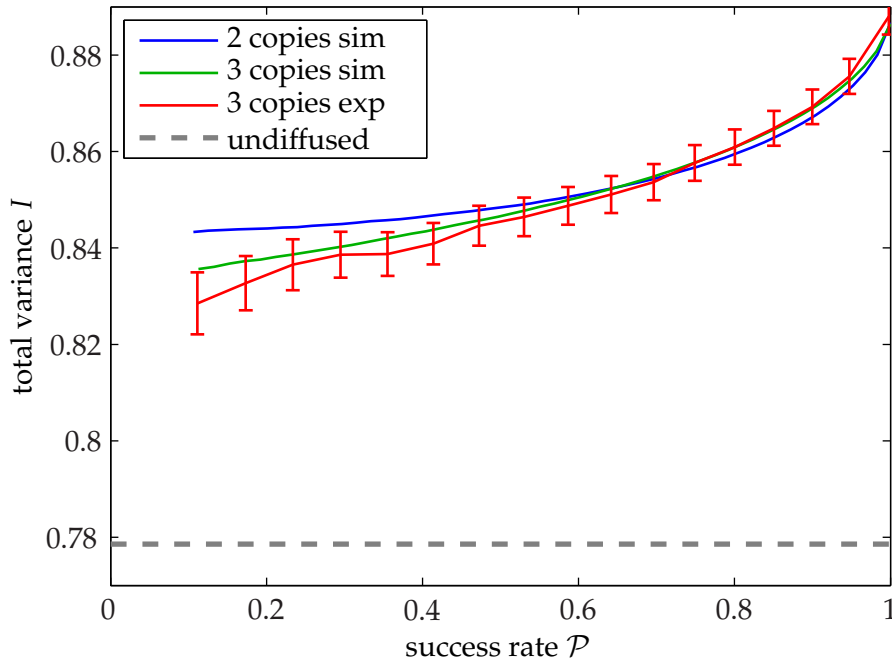


Figure 4.19 - The total variance I from the iterative experiment (3 copies exp) and a numerical simulation according to the experimental parameters (3 copies sim) versus the probability of success \mathcal{P} . For a comparison to the distillation based on two copies a numerical simulation is shown (2 copies sim). The total variance of the initial state prior to the phase diffusion is also shown (undiffused). The numerical simulations indicate that the iterative protocol outperforms the single step version for lower success rates.

In the last section we used quantities based on the covariance matrix to characterize the output state after distillation. As a first step we used the same approach also for the iterative setup in terms of the total variance I , see Figure 4.19. The comparison to the simulation indicated, that the iterative scheme provided a better performance than the single step version could have done for strong purification, i.e. for a success rate $\mathcal{P} < 0.4$ the measured total variance was below the single step simulation including

the error bars.

For a comparison of the iterative and the single step procedure we had to rely on numerical simulations because the output of the first stage was sent into the second stage. Thus, it was no longer available for a direct measurement. As it was shown here and in the last section the simulations reliably reproduced the experimental results. The increased number of components required for this setup inevitably led to additional loss of 0.2% and a slightly lower overall efficiency. The simulations took this into account. Apart from this issue the simulations were run with parameters equal to experiment. We inferred an initial squeezing of -8.5 dB and an overall efficiency of 70.5% from the measured variances. The phase diffusion standard deviation was $\sigma_\phi=0.302$ rad. The simulation was also based on the same number of quadrature samples. In order to reduce the statistical fluctuations for the curves shown in this section we performed an averaging over 1 000 individual simulations. The corresponding error bars were too small to be shown in the figures. The error bars, which are shown for the experimental data in the figures, were derived from the standard deviation of all simulations. This was reasonable as the experimental errors were dominated by statistic. The vast effort of number crunching was carried out on the computer cluster ATLAS, which was run by our institute.

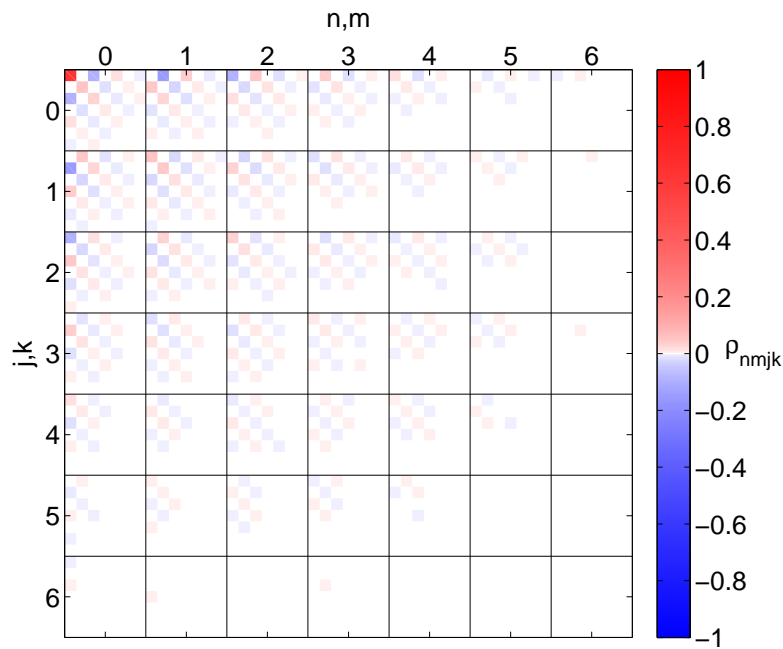


Figure 4.20 - Fock base density matrix ρ_{nmjk} reconstructed from a full two mode quantum state tomography. The large blocks count Alice's photon number, the subdivisions count Bob's. The matrix elements decayed rapidly for larger photon number. Thus, it was safe to truncate the reconstruction for $n \geq 5$.

Despite being the most relevant property for down stream protocols based on correlations in the second moment, in a strict sense these quantities could only fully describe

Gaussian states. However, the states we worked with had to be - and also were - non-Gaussian to a certain extent. In order to obtain the full information about the quantum state of the output we therefore performed a full and unbiased two mode quantum state tomography, see Section 2.3.2. For this purpose the joint probability distributions had to be measured for many different combination of quadrature detection phases $q_A(\phi_A)$ and $q_B(\phi_B)$ of the two output modes. A statistically significant estimate for the joint probability distributions was obtained by recording many samples of the BHD signals for each combination of detection phases, which required an active controlling. The control scheme of ϕ_A and ϕ_B for this purpose is described in Section 3.4. With this control scheme and the accompanying automated data acquisition management system, we were able to record data for ten different detection phases per BHD, which resulted in 100 combinations. For each combination we took 300 000 samples of the two output mode quadrature signals and simultaneously of the four trigger signals. As a representation of the quantum state of the output we chose the Fock base density matrix: $\rho_{nmjk} = \langle n|_A \langle m|_B \hat{\rho} |k\rangle_B |j\rangle_A$, of the two mode state $\hat{\rho}$. The reconstruction procedure is described in Section 2.3.2.

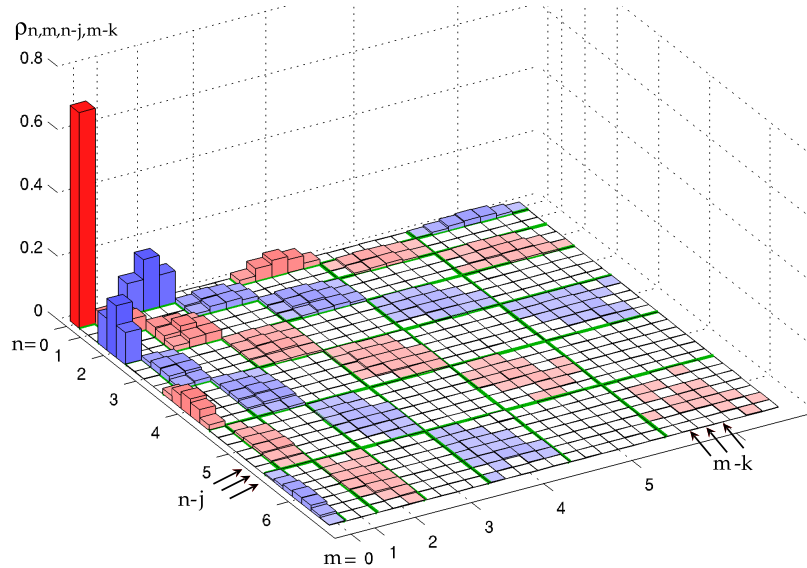


Figure 4.21 - Absolute values of the reconstructed density matrix with the sign indicated by the color of each column. The ordering of the matrix elements is such that for each block the total photon number is fixed: $\langle n|_A \langle m|_B \hat{\rho} |m-k\rangle_B |n-j\rangle_A$.

Figure 4.20 shows an example of the reconstructed density matrix. The matrix elements were organized such, that the big blocks accounted for Alice's photon number. Each block represented Bob's part of the density matrix for the photon number of Alice's part determined by the position of the block. Note that for separable systems the big blocks would differ by a factor, which is constant for all elements within the block. Obviously this was not the case here. The matrix elements were found to decay very rapidly for an increasing photon number. Thus, we truncated the reconstruction for photon numbers exceeding 5. Roughly speaking the decay was determined by the sum

of photons, which was somewhat intuitive as they emerged from a common source. In anticipation of this structure the density matrix elements were reorganized in Figure 4.21. Here the elements were organized such, that the blocks, separated by the green lines, represent a fixed sum of photon numbers.

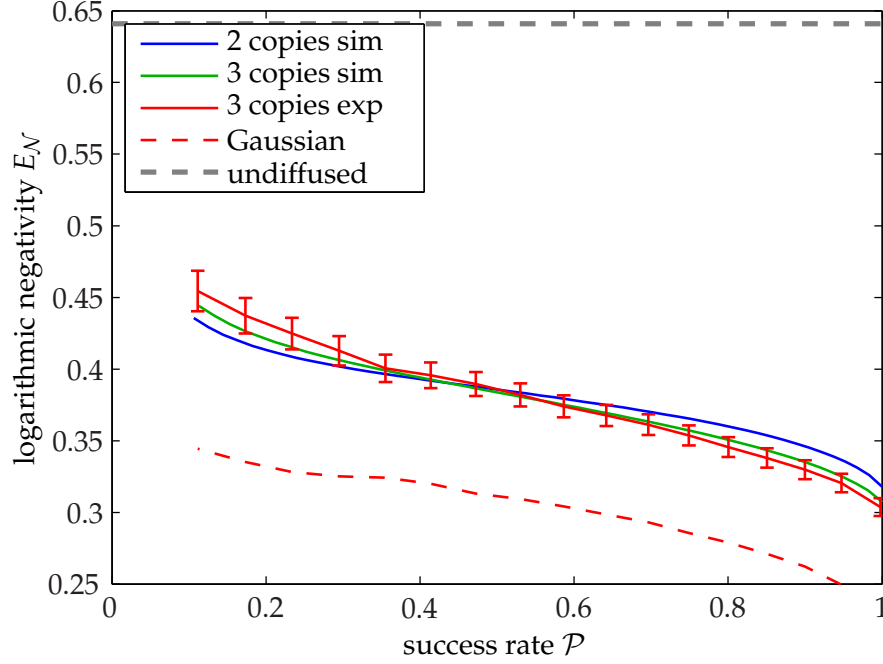


Figure 4.22 - Logarithmic negativity $E_{\mathcal{N}} = \|\rho_r^{T_A}(\mathcal{P})\|_1$ of the distilled state (3 copies exp) versus the probability of success based on the tomographically reconstructed density matrices $\rho_r(\mathcal{P})$. For comparison we show numerical simulations for the parameters of the experimental data for the iterative scheme (3 copies sim) and the single step distillation (2 copies sim). We also show the logarithmic negativity of the initial state prior to phase diffusion (undiffused). The logarithmic negativity represents an entanglement measure. Unlike the total variance it is not restricted to Gaussian states. This fully quantified the performance of the distillation. The logarithmic negativity under the assumption of the state being Gaussian was significantly lower (Gaussian). The simulation indicated that the iterative scheme produced a stronger entanglement than the single step version.

We reconstructed the density matrix for various strength of distillation, i.e. for various values of the common threshold Q . For the following figures we used the corresponding probability of success for the abscissa. Based on the density matrices we calculated the logarithmic negativity $E_{\mathcal{N}}$, see Section 2.2.4. This quantity measures the strength of the entanglement without a restriction to the Gaussian regime. The results are shown in Figure 4.22. The process of distillation increased the logarithmic negativity. This demonstrated that the distillation truly increased the entanglement. We applied the same reconstruction procedure on the simulated data for both the single step and the iterative setup. Again, we calculated the corresponding logarithmic negativity. The numerically simulated data for the iterative scheme were in excellent agreement with the experimental data. Thus, we also confided in the single step simulation, which shows that the iterative scheme was able to distill more entanglement for a sufficiently

low success rate.

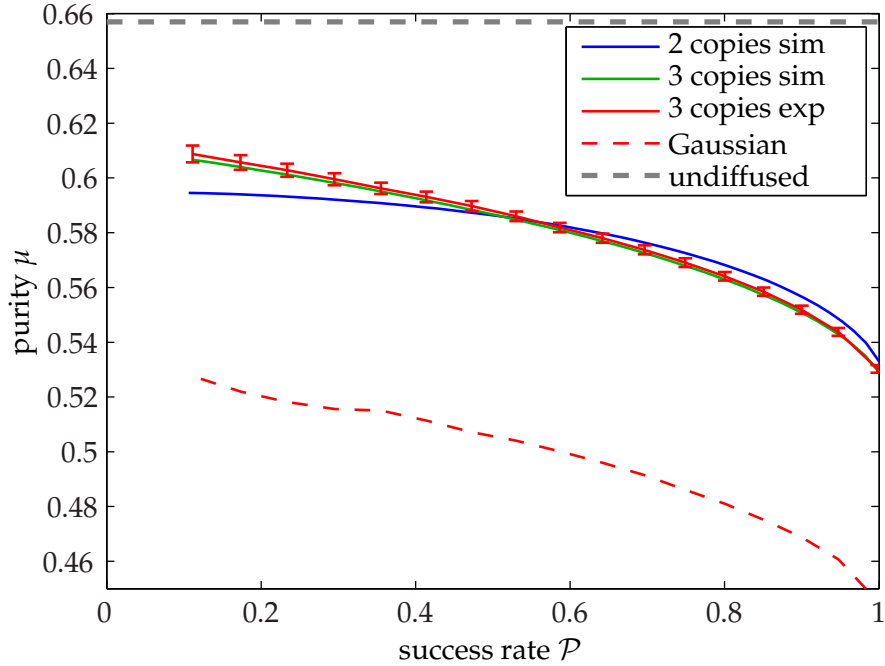


Figure 4.23 - Purity $\mu = \text{tr}(\rho_r(\mathcal{P})^2)$ after iterative distillation (3 copies exp) versus the probability of success \mathcal{P} . based on the tomographically reconstructed density matrices $\rho_r(\mathcal{P})$. For comparison we show numerical simulations for the parameters of the experimental data for the iterative scheme (3 copies sim) and the single step distillation (2 copies sim). We also show the purity of the initial state prior to phase diffusion (undiffused). Under the assumption of the state being Gaussian the purity was significantly underestimated (Gaussian). The iterative scheme produced a state of higher purity compared to the single step version simulation.

We also calculated the purity μ of the distilled states based on the reconstructed density matrices, see Section 4.7. The purity quantified the mixedness of the distilled states. The results for the experimental data and the corresponding simulations are shown in Figure 4.23. For this quantity, too, we found the iterative scheme yield a higher maximum purity than the single step simulation. Furthermore, the sum of the squared deviation between the measured probability distributions and Gaussian fits decrease by 40% after distillation. In this sense the output states were more Gaussian.

These results demonstrate that our apparatus indeed prepared distilled and purified entangled states in an iterative scheme. These quantities were determined in a completely unbiased way by means of a full two mode quantum state tomography. To our best knowledge this experiment was the first demonstration of the iterative application of a distillation protocol. It also was the first time, that a full unbiased two mode quantum state tomography was implemented to characterize the prepared states.

Discussion and Conclusion

The first protocols in the field of quantum information, such as teleportation [88] or quantum key distribution [89] were formulated for the regime of discrete variables, i.e. the photon counting regime. Soon after their publication these protocols were translated to the complementary continuous variable regime [90, 91, 92, 93], which has several advantages: The measurement tools such as balanced homodyne detectors show a detection efficiency close to unity. Entangled states can be prepared efficiently, e.g. using squeezed states and linear optics. Related to the high efficiency is the valuable feature of *unconditionalness*. A squeezed light source for example always emits squeezing once per inverse bandwidth. Entangled states based on squeezing show the same property. In the discrete-variable regime unconditionalness is not easy to achieve because of the poor quantum efficiencies of single photon detectors or photon counters. Typical experiments in this regime rely on coincidence measurements with two or more single photon detectors. Only in case of a coincidence a state is prepared, which automatically cancels out the unwanted contributions to the prepared state, e.g. from the vacuum state. For the same reason the unconditional preparation in case of continuous variables comes at the cost of the quality of the generated states. A measurement is bound to averaging over the time period the experiment lasts, because there is no *click*-event indicating the right instant of time for the measurement. Entanglement generated this way is always imperfect. The degree of imperfection is determined by the amount of initial squeezing, for which already more than 10 dB (measured directly) of squeezing was demonstrated [94]. Laxly summarized: On the one hand, continuous variable experiments can work well, efficiently and unconditionally, but never perfect. On the other hand, discrete-variable approaches only sometimes work, but then they do almost perfectly. The same arguments are applicable, when the distribution of quantum states, e.g. through optical fibres, is considered. Continuous variable states aggregate the inevitable noise during the transmission and leave the transmission-line in a degraded state.

In order to counteract the degradation of entanglement imposed by decoherence general strategies for the distillation of entanglement were developed [13, 14, 16]. Such

protocols transform a certain number of copies of previously shared less entangled pairs into a smaller number of in principal maximally entangled pairs. However, at this point another drawback of the continuous variable regime was found: It is impossible to distill Gaussian states by means of Gaussian operations [16, 95, 17]. A state is Gaussian, if it exhibits a Gaussian distribution for the probability distributions of the corresponding variables. The kind of entanglement based on squeezed states, i.e. the kind that can easily be prepared, is Gaussian. Gaussian operations are those, which preserve the Gaussianity of a state. The class of operations exhibiting an advantageous efficiency preserve the Gaussianity. This means, that for a distillation within this frame either a non-Gaussian operation, such as single photon counting, or a non-Gaussian state is required.

In this work we successfully demonstrated the experimental feasibility and functionality of a protocol for the simultaneous distillation, purification and Gaussification of non-Gaussian entangled states. The underlying de-Gaussification was based on the phase diffusion of Gaussian entangled states. This process realistically mimicked the phase fluctuations occurring during the transmission through an optical fibre network. In this frame phase fluctuation can happen due to temporal variations of the index of refraction caused, e.g. by mechanical motion of the environment. Also non-linear processes inherent to optical fibres are covered, like the optical Kerr-effect, which causes intensity fluctuations of the transmitted light affecting the optical phase. In contrast to previous demonstrations of entanglement distillation in the complementary discrete-variable regime [96], [97], our scheme [18] achieved the actual preparation of the distilled state. Thus, it is suitable for an arbitrary downstream application such as the Braunstein-Kimble teleportation [4].

However, the dominant decoherence process, which causes the entanglement to deteriorate, is displayed by generic loss, i.e. the random annihilation of photons. This effect preserves the Gaussianity of the state and thus cannot be counteracted solely by our protocol. In order to also address this effect our protocol can be combined with a single intentional de-Gaussification step. Some schemes were recently demonstrated [98, 99, 100], e.g. by single photon subtraction. This combination would provide a generic entanglement distillation scheme.

We also demonstrated the iterative applicability of the protocol. The experimental evidence was gained from a full unbiased two-mode quantum state tomography. This enabled us to quantify the performance of our setup in terms of the logarithmic negativity and the purity without a priori assumptions about the state. In summary this makes our scheme a suitable building block for a quantum repeater. Combined with already demonstrated quantum memory [8] and entanglement swapping [5, 6] our experiment may display an important enabling step for truly long-distance quantum communication networks.

Hardware

A.1 Homodyne Locking Scheme

In an ordinary squeezing setup the balanced homodyne detector (BHD) is tuned to the squeezed quadrature, which usually is the amplitude quadrature with respect to the fundamental carrier $E_s = E_s^0 e^{i(\omega t) + \phi}$ of the squeezed beam. From Section 3.3 we know, that this corresponds to a mutual phase ϕ of local oscillator $E_{LO}^0 = E_{LO} e^{i\omega t}$ and signal beam of $\phi = 0$. We follow the argumentation of Section 3.3 for the fundamental carrier on the signal beam only and find for the BHD signal X_D :

$$\begin{aligned} X_D(\phi) &= g E_s^0 E_{LO}^0 \cos \phi \\ &=: X_D^0 \cos \phi, \end{aligned} \tag{A.1}$$

with E_s^0 and E_{LO}^0 chosen to be real. The overall electronic transimpedance and gain factor is denoted g . This expression is linear in ϕ for small deviations from $\phi = 90^\circ$. Thus it is suitable to build a control loop which actuates on ϕ for the set point $\phi_p = 90^\circ$, i.e. the detection of the phase quadrature.

Typically there is a radio frequency phase modulation on the squeezed field. We can obtain the derivative of $X_D(\phi)$ with respect to ϕ by demodulating $X_D(\phi)$ with the frequency of the phase modulation, see Section B.1.2:

$$X_{dm}(\phi) = X_{dm}^0 \sin \phi. \tag{A.2}$$

This expression is linear in ϕ in proximity of $\phi = 0^\circ$ and thus can serve as an error signal for a control loop for detection of the amplitude quadrature with $\phi_q = 0^\circ$.

In a tomography scenario this is not sufficient. An error signal for an arbitrary phase is necessary. In a certain diploma thesis ([101]) the above two signals were used to construct such a signal:

$$X_{lc} = a X_{dm} + b X_D. \tag{A.3}$$

By choosing the right coefficients a, b of the linear combination of the two signals the phase ϕ_s of the set point $X_{lc} = 0$ can be chosen:

$$\phi_s = \pm \arccos \left(\frac{a}{\sqrt{a^2 + b^2}} \right). \quad (\text{A.4})$$

Of course this necessitates that both amplitudes are carefully matched in the first place. However, unless the set phase is not 0° or 90° , fluctuations of the amplitude of each signal couple into the signal for set phase. Inevitable offset voltages on the signals are a problem as well and have to be cancelled thoroughly.

The single side band modulation technique overcomes all of these problems. The author proposed to use this technique for the first time within the frame of generating *low frequency squeezing* [102], where it was successfully applied, however in a different scenario.

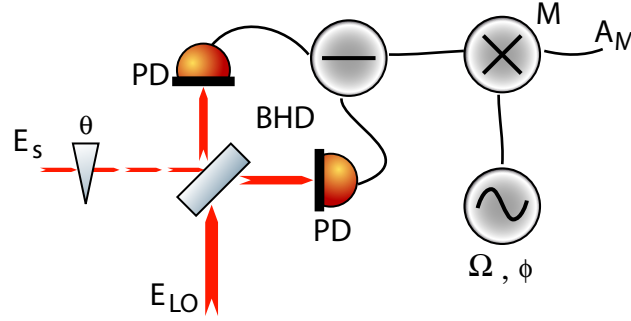


Figure A.1 - Phase readout scheme for the single side band technique. BHD: Balanced homodyne detector. E_s : Signal field carrying the single sideband with a frequency shift of Ω with respect to E_{LO} and a phase shift θ . E_{LO} : Local oscillator at the fundamental laser frequency ω . M: Doubly balanced mixer. A_M mixer output signal.

In a setup as depicted in Figure A.1 a BHD is operated with a local oscillator $E_{LO}(t) = E_{LO}^0 e^{i\omega t}$ at the fundamental laser frequency ω . The signal field $E_s(t) = e^{i\theta}(E_{exp}(t) + E_{ssb}(t))$ is a superposition of two fields: $E_{exp}(t)$ denotes the field, whose quadrature determined by the detection phase θ is to be measured for the main experiment. The auxiliary field $E_{ssb}(t) = E_{ssb}^0 e^{i(\omega+\Omega)t}$ is phase-locked to E_{exp} , see Section 3.1.2 and Section A.1.1.

Following the calculations of Section 3.3 we obtain for the BHD signal A_{BHD} :

$$\begin{aligned} A_{BHD}(t) &\propto \Re[E_{LO}(t)^* E_s(t)] \\ &= E_{LO}^0 \left(E_{exp} e^{-i(\omega t + \phi)} + E_{ssb}^0 e^{i(\Omega t + \theta)} \right) \\ &\propto X_{exp}(\theta) + E_{ssb} \cos(\Omega t + \theta), \end{aligned} \quad (\text{A.5})$$

with $X_{exp}(\phi)$ corresponding to a quadrature of E_{exp} rotated by θ . This signal is fed into

a mixer (M, Figure A.1), which basically (see Section 3.5) multiplies $A_{\text{BHD}}(t)$ with an electrical local oscillator $A_{\text{eLO}}(t) = A_{\text{eLO}}^0 \sin(\Omega t + \phi)$. We assume that X_{exp} is negligibly small compared to E_{ssb} and obtain for the mixer output signal A_{M} :

$$\begin{aligned} A_{\text{M}} &= A_{\text{BHD}} \cdot A_{\text{eLO}}(t) \\ &\propto \cos(\Omega + \theta) \sin(\Omega + \phi) \\ &= \frac{1}{2} (\sin(\phi - \theta) + \sin(2\Omega t + \phi + \theta)) \end{aligned}$$

$$\text{low pass filtered} \rightarrow \propto \sin(\phi - \theta). \quad (\text{A.6})$$

For $\phi = \theta$ the result is linear in the difference and thus can serve as an error signal a control loop actuating the phase θ of the signal field. In the stable closed loop the quadrature detection phase is determined by the phase of the electrical local oscillator. Note that this in turn requires the electrical local oscillator used for the phase lock of the auxiliary field, see Section 3.1.2, and the one used here to have the same frequency and a fixed phase. How these electrical local oscillators have been prepared is described in Section A.1.2.

A.1.1 Auxiliary Phase-Locked Laser

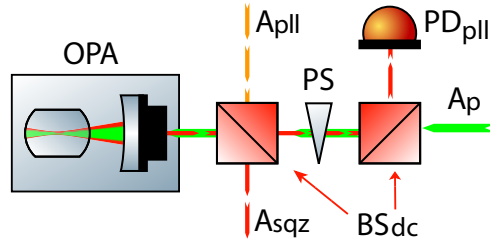


Figure A.2 - Injection scheme for the phase-locked auxiliary laser. A_{pll} : auxiliary laser field. A_{p} : second harmonic pump field. A_{sqz} : squeezed field with control field. BS_{dc} : dichroic beam splitter, reflects NIR, transmits green. PS: phase shifter. PD_{pll} : photo detector detecting the beat note of A_{pll} and the fundamental field emerging the OPA.

The only way to feed some of the auxiliary laser field into the squeezed mode is to use a beam splitter. However, the insertion of an extra beam splitter would inevitably lead to extra loss on the squeezed mode. The existing dichroic beam (left one in Figure A.2) splitter separating the pump from the squeezed field is supposed to be a perfect mirror for the squeezed field. But in reality, it is not: it rather reflects 99.5% and transmits the rest of the incident NIR intensity. Since this component has to be there anyway, it displays the perfect measure of superimposing the auxiliary field to the squeezed one. The beam splitter port transmitting the residual 0.5% of the squeezed light and reflecting 99.5% of the auxiliary laser can be used to detect the beat note for the phase lock. However, the main purpose of this port is to carry the pump mode. Hence, yet another dichroic beam splitter (right one in Figure A.2) has to be inserted into this path

to separate the pump from the beat note field.

In this setup the phase of the auxiliary field is locked to the fundamental field emerging the OPA cavity. The phase of the pump field and thus the orientation of the squeezing ellipse is locked to the same fundamental field by the loop discussed in Section 3.2.2. Hence, the phase of the auxiliary field maps the orientation of the squeezing ellipse.

A.1.2 The Mixer Box

The locking scheme of the balanced homodyne detectors in the frame of quantum state tomography relied on a control scheme, which allowed the optical detection phase to be determined by the phase of an electrical local oscillator (eLO), see Section A.1. For the experiment of Section 4.4 there were six balanced homodyne detectors to be controlled simultaneously. Yet another eLO was necessary for the phase-locked loop of the auxiliary laser, see Section 3.1.2, which the scheme is based on. All eLOs had to run coherently at the same frequency with a fixed but adjustable phase. To not overstrain the experimentalist the phases had to be controllable by a computer, see Section 2.3.2.

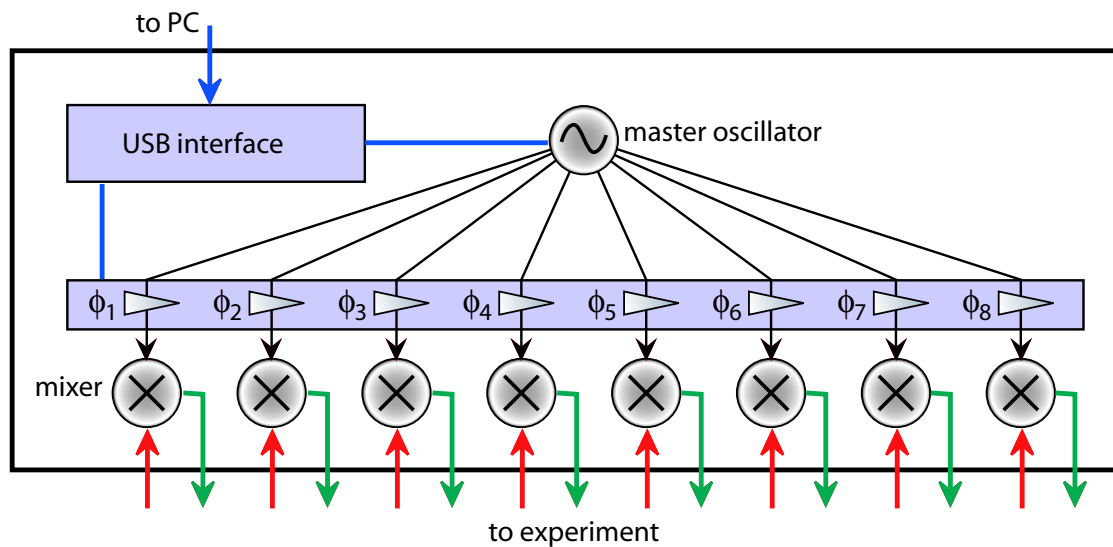


Figure A.3 - The oscillator box provides eight input and eight output ports for mixing signals with local oscillators with mutually fixed phases $\phi_1 \dots \phi_8$. Each phase can be set individually, which is controlled by a LabView interface.

The eLO generation was based on the *digital waveform synthesizer* chip AD9959 by Analog devices, providing four outputs derived from one master oscillator. The possibility to phase lock the master oscillator to another oscillator was used to link two of these chips together, such that the eight outputs were synchronized. The proprietary serial interface of the AD9959 was used to program each output with a LabView program running on a computer via a digital output interface (NI USB 6501 by National Instruments).

The AD9959 was available on an evaluation board providing all the support electronics to run the chip. Two of these boards were mounted in a metal case to shield inevitable radio frequency stray radiation. For the same reason this case also housed the amplifiers required to provide the appropriate signal power for a local oscillator. Likewise the mixers, which the local oscillators were used for, sat in the same case with all the appropriate support electronics. Although the total length of wiring connected to the mixer may not change with the location of the mixers, it is a good idea to keep the wiring of the local oscillator short. Usually the local oscillator signal is the strongest and thus the *antennas* displayed by the wiring should be short.

A.2 Electronics

A.2.1 Broadband Photo Detector

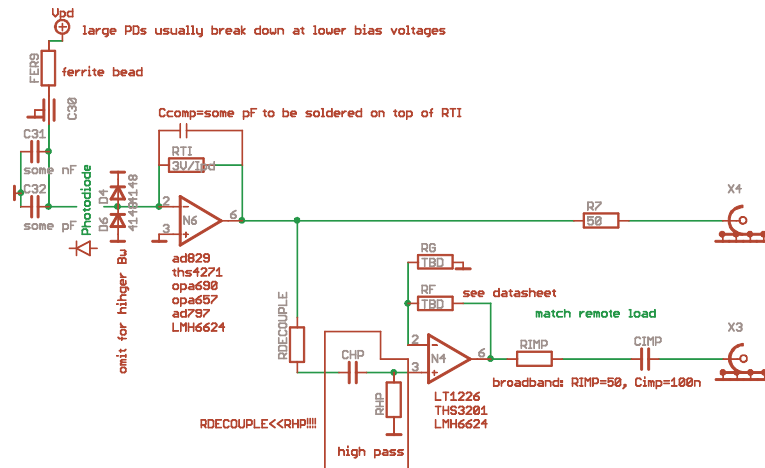


Figure A.4 - This circuit is a textbook transimpedance amplifier (upper pass), which converts the photo current into a proportional voltage via the resistor RTI. For the balanced homodyne detectors we used the OP: AD829 by Analog Devices. This device exhibits a high bandwidth and a low input noise figure at the same time. An additional amplifier provided a high gain factor for the AC component of the signal (lower pass).

A.2.2 Resonant Photo Detector

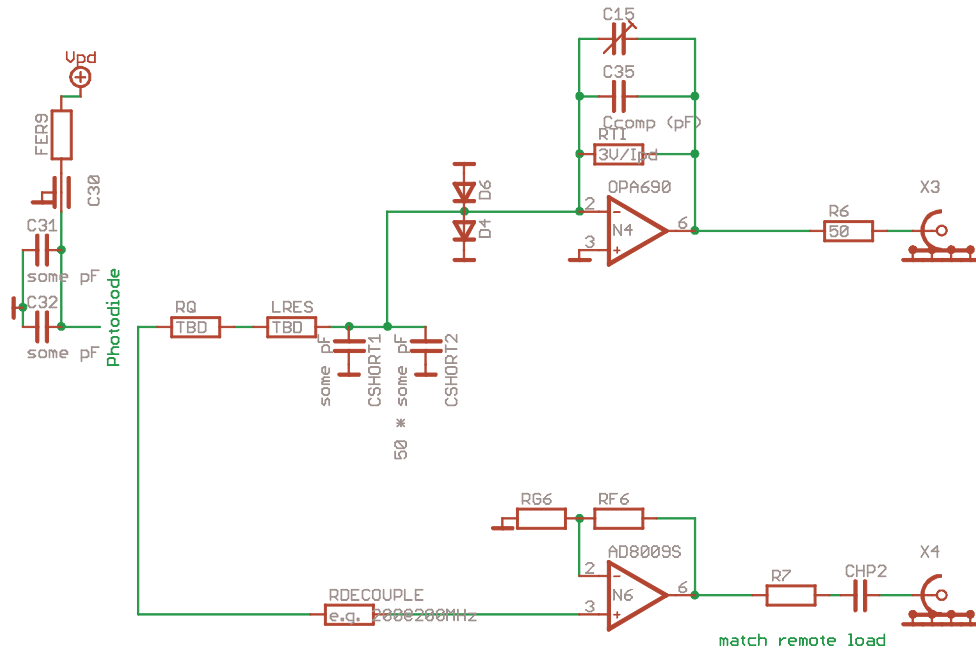


Figure A.5 - In this circuit the high impedance of the resonant tank formed by the capacity of the photo diode and the inductor LRES causes a high current-to-voltage conversion factor at the resonance frequency. This voltage is further amplified in the lower path. The upper path is a low speed transimpedance amplifier.

A.2.3 Amplifier and Mixer for the Mixer Box

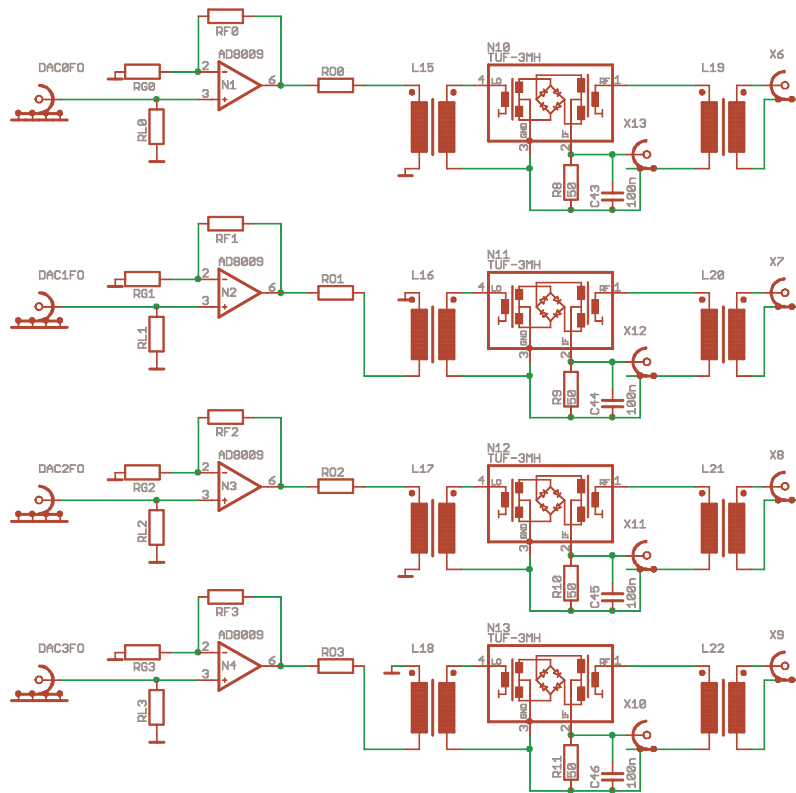


Figure A.6 - The board carrying this circuit was attached piggy-back to the AD9959 evaluation board by Analog Devices. The low power signals generated by the AD9959 were amplified to the appropriate power level of 7 dBm for the local oscillator input of the mixers (TUF3+ by Mini-Circuits). Two of these devices were housed in a well-shielded metal case, which efficiently suppressed stray radiation.

A.2.4 Subtractor / Adder for BHDs

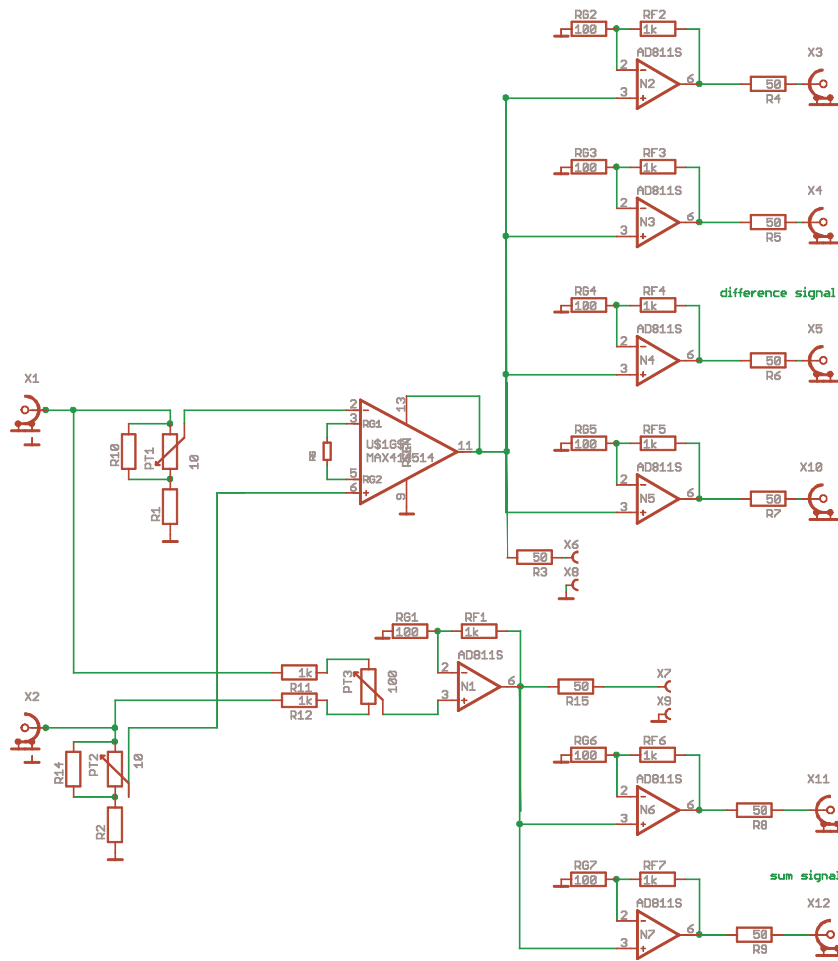


Figure A.7 - For the subtractor the line receiver IC MAX4145 was chosen for its high band width and common mode rejection ratio. The output signal was split and amplified as it was used for various purposes at the same time. The adder is a textbook circuit.

A.2.5 Improved SHG Electronics

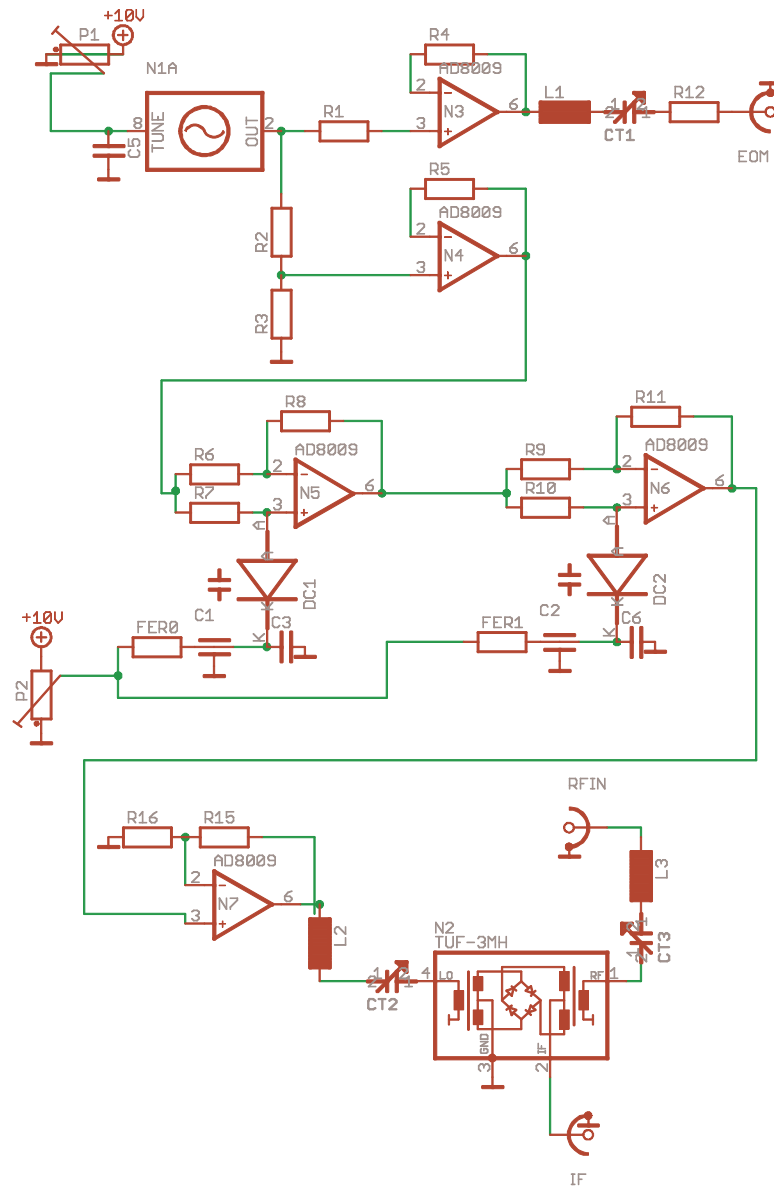


Figure A.8 - This circuit was fitted on a tiny board in order to fit inside the SHG in the Laser head. It consisted of an oscillator at 200MHz with an appropriate amplifier to drive the EOM in the laser head (top section). The oscillator signal was split and sent through an allpass filter (mid section) in order to tune the demodulation phase for the subsequent mixer (bottom). The whole radio frequency part of the modulation / demodulation scheme could be confined inside the laser head.

Calculus For Fun

B.1 Error Signals

Here we restrict ourselves to the case, in which the state of the system to be controlled is characterized by a single quantity X_p , usually a voltage proportional to the real quantity like temperature or intensity. This quantity is a function of a single parameter $X_p(\phi)$ of the system, which can be changed usually by applying a voltage X_c on a dedicated part of the system.

B.1.1 Linear Set Point

In the easiest scenario $X_p(\phi)$ depends linear on ϕ in the neighborhood of the desired state $X_s = X_p(\phi_{set})$. The error signal $X_{es} = X_s - X_p(\phi)$ is proportional to the deviation of the system's actual state from the desired one. Given that and additionally a linear dependence of ϕ on X_c , X_{es} can be filtered and fed back to X_c by a controller. With appropriate filtering this gives a well stabilized system sitting at the set point X_s , see [103].

B.1.2 Extremal Set Point

The situation becomes a bit more complicated when X_p is extremal for ϕ_{set} . Here $X_s - X_p(\phi)$ has always the same sign and thus contains no information about whether ϕ is too small or too large. The technique of modulation and demodulation helps out: A slight jiggling with the modulation frequency Ω and the amplitude m is applied to ϕ . The resulting signal $X_p(\phi + m \cos \Omega t)$ is demodulated with the same frequency, i.e. it is multiplied with a periodic (modulation period) function and temporally integrated (low pass filtered).

$$X_{es} = \frac{1}{\tau} \int_t^{t+\tau} \cos(\Omega t) \cdot P(\phi_{free} + m \cos \Omega t) dt. \quad (\text{B.1})$$

Because $P\phi$ is measured in the laboratory it is likely to be quite often differentiable and thus may be represented by its Taylor series $P(\phi) = \sum_{n=0}^{\infty} \frac{\partial_n P(\phi_0)}{n!} (\phi - \phi_0)$, which for small m can be terminated after the first element:

$$X_{es} \approx \frac{1}{\tau} \int_t^{t+\tau} \cos(\Omega t) \cdot (P(\phi_{\text{free}}) + (m \cos \Omega t) \partial_{\phi} P(\phi_{\text{free}})) dt \quad (\text{B.2})$$

$$= \frac{1}{\tau} \int_t^{t+\tau} \cos(\Omega t) \cdot P(\phi_{\text{free}}) + (m \cos^2 \Omega t) \partial_{\phi} P(\phi_{\text{free}}) dt. \quad (\text{B.3})$$

Even with the next Taylor element taken into account the only term with nonzero mean is the \cos^2 term. Its mean is one half, which is integrated over the period τ , which is chosen to be smaller than the smallest interesting period in ϕ_{free} , but much larger than the modulation period $2\pi/\Omega$:

$$X_{es} = \frac{1}{\tau} \left(\frac{\tau m}{2} \right) \partial_{\phi} P(\phi_{\text{free}}). \quad (\text{B.4})$$

Now we have the derivative of the signal to be kept extremal at hand. This is proportional to a slight deviation from the extremum because the extremum is best approximated by a parabola, whose derivative is the desired line through the origin.

B.1.3 Extremal Not Modulatable Set Point, PDH Method

An even more complicated case arises when ϕ cannot or must not be modulated. There is no general solution for such a problem, but the special case discussed in this section happens so often, that it appears to be general: The length of a cavity is to be stabilized on resonance for the laser light with the optical frequency ω . For one reason or another the length of the resonator cannot be modulated. Solely the power reflected from the cavity is measurable. To obtain an error signal people modulate the phase of the incoming laser field, see Section B.2.2 and demodulate the detected power. How does that work? Assuming the single mode steady state we find the reflection coefficient according to Section B.3 for a laser field at frequency ω from a cavity with round trip length L , real amplitude reflectivities ρ_n and ρ_f for the near and the far mirror and round trip loss δ : The frequency dependence $e^{i\omega L/c}$ is often expressed in terms of the so called tuning parameter $\phi = (\omega L/c) \bmod 2\pi$:

$$\rho(\omega) = \frac{\rho_n - \rho_f \delta e^{i\omega L/c}}{1 - \rho_n \rho_f \delta e^{i\omega L/c}}. \quad (\text{B.5})$$

We obtain the power of the reflected phase modulated field from the cavity by cal-

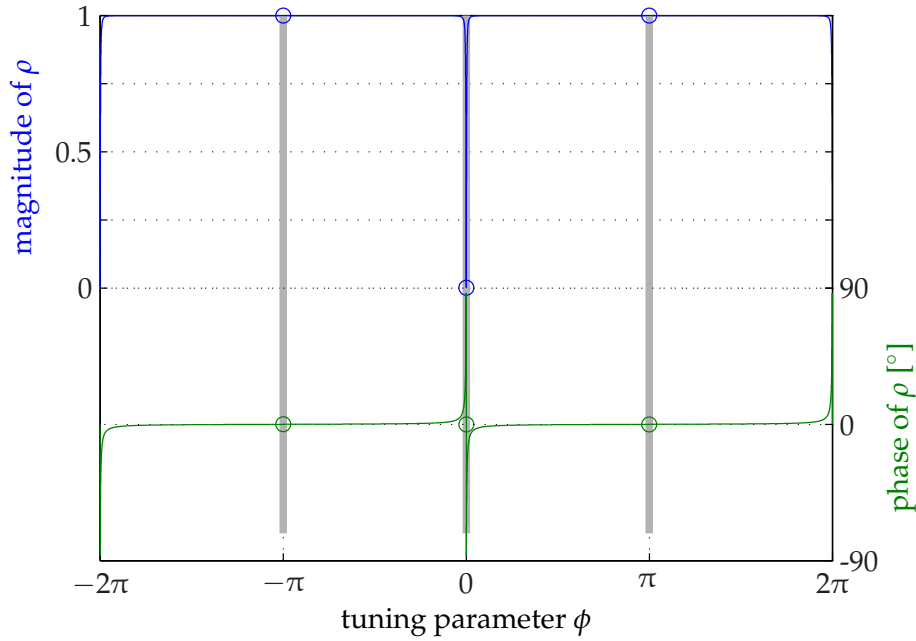


Figure B.1 - Amplitude reflection coefficient ρ for a moderate mode cleaner (impedance matched, $F = 300$). The grey bars indicate the frequency components of a phase modulated field. The modulation frequency is as much outside the linewidth as possible.

culating the reflection coefficient for every frequency component of Equation B.16,

$$E_r = E_0 \left(\rho(\omega) e^{-i\omega t} + \rho(\omega + \Omega) \frac{im}{2} e^{-i(\omega+\Omega)t} + \rho(\omega - \Omega) \frac{im}{2} e^{-i(\omega-\Omega)t} \right), \quad (\text{B.6})$$

and taking the absolute square $E_r^* E_r$. The demodulation picks only those terms of $E_r^* E_r$ which oscillate at Ω :

$$X_\Omega = X_0 \left(\text{Re}(\rho_c^* (\rho_u - \rho_l)) \sin \Omega t + \text{Im}(\rho_c^* (\rho_u + \rho_l)) \cos \Omega t \right), \quad (\text{B.7})$$

with $\rho_c = \rho(\omega)$, $\rho_l = \rho(\omega - \Omega)$ and $\rho_u = \rho(\omega + \Omega)$. By choosing the demodulation phase it can be chosen which linear combination of the sine and cosine term is detected. We deduce that there is a signal in the sine quadrature, when there is for example an imbalance of ρ_l and ρ_u . On the other hand the cosine quadrature is fed for example from an imaginary component of ρ_c .

How does that apply on the cavity problem? Figure B.1 shows the reflection coefficient ρ for a moderate mode cleaner. The grey bars indicate the frequency components of the phase modulated field. The modulation frequency is well outside the line width of the cavity. The error signal can be *seen* by shifting the grey bars left and right, i.e. detuning the laser. There is hardly any effect on ρ_l or ρ_u , but ρ_c is strongly affected, which

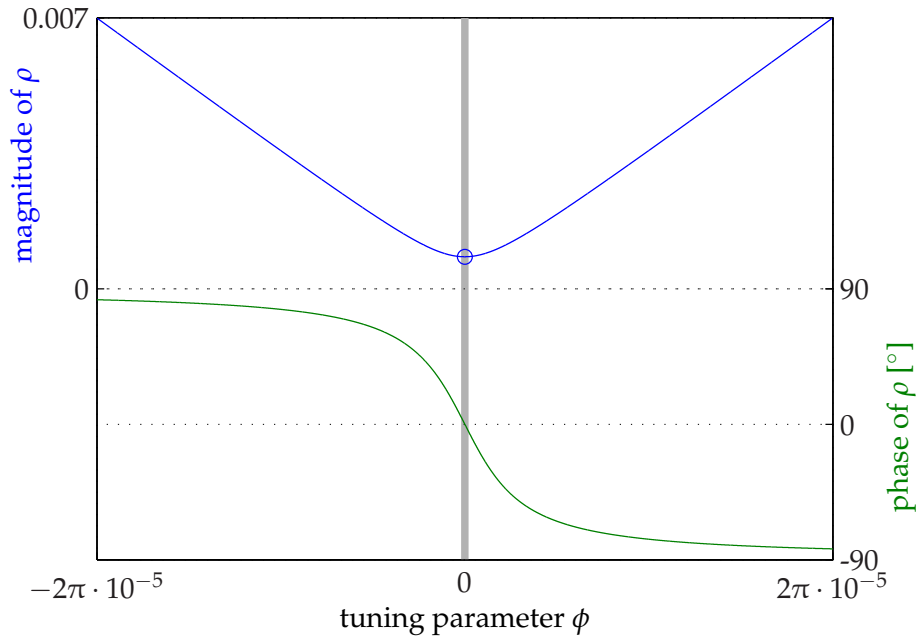


Figure B.2 - Close view of the center part of Figure B.1

is resolved in Figure B.2. For a small detuning ρ_c gets a phase shift proportional to the detuning and thus for the generation of an error signal the demodulation phase should be chosen to demodulate the cosine quadrature.

The situation is different when the modulation frequency is within the cavity line and the cavity is far from being impedance matched, which is the case for the OPA cavities, see Section 3.2. In this case the phase modulated field is sent from the strongly under-coupled side of the cavity. The reflection coefficient is shown in Figure B.3. The impact of detuning on the phase of three components is small on the one hand and the same on the other hand, because the phase is approximately linear in the relevant range. Thus there is only a small signal in the cosine quadrature. But detuning creates an imbalance between ρ_l and ρ_u and an error signal can be generated by demodulating in the sine quadrature. In Section 3.2.2 you can read, why this is worth mentioning.

B.2 Modulation Of Light Fields

Assume, we have a single mode laser beam at frequency ω . After packing the spatial shape, the amplitude and polarization into E_0 we can write the field as

$$E(t) = E_0 e^{-i\omega t}. \quad (\text{B.8})$$

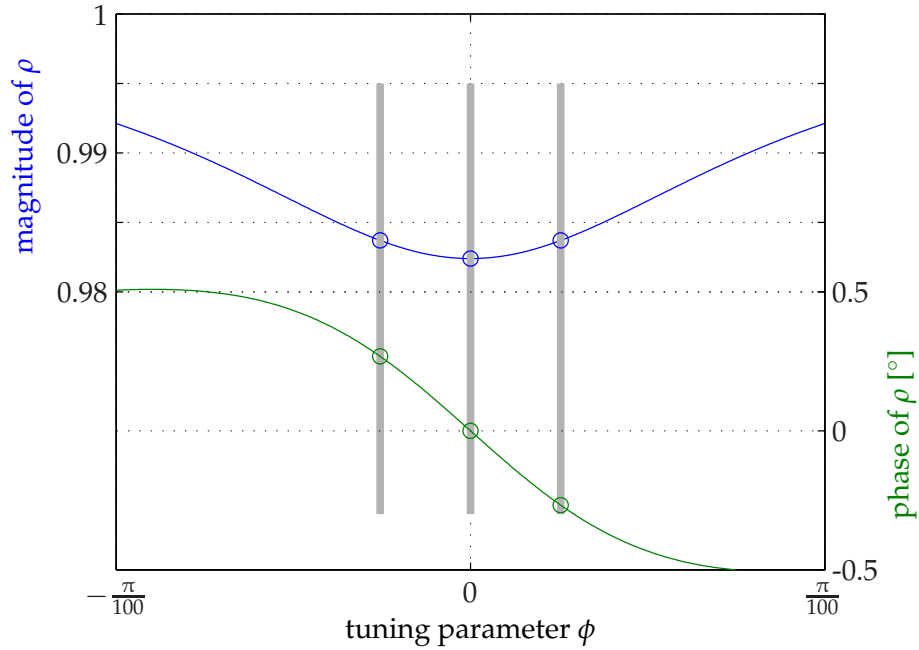


Figure B.3 - Amplitude reflection coefficient ρ for the under coupled view of an OPA cavity, $F = 110$. The grey bars indicate the frequency components of a phase modulated field. The modulation frequency is well within the line width.

B.2.1 Amplitude Modulation

A cosine shaped periodic (Ω) change of depth m of the amplitude reads:

$$E_{\text{am}}(t) = E_0 (1 + m \cos \Omega t) e^{-i\omega t} \quad (\text{B.9})$$

$$= E_0 \left(1 + \frac{m}{2} (e^{-i\Omega t} + e^{i\Omega t}) \right) e^{-i\omega t} \quad (\text{B.10})$$

$$= E_0 \left(e^{-i\omega t} + \frac{m}{2} e^{-i(\omega+\Omega)t} + \frac{m}{2} e^{-i(\omega-\Omega)t} \right). \quad (\text{B.11})$$

This leads to the term side band picture where in steady state a field is represented by its frequency components. In the case of a cosine shaped amplitude modulation there are exactly three single frequency fields involved, the carrier at frequency ω and the two amplitude modulation fields at $\omega + \Omega$ and $\omega - \Omega$, which are often termed *side bands*. The original term side band refers to a piece of frequency space in proximity of the carrier. This kind of modulation can be detected by a power (E^*E) detector:

$$E_{\text{am}}^*(t)E_{\text{am}}(t) = E_0^* (1 + m \cos \Omega t) e^{+i\omega t} E_0 (1 + m \cos \Omega t) e^{-i\omega t} \quad (\text{B.12})$$

$$= E_0^* E_0 (1 + 2m \cos \Omega t + m^2 \cos^2 \Omega t). \quad (\text{B.13})$$

B.2.2 Phase Modulation

The *other* modulation, the *phase modulation*, is a bit more tricky:

$$E_{\text{pm}}(t) = E_0 e^{im \cos(\Omega t)} e^{-i\omega t}. \quad (\text{B.14})$$

For a very small modulation index m the first exponential can be approximated by the first two elements of its Taylor series:

$$E_{\text{pm}}(t) \approx E_0 (1 + im \cos(\Omega t)) e^{-i\omega t} \quad (\text{B.15})$$

$$= E_0 \left(e^{-i\omega t} + \frac{im}{2} e^{-i(\omega+\Omega)t} + \frac{im}{2} e^{-i(\omega-\Omega)t} \right). \quad (\text{B.16})$$

The result looks quite similar to the one in the previous section. The important difference is the phase relation of the three fields, i.e. the i in front of the sideband fields. This kind of modulation cannot be detected directly:

$$E_{\text{pm}}^*(t)E_{\text{pm}}(t) = (E_0^* e^{-im \cos(\Omega t)} e^{i\omega t})(E_0 e^{im \cos(\Omega t)} e^{-i\omega t}) \quad (\text{B.17})$$

$$\equiv E_0^*E_0. \quad (\text{B.18})$$

An overall phase shift does not change the situation. But a frequency discriminating device would do so, if it changed the phase of only the carrier or one of the sideband fields. The latter can be expressed by a carrier phase shift plus an overall one. Assuming only the carrier is shifted by ϕ , the 1 in Equation B.15 has to be multiplied by $e^{i\phi}$:

$$E(t) \approx E_0 (e^{i\phi} + im \cos(\Omega t)) e^{-i\omega t}. \quad (\text{B.19})$$

What is the power of this expression?

$$E^*(t)E(t) = E_0^*E_0 (e^{-i\phi} - im \cos(\Omega t)) (e^{i\phi} + im \cos(\Omega t)) \quad (\text{B.20})$$

$$= E_0^*E_0 (1 + m \sin \phi \cos(\Omega t) + m^2 \cos^2(\Omega t)). \quad (\text{B.21})$$

This expression contains a term oscillating at the modulation frequency Ω , which is proportional to the phase shift ϕ (for $\phi \approx 0$)! Note that this oscillation is in phase with the initial modulation signal.

Something similar will happen, if the power balance of the two modulation sideband fields is disturbed:

$$E(t) \approx E_0 \left(1 + \frac{i(m-\delta)}{2} e^{-i\Omega t} + \frac{i(m+\delta)}{2} e^{+i\Omega t} \right) e^{-i\omega t} \quad (\text{B.22})$$

$$= E_0 (1 + im \cos(\Omega t) + \delta \sin(\Omega t)) e^{-i\omega t}. \quad (\text{B.23})$$

The power of this expression reads:

$$E^*(t)E(t) = E_0^*E_0 (1 + m^2 \cos^2 \Omega t + \delta^2 \sin^2 \Omega t + 2\delta \sin \Omega t). \quad (\text{B.24})$$

Again there is a term oscillating with the modulation frequency Ω but 90 out of phase with the initial modulation signal!

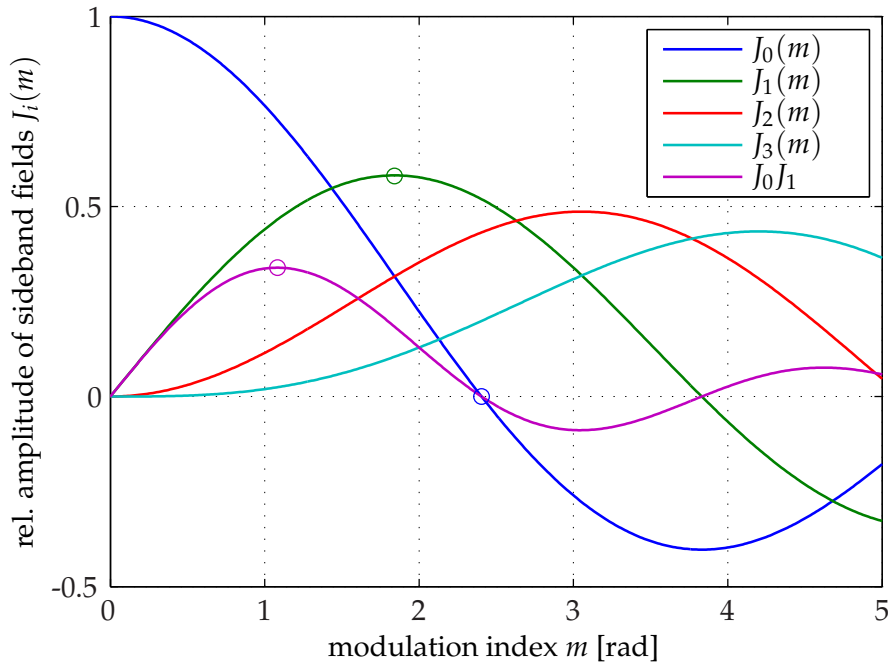


Figure B.4 - A bunch of Bessel functions and the product $J_0 \cdot J_1$. The latter tells you how *big* your error signal will be. Note that only J_1 has a slope $\neq 0$ at the origin.

What is the flap about these Bessel functions? They show up through the Jacobi-Anger identity:

$$e^{im \cos \Omega t} = \sum_{n=-\infty}^{\infty} i^n J_n(m) e^{in\Omega t}. \quad (\text{B.25})$$

Here, $J_n(m)$ denote the first kind Bessel functions. For positive integer n they obey the identity $J_{-n}(m) = (-1)^n J_n(m)$:

$$e^{im \cos \Omega t} = J_0(m) + \sum_{n=1}^{\infty} i^n J_n(m) (e^{in\Omega t} + e^{-in\Omega t}). \quad (\text{B.26})$$

In contrast to the previous section there are more and more side bands generated for larger values of m . For small values of m we obtain the previous result $J_0 \approx 1$ and $J_1 \approx m/2$ for all other Bessel functions the linear term vanishes.

Experimentally interesting are three distinct values for the modulation index. The

first at $m \approx 1.082$ is the modulation index which maximizes the possible error signal obtained from PDH technique because it is proportional to the power at the demodulation frequency which is proportional to the product of the field amplitudes. Second is $m \approx 1.841$ where the fields at $\omega \pm \Omega$ have their maximal amplitude. For the other is at $m \approx 2.405$ the carrier at ω vanishes.

B.3 The Naive Optical Resonator

The topology, the length, the radii of curvature of the mirrors and possibly intra cavity elements determine the transverse shape and size of the cavity eigenmodes, and whether there are some at all [104, 105]. Here we assume a stable resonator and a perfect match of all other fields involved to one and the same eigenmode.

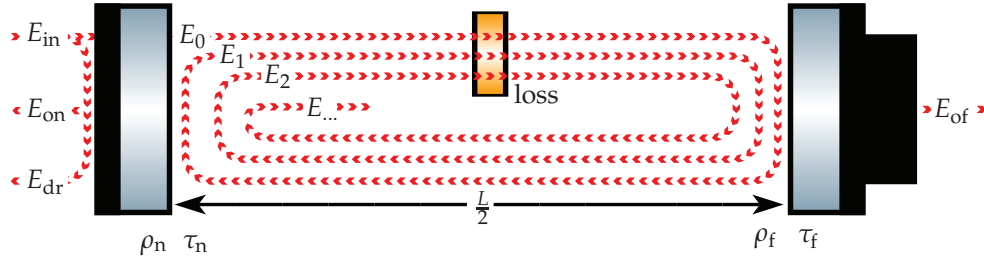


Figure B.5 - The spatial shape of E_{in} perfectly matches the considered cavity eigenmode. The amplitude reflection and transmission coefficients are denoted by ρ and τ . A whole round trip lasts L/c , after which the amplitude is attenuated by the factor δ due to accumulated loss.

The fields E_m inside the resonator shall be considered as the *piece* of field at the left mirror propagating to the right after m round trips disregarding any interference. Thus, the first piece is a fraction the input field E_{in} , attenuated by the mirror transmission: $E_0 = \tau_n E_{in}$. After one round trip the phase evolved corresponding to the wave number $k = \omega/c$ of the field and the distance L it propagated. During this propagation the field is reflected once from each mirror (ρ_n, ρ_f) and attenuated (δ) by generic loss. The phase shift due to reflection is chosen to vanish for intra cavity reflections. Hence this shift equals π for the outside reflection. In total this yields $E_1 = \rho_n \rho_f \delta \exp(-i\omega L/c) E_0$. The same holds for the next round trip, and thus

$$E_m = \rho_n \rho_f \delta e^{(-i\omega L/c)} E_{m-1} = \left(\rho_n \rho_f \delta e^{(-i\omega L/c)} \right)^m E_0. \quad (\text{B.27})$$

To obtain the total field E_c at the left mirror propagating to the right, we have to super-

impose (add) all *pieces*.

$$\begin{aligned}
 E_c &= \sum_{m=0}^{\infty} E_m \\
 &= E_0 \sum_{m=0}^{\infty} \left(\rho_n \rho_f \delta e^{(-i\omega L/c)} \right)^m \\
 &= E_0 \frac{1}{1 - \rho_n \rho_f \delta e^{(-i\omega L/c)}} \\
 &= E_{\text{in}} \frac{\tau_n}{1 - \rho_n \rho_f \delta e^{(-i\omega L/c)}}. \tag{B.28}
 \end{aligned}$$

The last step is valid because the magnitude of the base in the sum in the second line is guaranteed to be smaller than one, and thus the geometric series converges. This expression becomes large whenever the exponential in the denominator gets close to one, i.e. $(\omega L/c \bmod 2\pi) = 0$. The piece of frequency space between two adjacent resonances is called free spectral range $\nu_{\text{FSR}} = c/L$ (physical frequency). Note that the free spectral range solely depends on the length of the cavity. The frequency dependence is often expressed by the tuning parameter $\phi = (\omega/\nu_{\text{FSR}} \bmod 2\pi)$. The other characteristic frequency is the width of the resonance which is usually given by the full width at half maximum of the power, i.e. the absolute square of the field inside the resonator P_c or the transmitted field or full width at half minimum of the reflected power. For the sake of simplicity all dispensable quantities are omitted:

$$P_c \propto \frac{1}{1 - \rho_n \rho_f \delta (2 \cos \phi - \rho_n \rho_f \delta)}. \tag{B.29}$$

Now we have to solve $\frac{1}{2}P_c(\phi = 0) = P_c(\phi)$ for ϕ :

$$\begin{aligned}
 \frac{1}{2} \frac{1}{1 - 2\rho_n \rho_f \delta + \rho_n^2 \rho_f^2 \delta^2} &= \frac{1}{1 - 2\rho_n \rho_f \delta \cos \phi + \rho_n^2 \rho_f^2 \delta^2}, \\
 2 - 4\rho_n \rho_f \delta + 2\rho_n^2 \rho_f^2 \delta^2 &= 1 - 2\rho_n \rho_f \delta \cos \phi + \rho_n^2 \rho_f^2 \delta^2, \\
 \frac{1}{2} \left(\frac{1}{\rho_n \rho_f \delta} + \rho_n \rho_f \delta - 4 \right) &= \cos \phi. \tag{B.30}
 \end{aligned}$$

Because of the symmetry of the cosine there are two solutions, one for each side. The difference between both yields the line width $\Delta\phi$ in terms of the tuning parameter or $\Delta\nu$ for the frequency:

$$\begin{aligned}
 \Delta\phi &= 2 \arccos \left[\frac{1}{2} \left(\frac{1}{\rho_n \rho_f \delta} + \rho_n \rho_f \delta - 4 \right) \right], \\
 \Delta\nu &= \frac{\nu_{\text{FSR}}}{\pi} \arccos \left[\frac{1}{2} \left(\frac{1}{\rho_n \rho_f \delta} + \rho_n \rho_f \delta - 4 \right) \right]. \tag{B.31}
 \end{aligned}$$

For reflectivities close to one and very low loss we can approximate this rather complicated expression by the first two elements of its power series about $\rho_n \rho_f \delta = 1$. This yields much more intuitive but also quite inaccurate results:

$$\begin{aligned}\Delta\phi &\approx 2(1 - \rho_n \rho_f \delta), \\ \Delta\nu &\approx \frac{\nu_{\text{FSR}}}{\pi}(1 - \rho_n \rho_f \delta).\end{aligned}\tag{B.32}$$

A much more accurate approximation can be obtained by going one step back to Equation B.29. Now we assume, that the line width of the resonance is small compared to the free spectral range, i.e. we can approximate the cosine by $\cos \phi \approx 1 - \phi^2/2$ and with this substitution solve $\frac{1}{2}P_c(\phi = 0) = P_c(\phi)$ for ϕ and take the difference of both solutions again:

$$\begin{aligned}\Delta\phi &\approx 2(1 - \rho_n \rho_f \delta) / \sqrt{\rho_n \rho_f \delta}, \\ \Delta\nu &\approx \frac{\nu_{\text{FSR}}}{\pi}(1 - \rho_n \rho_f \delta) / \sqrt{\rho_n \rho_f \delta}.\end{aligned}\tag{B.33}$$

The quality factor of the resonator is most commonly given by the Finesse $F = \nu_{\text{FSR}} / \Delta\nu =$

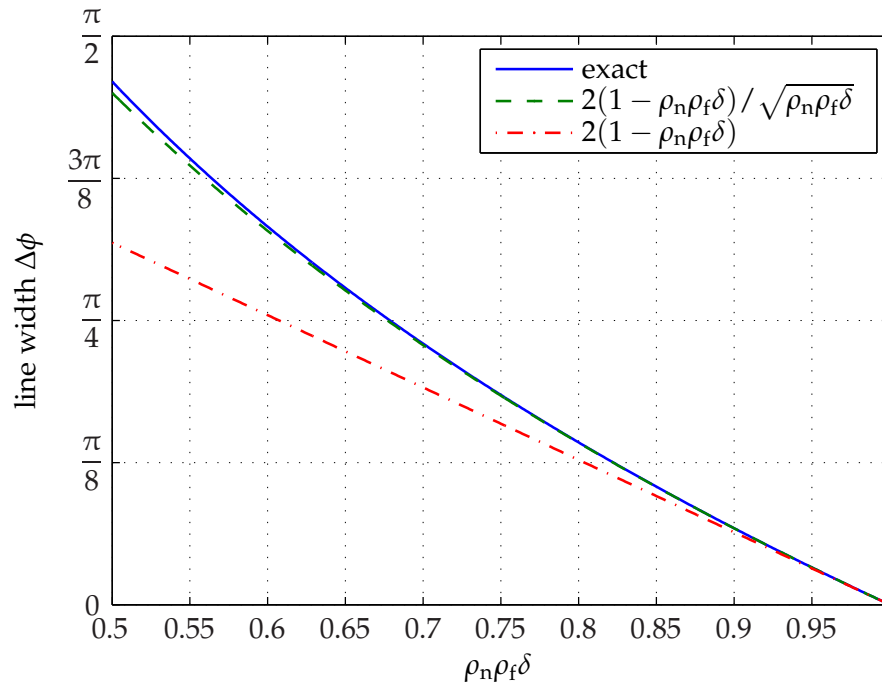


Figure B.6 - Although the assumptions seem to be very similar their accuracy differs significantly. See Equation B.31 for the exact solution. But obviously the popular formula Equation B.33 is good even for moderate reflectivities.

$2\pi / \Delta\phi$, which can easily be derived from the above. The most commonly used formula

relates to Equation B.33 and reads:

$$F = \frac{\pi\sqrt{\rho_n\rho_f\delta}}{1 - \rho_n\rho_f\delta}. \quad (\text{B.34})$$

The transmitted field E_{of} is formed by the propagation of E_c to the far mirror and the transmission through it. This yields the total frequency dependent transmission coefficient $\tau(\omega)$ of the cavity which is also called the transfer function as the transmitted field is normalized by the input field:

$$\tau(\omega) = \frac{\tau_n\tau_f\delta e^{(-i\omega L/2c)}}{1 - \rho_n\rho_f\delta e^{(-i\omega L/c)}}. \quad (\text{B.35})$$

The total reflected E_r field is formed by the interference of the field reflected directly from the near mirror $E_{\text{dr}} = -\rho_n E_{\text{dr}}$ and the field leaving the resonator to the left E_{on} . The latter can be derived from E_c analogous to the transmitted field: propagation, reflection from the far mirror, transmission through the near mirror:

$$E_r = E_{\text{dr}} + E_{\text{on}} \quad (\text{B.36})$$

$$= E_{\text{in}} \left(-\rho_n + \frac{\tau_n^2 \rho_f \delta e^{(-i\omega L/c)}}{1 - \rho_n \rho_f \delta e^{(-i\omega L/c)}} \right) \quad (\text{B.37})$$

$$\Rightarrow \rho(\omega) = \frac{-\rho_n + \rho_f \delta e^{(-i\omega L/c)}}{1 - \rho_n \rho_f \delta e^{(-i\omega L/c)}}. \quad (\text{B.38})$$

In the last line the identity $\rho^2 + \tau^2 = 1$ was used. The reflection coefficient $\rho(\omega)$ on resonance will vanish, if $\rho_n = \rho_f \delta$, which is called impedance matching.

There is a quite different approach: Solve the cavity's equation of motion for the electric field $E_c(t)$ inside, which works straight forward as long as the free spectral range is much larger than the line width. Given the latter we can describe the resonator as a harmonic oscillator with only a single eigenmode with the frequency ω_0 and disregard all the other longitudinal modes. The phase evolves like $\exp(i\omega_0 t)$ and thus $\dot{E}_c(t) = i\omega_0 E_c(t)$. The field partially gets lost by transmission through the mirrors and loss with the loss rates κ_n , κ_f and κ_l and it is fed by an external field $E_{\text{in}}(t) = E_{\text{in}} \exp(i\omega t)$ through the near mirror:

$$\dot{E}_c(t) = i\omega_0 E_c(t) - (\kappa_n + \kappa_f + \kappa_l) E_c(t) + \kappa_n E_{\text{in}} \exp(i\omega t). \quad (\text{B.39})$$

The homogenous solution is found via $\dot{E}_c(t)/E_c(t) = \partial_t \log E_c(t)$ and reads $E_{c,\text{hom}}(t) = E_{c,\text{hom}} \exp[(i\omega_c - \kappa_n - \kappa_f - \kappa_l)t]$, which is absolutely unimportant because at the beginning of all times there was nothing except from the vacuum inside the cavity and thus $E_{c,\text{hom}} = 0$.

Bibliography

- [1] EINSTEIN A., PODOLSKY B. and ROSEN N. *Can quantum-mechanical description of physical reality be considered complete?* Phys. Rev., **47** (1935) 777–780. doi:10.1103/PhysRev.47.777.
- [2] BELL J.S. *Speakable and unspeakable in quantum mechanics: collected papers on quantum philosophy. Collected papers on quantum philosophy.* Cambridge University Press (2004). ISBN 0521523389.
- [3] ASPECT A., GRANGIER P. and ROGER G. *Experimental tests of realistic local theories via bell's theorem.* Phys. Rev. Lett., **47** (1981) 460–463. doi:10.1103/PhysRevLett.47.460.
- [4] FURUSAWA A., SØRENSEN J.L., BRAUNSTEIN S.L., FUCHS C.A., KIMBLE H.J. and POLZIK E.S. *Unconditional quantum teleportation.* Science, **282** (1998) 706–709. doi:10.1126/science.282.5389.706.
- [5] TAKEI N., YONEZAWA H., AOKI T. and FURUSAWA A. *High-fidelity teleportation beyond the no-cloning limit and entanglement swapping for continuous variables.* Phys. Rev. Lett., **94** (2005) 220502. doi:10.1103/PhysRevLett.94.220502.
- [6] JIA X., SU X., PAN Q., GAO J., XIE C. and PENG K. *Experimental demonstration of unconditional entanglement swapping for continuous variables.* Phys. Rev. Lett., **93** (2004) 250503. doi:10.1103/PhysRevLett.93.250503.
- [7] JULSGAARD B., KOZHEKIN A. and POLZIK E.S. *Experimental long-lived entanglement of two macroscopic objects.* Nature, **413** (2001) 400–403. ISSN 0028-0836. doi:10.1038/35096524.
- [8] JULSGAARD B., SHERSON J., CIRAC J.I., FIURASEK J. and POLZIK E.S. *Experimental demonstration of quantum memory for light.* Nature, **432** (2004) 482–486. ISSN 0028-0836. doi:10.1038/nature03064.
- [9] SHERSON J.F., KRAUTER H., OLSSON R.K., JULSGAARD B., HAMMERER K., CIRAC I. and POLZIK E.S. *Quantum teleportation between light and matter.* Nature, **443** (2006) 557–560. ISSN 0028-0836. doi:10.1038/nature05136.

- [10] GROSSHANS F., VAN ASSCHE G., WENGER J., BROURI R., CERF N.J. and GRANGIER P. *Quantum key distribution using Gaussian-modulated coherent states*. *Nature*, **421** (2003) 238–241. ISSN 0028-0836. doi:10.1038/nature01289.
- [11] BRIEGEL H.J., DÜR W., CIRAC J.I. and ZOLLER P. *Quantum repeaters: The role of imperfect local operations in quantum communication*. *Phys. Rev. Lett.*, **81** (1998) 5932–5935. doi:10.1103/PhysRevLett.81.5932.
- [12] DUAN L.M., LUKIN M.D., CIRAC J.I. and ZOLLER P. *Long-distance quantum communication with atomic ensembles and linear optics*. *Nature*, **414** (2001) 413–418. ISSN 0028-0836. doi:10.1038/35106500.
- [13] BENNETT C.H., BRASSARD G., POPESCU S., SCHUMACHER B., SMOLIN J.A. and WOOTTERS W.K. *Purification of noisy entanglement and faithful teleportation via noisy channels*. *Phys. Rev. Lett.*, **76** (1996) 722–725. doi:10.1103/PhysRevLett.76.722.
- [14] DEUTSCH D., EKERT A., JOZSA R., MACCHIAVELLO C., POPESCU S. and SANPERA A. *Quantum privacy amplification and the security of quantum cryptography over noisy channels*. *Phys. Rev. Lett.*, **77** (1996) 2818–2821. doi:10.1103/PhysRevLett.77.2818.
- [15] ŻUKOWSKI M., ZEILINGER A., HORNE M.A. and EKERT A.K. *'Event-ready-detectors' Bell experiment via entanglement swapping*. *Phys. Rev. Lett.*, **71** (1993) 4287–4290. doi:10.1103/PhysRevLett.71.4287.
- [16] EISERT J., SCHEEL S. and PLENIO M.B. *Distilling Gaussian states with Gaussian operations is impossible*. *Phys. Rev. Lett.*, **89** (2002) 137903. doi:10.1103/PhysRevLett.89.137903.
- [17] GIEDKE G. and IGNACIO CIRAC J. *Characterization of Gaussian operations and distillation of Gaussian states*. *Phys. Rev. A*, **66** (2002) 032316. doi:10.1103/PhysRevA.66.032316.
- [18] FIURÁŠEK J., MAREK P., FILIP R. and SCHNABEL R. *Experimentally feasible purification of continuous-variable entanglement*. *Phys. Rev. A*, **75** 050302. doi:10.1103/PhysRevA.75.050302.
- [19] GLÖCKL O., ANDERSEN U.L., FILIP R., BOWEN W.P. and LEUCHS G. *Squeezed-state purification with linear optics and feedforward*. *Phys. Rev. Lett.*, **97** 053601. doi:10.1103/PhysRevLett.97.053601.
- [20] HEERSINK J., MARQUARDT C., DONG R., FILIP R., LORENZ S., LEUCHS G. and ANDERSEN U.L. *Distillation of squeezing from non-Gaussian quantum states*. *Phys. Rev. Lett.*, **96** 253601. doi:10.1103/PhysRevLett.96.253601.
- [21] FRANZEN A., HAGE B., DIGUGLIELMO J., FIURÁŠEK J. and SCHNABEL R. *Experimental demonstration of continuous variable purification of squeezed states*. *Phys. Rev. Lett.*, **97** 150505. doi:10.1103/PhysRevLett.97.150505.

- [22] HAGE B., FRANZEN A., DIGUGLIELMO J., MAREK P., FIURASEK J. and SCHNABEL R. *On the distillation and purification of phase-diffused squeezed states*. New Journal of Physics, **9** (2007) 227.
- [23] LEONHARDT U. *Measuring the Quantum State of Light*. Cambridge University Press (1997). ISBN 0521497302.
- [24] WALLS D.F. and MILBURN G.J. *Quantum optics*. Springer-Verlag, Berlin/New York, springer study ed. edn. (1995). ISBN 3540588310.
- [25] VOGEL W. and WELSCH D.G. *Quantum Optics*. Wiley-VCH (2006). ISBN 3527405070.
- [26] WIGNER E. *On the quantum correction for thermodynamic equilibrium*. Phys. Rev., **40** (1932) 749–759. doi:10.1103/PhysRev.40.749.
- [27] GLAUBER R.J. *Photon correlations*. Phys. Rev. Lett., **10** (1963) 84–86. doi:10.1103/PhysRevLett.10.84.
- [28] SUDARSHAN E.C.G. *Equivalence of semiclassical and quantum mechanical descriptions of statistical light beams*. Phys. Rev. Lett., **10** (1963) 277–279. doi:10.1103/PhysRevLett.10.277.
- [29] VON NEUMANN J. *Mathematische Grundlagen der Quantenmechanik*. Springer, Berlin (1995). ISBN 3540592075.
- [30] MAREK P., FIURÁŠEK J., HAGE B., FRANZEN A., DIGUGLIELMO J. and SCHNABEL R. *Multiple-copy distillation and purification of phase-diffused squeezed states*. Phys. Rev. A, **76** 053820. doi:10.1103/PhysRevA.76.053820.
- [31] SCHMIDT E. *Zur Theorie der linearen und nichtlinearen Integralgleichungen*. Mathematische Annalen, **63** (1907) 433–476. doi:10.1007/BF01449770.
- [32] WERNER R.F. *Quantum states with Einstein-Podolsky-Rosen correlations admitting a hidden-variable model*. Phys. Rev. A, **40** (1989) 4277–4281. doi:10.1103/PhysRevA.40.4277.
- [33] PERES A. *Separability criterion for density matrices*. Phys. Rev. Lett., **77** (1996) 1413–1415. doi:10.1103/PhysRevLett.77.1413.
- [34] VIDAL G. and WERNER R.F. *Computable measure of entanglement*. Phys. Rev. A, **65** (2002) 032314. doi:10.1103/PhysRevA.65.032314.
- [35] BRAUNSTEIN S.L. and VAN LOOCK P. *Quantum information with continuous variables*. Rev. Mod. Phys., **77** (2005) 513–577. doi:10.1103/RevModPhys.77.513.
- [36] REID M.D. *Demonstration of the Einstein-Podolsky-Rosen paradox using non-degenerate parametric amplification*. Phys. Rev. A, **40** (1989) 913–923. doi:10.1103/PhysRevA.40.913.

- [37] REID M.D. and DRUMMOND P.D. *Quantum correlations of phase in nondegenerate parametric oscillation.* Phys. Rev. Lett., **60** (1988) 2731–2733. doi:10.1103/PhysRevLett.60.2731.
- [38] BOWEN W.P., SCHNABEL R., LAM P.K. and RALPH T.C. *Experimental characterization of continuous-variable entanglement.* Phys. Rev. A, **69** (2004) 012304. doi:10.1103/PhysRevA.69.012304.
- [39] DIGUGLIELMO J., HAGE B., FRANZEN A., FIURÁŠEK J. and SCHNABEL R. *Experimental characterization of Gaussian quantum-communication channels.* Phys. Rev. A, **76** 012323. doi:10.1103/PhysRevA.76.012323.
- [40] DUAN L.M., GIEDKE G., CIRAC J.I. and ZOLLER P. *Inseparability criterion for continuous variable systems.* Phys. Rev. Lett., **84** (2000) 2722–2725. doi:10.1103/PhysRevLett.84.2722.
- [41] CAVES C.M. and SCHUMAKER B.L. *New formalism for two-photon quantum optics. i. quadrature phases and squeezed states.* Phys. Rev. A, **31** (1985) 3068–3092. doi:10.1103/PhysRevA.31.3068.
- [42] SCHUMAKER B.L. and CAVES C.M. *New formalism for two-photon quantum optics. ii. mathematical foundation and compact notation.* Phys. Rev. A, **31** (1985) 3093–3111. doi:10.1103/PhysRevA.31.3093.
- [43] KAK A.C. and SLANEY M. *Principles of Computerized Tomographic Imaging.* IEEE Press (1988).
- [44] VOGEL K. and RISKEN H. *Determination of quasiprobability distributions in terms of probability distributions for the rotated quadrature phase.* Phys. Rev. A, **40** (1989) 2847–2849. doi:10.1103/PhysRevA.40.2847.
- [45] SMITHEY D.T., BECK M., RAYMER M.G. and FARIDANI A. *Measurement of the wigner distribution and the density matrix of a light mode using optical homodyne tomography: Application to squeezed states and the vacuum.* Phys. Rev. Lett., **70** (1993) 1244–1247. doi:10.1103/PhysRevLett.70.1244.
- [46] BREITENBACH G., MÜLLER T., PEREIRA S.F., POIZAT J.P., SCHILLER S. and MLYNEK J. *Squeezed vacuum from a monolithic optical parametric oscillator.* J. Opt. Soc. Am. B, **12** (1995) 2304–2309.
- [47] THÜRING A. *Investigations of coupled and Kerr non-linear optical resonators.* Ph.D. thesis, Leibniz Universität Hannover (2009).
- [48] GEL'FAND I.M. and SHILOV G.E. *Generalized Functions.* Academic Press (1964). ISBN 0122795016.
- [49] OPPENHEIM A.V. *Discrete-Time Signal Processing.* Prentice Hall (1998). ISBN 0137549202.

- [50] RAYMER M.G., MCALISTER D.F. and LEONHARDT U. *Two-mode quantum-optical state measurement: Sampling the joint density matrix*. Phys. Rev. A, **54** (1996) 2397–2401. doi:10.1103/PhysRevA.54.2397.
- [51] LEONHARDT U., PAUL H. and D’ARIANO G.M. *Tomographic reconstruction of the density matrix via pattern functions*. Phys. Rev. A, **52** (1995) 4899–4907. doi:10.1103/PhysRevA.52.4899.
- [52] D’ARIANO G.M., LEONHARDT U. and PAUL H. *Homodyne detection of the density matrix of the radiation field*. Phys. Rev. A, **52** (1995) R1801–R1804. doi:10.1103/PhysRevA.52.R1801.
- [53] LEONHARDT U. and RAYMER M.G. *Observation of moving wave packets reveals their quantum state*. Phys. Rev. Lett., **76** (1996) 1985–1989. doi:10.1103/PhysRevLett.76.1985.
- [54] KÜHN H., WELSCH D.G. and VOGEL W. *Reconstruction of the quantum state of multimode light*. Phys. Rev. A, **51** (1995) 4240–4249. doi:10.1103/PhysRevA.51.4240.
- [55] LEONHARDT U. and MUNROE M. *Number of phases required to determine a quantum state in optical homodyne tomography*. Phys. Rev. A, **54** (1996) 3682–3684. doi:10.1103/PhysRevA.54.3682.
- [56] POUND R.V. *Electronic frequency stabilization of microwave oscillators*. Review of Scientific Instruments, **17** (1946) 490–505. doi:10.1063/1.1770414.
- [57] DREVER R.W.P., HALL J.L., KOWALSKI F.V., HOUGH J., FORD G.M., MUNLEY A.J. and WARD H. *Laser phase and frequency stabilization using an optical resonator*. Appl. Phys. B, **31** (1983) 97–105. doi:10.1007/BF00702605.
- [58] BLACK E.D. *An introduction to pound–drever–hall laser frequency stabilization*. American Journal of Physics, **69** (2001) 79–87. doi:10.1119/1.1286663.
- [59] WILLKE B., UEHARA N., GUSTAFSON E.K., BYER R.L., KING P.J., SEEL S.U. and R. L. SAVAGE J. *Spatial and temporal filtering of a 10-w nd:yag laser with a fabry–perot ring-cavity premode cleaner*. Opt. Lett., **23** (1998) 1704–1706.
- [60] LASTZKA N. and SCHNABEL R. *The gouy phase shift in nonlinear interactions of waves*. Opt. Express, **15** (2007) 7211–7217.
- [61] GARDINER C.W. and COLLETT M.J. *Input and output in damped quantum systems: Quantum stochastic differential equations and the master equation*. Phys. Rev. A, **31** (1985) 3761–3774. doi:10.1103/PhysRevA.31.3761.
- [62] BUCHLER B.C., LAM P.K., BACHOR H.A., ANDERSEN U.L. and RALPH T.C. *Squeezing more from a quantum nondemolition measurement*. Phys. Rev. A, **65** (2001) 011803. doi:10.1103/PhysRevA.65.011803.

- [63] BOWEN W.P., SCHNABEL R., BACHOR H.A. and LAM P.K. *Polarization squeezing of continuous variable stokes parameters*. Phys. Rev. Lett., **88** (2002) 093601. doi: 10.1103/PhysRevLett.88.093601.
- [64] SCHNEIDER K., LANG M., MLYNEK J. and SCHILLER S. *Generation of strongly squeezed continuous-wave light at 1064 nm*. Opt. Express, **2** (1998) 59–64.
- [65] VOLK T., RUBININA N. and WÖHLECKE M. *Optical-damage-resistant impurities in lithium niobate*. J. Opt. Soc. Am. B, **11** (1994) 1681–1687.
- [66] BRYAN D.A., GERSON R. and TOMASCHKE H.E. *Increased optical damage resistance in lithium niobate*. Applied Physics Letters, **44** (1984) 847–849. doi: 10.1063/1.94946.
- [67] FURUKAWA Y., KITAMURA K., ALEXANDROVSKI A., ROUTE R.K., FEJER M.M. and FOULON G. *Green-induced infrared absorption in mgo doped linbo₃*. Applied Physics Letters, **78** (2001) 1970–1972. doi:10.1063/1.1359137.
- [68] SCHNABEL R., VAHLBRUCH H., FRANZEN A., CHELKOWSKI S., GROSSE N., BACHOR H.A., BOWEN W., LAM P. and DANZMANN K. *Squeezed light at sideband frequencies below 100 khz from a single opa*. Optics Communications, **240** (2004) 185 – 190. ISSN 0030-4018. doi:10.1016/j.optcom.2004.06.030.
- [69] LUDWIG R. and BRETCHKO P. *RF Circuit Design: Theory and Applications*. Pearson US Imports & PHIPES (1999). ISBN 0130953237.
- [70] MAAS S.A. *Microwave Mixers*. Artech House (1986). ISBN 0890061718.
- [71] SHANNON C. *Communication in the presence of noise*. Proceedings of the IEEE, **72** (1984) 1192–1201. ISSN 0018-9219.
- [72] UNSER M. *Sampling – 50 Years after Shannon*. Proceedings of the IEEE, **88** (2000) 569–587.
- [73] ABRAMOVICI A. and CHAPSKY J. *Feedback Control Systems – A Fast-Track Guide for Scientists and Engineers*. Springer US (2000). ISBN 978-0-7923-7935-5.
- [74] PAARMANN L.D. *Design and analysis of analog filters: a signal processing perspective*. Springer (2001). ISBN 0792373731.
- [75] BIANCHI G. and SORRENTINO R. *Electronic filter simulation & design*. McGraw-Hill Professional (2007). ISBN 0071494677.
- [76] HEINZEL G. *Advanced optical techniques for laser-interferometric gravitational-wave detectors*. Ph.D. thesis, Universität Hannover (1999).
- [77] SUMNER P. DAVIS MARK C. ABRAMS J.W.B. *Fourier transform spectrometry*. Academic Press (2001). ISBN 0120425106.

- [78] VOGEL W. *Nonclassical states: An observable criterion*. Phys. Rev. Lett., **84** (2000) 1849–1852. doi:10.1103/PhysRevLett.84.1849.
- [79] TITULAER U.M. and GLAUBER R.J. *Correlation functions for coherent fields*. Phys. Rev., **140** (1965) B676–B682. doi:10.1103/PhysRev.140.B676.
- [80] KIESEL T., VOGEL W., HAGE B., DIGUGLIELMO J., SAMBLOWSKI A. and SCHNABEL R. *Experimental test of nonclassicality criteria for phase-diffused squeezed states*. Phys. Rev. A, **79** 022122. doi:10.1103/PhysRevA.79.022122.
- [81] HONG C.K. and MANDEL L. *Higher-order squeezing of a quantum field*. Phys. Rev. Lett., **54** (1985) 323–325. doi:10.1103/PhysRevLett.54.323.
- [82] AGARWAL G. *Nonclassical characteristics of the marginals for the radiation field*. Optics Communications, **95** (1993) 109 – 112. ISSN 0030-4018. doi:10.1016/0030-4018(93)90059-E.
- [83] RICHTER T. and VOGEL W. *Nonclassicality of quantum states: A hierarchy of observable conditions*. Phys. Rev. Lett., **89** (2002) 283601. doi:10.1103/PhysRevLett.89.283601.
- [84] BROWNE D.E., EISERT J., SCHEEL S. and PLENIO M.B. *Driving non-Gaussian to Gaussian states with linear optics*. Phys. Rev. A, **67** (2003) 062320. doi:10.1103/PhysRevA.67.062320.
- [85] EISERT J., BROWNE D.E., SCHEEL S. and PLENIO M.B. *Distillation of continuous-variable entanglement with optical means*. Annals of Physics, **311** (2004) 431 – 458. ISSN 0003-4916. doi:10.1016/j.aop.2003.12.008.
- [86] HAGE B., SAMBLOWSKI A., DIGUGLIELMO J., FRANZEN A., FIURASEK J. and SCHNABEL R. *Preparation of distilled and purified continuous-variable entangled states*. Nat. Phys., **4** (2008) 915–918. ISSN 1745-2473. doi:10.1038/nphys1110.
- [87] DONG R., LASSEN M., HEERSINK J., MARQUARDT C., FILIP R., LEUCHS G. and ANDERSEN U.L. *Experimental entanglement distillation of mesoscopic quantum states*. Nat. Phys., **4** (2008) 919–923. ISSN 1745-2473. doi:10.1038/nphys1112.
- [88] BENNETT C.H., BRASSARD G., CRÉPEAU C., JOZSA R., PERES A. and WOOTTERS W.K. *Teleporting an unknown quantum state via dual classical and Einstein-Podolsky-Rosen channels*. Phys. Rev. Lett., **70** (1993) 1895–1899. doi:10.1103/PhysRevLett.70.1895.
- [89] BENNETT C. and BRASSARD G. *Quantum cryptography: Public key distribution and coin tossing*. In IEEE, ed., *Proceedings of IEEE International Conference on Computers, Systems, and Signal Processing*, (pp. 175–179) (1984).
- [90] VAIDMAN L. *Teleportation of quantum states*. Phys. Rev. A, **49** (1994) 1473–1476. doi:10.1103/PhysRevA.49.1473.

- [91] RALPH T.C. *Continuous variable quantum cryptography*. Phys. Rev. A, **61** (1999) 010303. doi:10.1103/PhysRevA.61.010303.
- [92] REID M.D. *Quantum cryptography with a predetermined key, using continuous-variable Einstein-Podolsky-Rosen correlations*. Phys. Rev. A, **62** (2000) 062308. doi:10.1103/PhysRevA.62.062308.
- [93] HILLERY M. *Quantum cryptography with squeezed states*. Phys. Rev. A, **61** (2000) 022309. doi:10.1103/PhysRevA.61.022309.
- [94] VAHLBRUCH H., MEHMET M., CHELKOWSKI S., HAGE B., FRANZEN A., LASTZKA N., LER S.G., DANZMANN K. and SCHNABEL R. *Observation of squeezed light with 10-db quantum-noise reduction*. Phys. Rev. Lett., **100** 033602. doi:10.1103/PhysRevLett.100.033602.
- [95] FIURÁŠEK J. *Gaussian transformations and distillation of entangled Gaussian states*. Phys. Rev. Lett., **89** (2002) 137904. doi:10.1103/PhysRevLett.89.137904.
- [96] PAN J.W., GASPARONI S., URSIN R., WEIHS G. and ZEILINGER A. *Experimental entanglement purification of arbitrary unknown states*. Nature, **423** (2003) 417–422. ISSN 0028-0836. doi:10.1038/nature01623.
- [97] ZHAO Z., YANG T., CHEN Y.A., ZHANG A.N. and PAN J.W. *Experimental realization of entanglement concentration and a quantum repeater*. Phys. Rev. Lett., **90** (2003) 207901. doi:10.1103/PhysRevLett.90.207901.
- [98] OURJOUNTSEV A., TUALLE-BROURI R., LAURAT J. and GRANGIER P. *Generating Optical Schrodinger Kittens for Quantum Information Processing*. Science, **312** (2006) 83–86. doi:10.1126/science.1122858.
- [99] NEERGAARD-NIELSEN J.S., NIELSEN B.M., HETTICH C., LMER K.M. and POLZIK E.S. *Generation of a superposition of odd photon number states for quantum information networks*. Phys. Rev. Lett., **97** 083604. doi:10.1103/PhysRevLett.97.083604.
- [100] WAKUI K., TAKAHASHI H., FURUSAWA A. and SASAKI M. *Photon subtracted squeezed states generated with periodically poled ktiopo4*. Opt. Express, **15** (2007) 3568–3574.
- [101] HAGE B. *Quantentomographische Charakterisierung gequetscher Zustände*. Master's thesis, Leibniz Universität Hannover, Germany (April 2004).
- [102] VAHLBRUCH H., CHELKOWSKI S., HAGE B., FRANZEN A., DANZMANN K. and SCHNABEL R. *Coherent control of vacuum squeezing in the gravitational-wave detection band*. Ohys. Rev. Lett., **97** 011101. doi:10.1103/PhysRevLett.97.011101.
- [103] ABRAMOVICI A. and CHAPSKY J. *Feedback Control Systems*. Kluwer Academic Publ. (2000). ISBN 0792379357.

[104] SIEGMANN A.E. *Lasers*. University Science Books (1986). ISBN 0935702113.

[105] YARIV A. *Quantum Electronics*. Wiley (1989). ISBN 0471609978.